Energie & Umwelt
Energy & Environment

340

Atomic oxygen derived from SCIAMACHY

Yajun Zhu

Member of the Helmholtz Association

Energie & Umwelt /
Energy & Environment
Band / Volume 340
ISBN 978-3-95806-178-1

JÜLICH
FORSCHUNGSZENTRUM

Atomic oxygen derived from SCIAMACHY O(¹S) and OH airglow measurements in the Mesopause region

Yajun Zhu

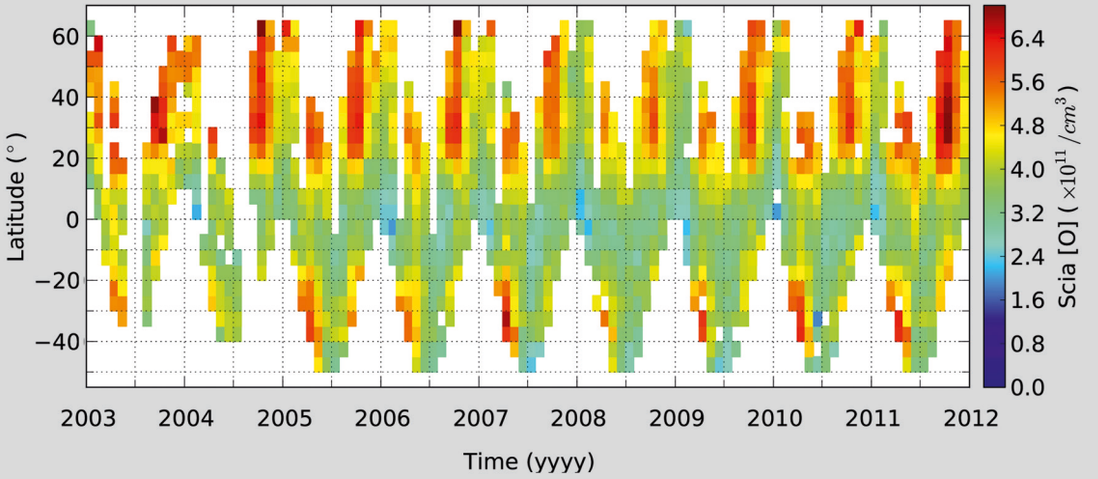

Energie & Umwelt /
Energy & Environment
Band / Volume 340
ISBN 978-3-95806-178-1

JÜLICH
FORSCHUNGSZENTRUM

Atomic oxygen derived from SCIAMACHY O(^{1}S) and OH airglow measurements in the Mesopause region

Dissertation

zur Erlangung des Grades
Doktor der Naturwissenschaften (Dr. rer. nat.)

vorgelegt der

Bergischen Universität Wuppertal
Fakultät für Mathematik und Naturwissenschaften

von

Yajun Zhu

Wuppertal, 2016

Die Dissertation kann wie folgt zitiert werden:

urn:nbn:de:hbz:468-20161019-092721-7
[http://nbn-resolving.de/urn/resolver.pl?urn=urn%3Anbn%3Ade%3Ahbz%3A468-20161019-092721-7]

Forschungszentrum Jülich GmbH
Institute of Energy and Climate Research
Stratosphere (IEK-7)

Atomic oxygen derived from SCIAMACHY O(^{1}S) and OH airglow measurements in the Mesopause region

Yajun Zhu

Schriften des Forschungszentrums Jülich
Reihe Energie & Umwelt / Energy & Environment Band / Volume 340

ISSN 1866-1793 ISBN 978-3-95806-178-1

Bibliographic information published by the Deutsche Nationalbibliothek.
The Deutsche Nationalbibliothek lists this publication in the Deutsche
Nationalbibliografie; detailed bibliographic data are available in the
Internet at http://dnb.d-nb.de.

Publisher and Distributor:	Forschungszentrum Jülich GmbH Zentralbibliothek 52425 Jülich Tel: +49 2461 61-5368 Fax: +49 2461 61-6103 Email: zb-publikation@fz-juelich.de www.fz-juelich.de/zb
Cover Design:	Grafische Medien, Forschungszentrum Jülich GmbH
Printer:	Grafische Medien, Forschungszentrum Jülich GmbH
Copyright:	Forschungszentrum Jülich 2016

Schriften des Forschungszentrums Jülich
Reihe Energie & Umwelt / Energy & Environment, Band / Volume 340

D 468 (Diss., Wuppertal, Univ., 2016)

ISSN 1866-1793
ISBN 978-3-95806-178-1

The complete volume is freely available on the Internet on the Jülicher Open Access Server (JuSER)
at www.fz-juelich.de/zb/openaccess.

This is an Open Access publication distributed under the terms of the Creative Commons Attribution License 4.0,
which permits unrestricted use, distribution, and reproduction in any medium, provided the original work is properly cited.

ABSTRACT

Atomic oxygen plays a crucial role in the photochemistry and energy balance of the mesopause region. In particular, it is the most abundant reactive species and an important quantity in the derivation of temperature, ozone and other constituents in this part of the atmosphere. This work deals with the derivation of the atomic oxygen abundance from SCIAMACHY (Scanning Imaging Absorption spectroMeter for Atmospheric CHartographY) $O(^1S)$ green line and OH(9-6) band nightglow measurements from 2003 to 2011.

There are two different photochemical models available, which describe $O(^1S)$ green line volume emission rates, namely the ETON and Khomich models. Differences between the two models and their implication on the derivation of atomic oxygen abundance are discussed. Two atomic oxygen datasets are derived from SCIAMACHY $O(^1S)$ green line measurements at 90–105 km. Analyses are performed on abundance uncertainties owing to rate constants and background atmosphere (i.e., temperature and total density), as well as abundance differences (up to around 20%) arising from the different model schemes. One photochemical model is used to simulate SCIAMACHY OH(9-6) band measurements and the resulting atomic oxygen abundance is derived at 80–96 km. Induced abundance uncertainties, as a result of uncertainties in rate constants and background atmosphere, are 20% at 80 km, which rise intensively up to 90% at 96 km.

Atomic oxygen datasets derived from SCIAMACHY measurements show a consistent picture with each other. These derived datasets agree within 20% to the atomic oxygen data derived from WINDII (Wind Imaging Interferometer) $O(^1S)$ and OH nightglow measurements, whereas atomic oxygen data derived from simultaneously measured SABER (Sounding of the Atmosphere using Broadband Emission Radiometry) OH nightglow emissions are around 30–50% larger than the SCIAMACHY and WINDII data.

The effect of the 11-year solar cycle is clearly evident in the atomic oxygen data. An investigation is conducted on the solar maximum/minimum (max/min) differences imprinted in SCIAMACHY and SABER atomic oxygen abundances. The differences vary in a range of 8–18% and depend on latitude. One striking feature is that the solar cycle variation increases with altitude at 90–105 km. The solar cycle variation is discussed using HAMMONIA (Hamburg Model of the Neutral and Ionized Atmosphere) model data. The model suggests that the 11-year solar cycle observed in the atomic oxygen abundance is mostly caused by total density variations (about 6–11% at 90–105 km) compared to volume mixing ratio (vmr) variations (3%). Thus, the atomic oxygen solar max/min variation is primarily driven by the total density compression/expansion variations during the solar cycle, rather than different atomic oxygen volume mixing ratios relevant to photolysis rates.

Contents

Chapter 1

Introduction

1.1 Atmospheric structure

The Earth's atmosphere extends from the surface up to 1000 km and consists of many species, such as O_2, N_2, O (mainly above 80 km), Ar, and CO_2. Mixing ratios of inert species (e.g., O_2 and N_2) tend to be independent of altitude below around 100 km owing to turbulent motion mixing, but decrease exponentially with increase of height above 100 km with a scale height which is inversely proportional to species weight (*Wallace and Hobbs*, 2006).

Based on the temperature profile, the Earth's atmosphere is normally divided into four different layers, namely troposphere, stratosphere, mesosphere, and thermosphere. Boundaries between these layers are labeled with suffix "pause", namely tropopause, stratopause and mesopause, where the vertical temperature gradient is roughly equal to

zero. Figure 1.1 displays a typical spring time atmospheric temperature profile at 40°N. Temperature is calculated from the MSIS (Mass Spectrometer and Incoherent Scatter) empirical model (*Picone et al.*, 2002). The troposphere just lies above the Earth's surface up to a height around

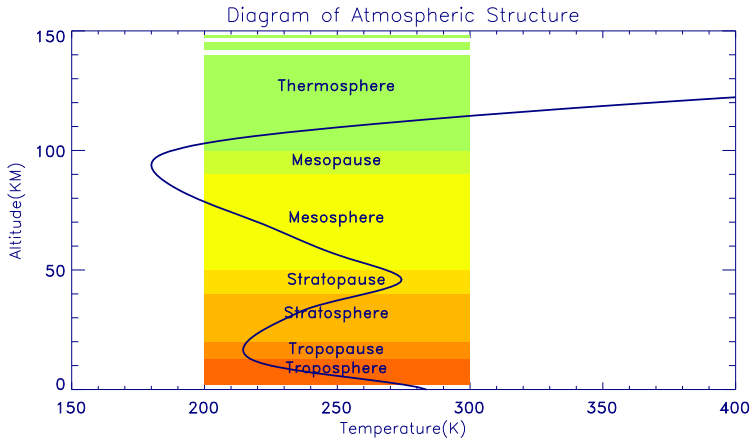

Figure 1.1: A typical spring atmospheric temperature profile at 40°N. The atmospheric layers are roughly labelled by different colors. The temperature is simulated by MSIS empirical model.

15 km. The main energy source in this region is the sun-warmed surface (i.e., land and ocean) of Earth and the energy is transferred to the atmosphere via infrared radiation, sensible, or latent heat. Therefore, atmospheric temperature decreases with the increase of height due to the convection and radiative cooling in the atmosphere and the lapse rate is about -6.5 K/km. The vertical temperature gradient changes from negative to positive at the tropopause. In the stratosphere, temperature in-

creases slowly from the tropopause region and reaches its maximum at around 50 km. The vertical temperature gradient is positive and there is no regular convection. The air is rather dry but rich in ozone. The main energy source in the region comes from the absorption of the ultraviolet radiation of the sun by ozone. Some energy is released as heat by chemical reactions with ozone. The dominant cooling process is CO_2 infrared radiation. The increase of temperature with altitude ceases at the stratopause. Above the stratopause lies the mesosphere. Infrared radiation, mainly emitted by carbon dioxide, again dominates the cooling of this region. The absorption of solar ultraviolet radiation by ozone and oxygen is the main source of heating. Temperature decreases again with the increase of height and reaches its local minimum at around 95 km, where is the mesopause region. In the thermosphere (above 100 km), the mean free path of molecules exceeds 1 m and molecular diffusion is more predominant than turbulence and eddy mixing in this region. Heavier molecules (such as O_2, N_2, CO_2) decreases much more rapidly and their mixing ratios vary fast with height (*Wallace and Hobbs*, 2006). The main energy source comes from the absorption of extreme ultraviolet radiation of the sun by molecules.

In this thesis, the mesopause is investigated based on global satellite observations in the recent years. Dynamics, energetics and photochemistry are strongly coupled and balanced in the mesopause, which is not found in the other part of atmosphere (*Smith*, 2012a). Therefore, the in-

vestigation intends to improve understanding of interactions of dynamics, chemistry and radiations in the mesopause, especially the solar activity effect which is the main energy input in this region.

1.2 The Upper Mesosphere and Lower Thermosphere (UMLT) region

The UMLT region is known as a transition region between the mesosphere and thermosphere (the mesopause region). The vertical temperature gradient changes from negative sign to positive sign in this region. The UMLT is the coldest region in the atmospheric system, especially in the summer season. It is known that the summer mesopause is much colder than the winter mesopause, which results from strong adiabatic cooling associated with upwelling air in the summer season and adiabatic heating due to downwelling air in the winter season (*Smith et al.*, 2011a). The transport is part of the global mean circulation in the UMLT region, which is mainly driven by momentum deposited by gravity waves that are excited at lower altitudes and filtered by stratospheric winds (*Smith et al.*, 2011a).

The photo-dissociation of O_2 and O_3 by solar ultraviolet (UV) radiation is the major energy input of the UMLT region. The solar UV absorption mainly occurs at 121.5–204.5 nm (at the Lyman-α line, in the

Schumann-Runge continuum, and in the Schumann-Runge bands) for O_2 and in the Hartley band for O_3 (*Mlynczak et al.*, 2013a). It is worth noting that the dissociation of O_2 mainly occurs in the thermosphere but the generated atomic oxygen, with chemical energy from the solar radiation, can be transported downward to the UMLT region owing to its long lifetime (see next section).

The UV radiation is partly converted to ambient heat to increase the kinetic temperature. The heating rate due to O_2 dissociation increases from about 1 K/day at 80 km to around 6 K/day at 100 km (*Mlynczak et al.*, 2013a). The O_3 heating rate peaks at 90 km (3 K/day) and decreases out of the peak altitude. Another two minor heating sources due to the absorption of solar radiation are carbon dioxide in the near infrared region (*Fomichev et al.*, 2004) and the water vapour at the Lyman-α line, in the Schumann-Runge continuum, and in the Schumann-Runge bands (*Smith et al.*, 2011a).

The input energy partially (around 70% of the absorbed energy (*Strobel*, 1978)) converts to chemical energy to excite atoms or molecules. Chemical reactions play a significant role in the transfer of energy and seven exothermic chemical reactions are relevant to the chemical heating in the UMLT region (Table 1.1) (*Riese et al.*, 1994). Their chemical heating rates are displayed in Figure 1.2 except for the reactions R5 and R7 whose heating rates are less than 1 K/day (*Mlynczak et al.*, 2013a). The two dominant chemical heating sources are the three-body recombination

Table 1.1: Seven exothermic chemical reactions which are of importance in the energy budget in the UMLT region.

Number	Reactions
R1	$O + O + M \rightarrow O_2^* + M + 5.12eV$
R2	$O + O_2 + M \rightarrow O_3 + M + 1.05eV$
R3	$O + O_3 \rightarrow O_2 + O_2 + 4.06eV$
R4	$O + OH \rightarrow H + O_2 + 0.72eV$
R5	$O + HO_2 \rightarrow OH + O_2 + 2.29eV$
R6	$H + O_3 \rightarrow OH^*(v \leq 9) + O_2 + 3.34eV$
R7	$H + O_2 + M \rightarrow HO_2 + M + 2.00eV$

reaction of O (R1 in Table 1.1), which could excite oxygen to several metastable states (O_2^*), and the reaction of H and O_3 (R6), which mainly produces vibrationally excited OH^* in the UMLT region. Adding the heating rate due to the recombination reaction of O and O_2 could account for 85–98% chemical heating at 80–100 km.

The energy is balanced on a long-term scale in the UMLT region, that is, the solar and exothermic chemical heating are equal to total cooling. CO_2 plays a crucial role in removing thermal energy from this region. Radiative cooling occurs in such a way that CO_2 is excited to various vibrational states via collisions with other species (e.g., O) and, then, de-excited by spontaneous emissions (e.g., 4.3 μm and 15 μm) (*Smith et al.*, 2011a). CO_2 radiative cooling rate is around 2 K/day at 80 km, which rises up to about 16 K/day above 90 km (*Mlynczak et al.*, 2013a). Another cooling source is the infrared emission by water vapour but its

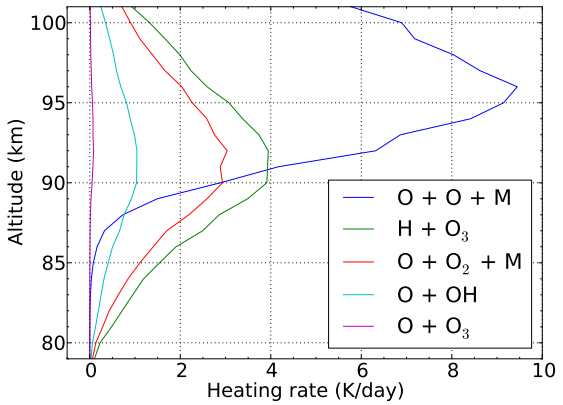

Figure 1.2: Heating rates of different exothermic chemical reactions. The background atmosphere is derived from SABER measurements at 22.5°N November 2005 and the calculation is based on the algorithms introduced by *Mlynczak et al.* (2013a).

contribution is minor (*Fomichev et al.*, 2004).

The direct solar heating is smaller in comparison to chemical heating in the UMLT region generally. In particular, the *O*-related exothermic reactions account for 45–94% of the chemical heating at 80–100 km. Collisions of CO_2 with atomic oxygen are also important in exciting the vibrational states of CO_2. Therefore, atomic oxygen is an important quantity for understanding the photochemistry (Table 1.1) and energy budget (Figure 1.2) in the UMLT region. It is the intention of this work to derive atomic oxygen abundance from SCIAMACHY measurements in this region.

1.3 Atomic oxygen in the UMLT region

Atomic oxygen is a key parameter for the photochemistry and energy balance in the UMLT region (e.g., *Brasseur and Offermann*, 1986; *Mlynczak and Solomon*, 1993; *Riese et al.*, 1994), as stated in the last section. It is mainly formed through the photolysis of molecular oxygen by solar ultraviolet radiation at the Lyman-α line, in the Schumann-Runge continuum, and in the Schumann-Runge bands in the thermosphere. Its lifetime varies with altitude from 24 hours at around 85 km (*Russell*, 2003) to months at 100 km (*Smith et al.*, 2010). As a result, transport plays an important role in atomic oxygen spatial distribution in the UMLT region, such as molecular diffusion, eddy diffusion and advection (*Smith and Marsh*, 2005). Reacting with other molecules is the main loss mechanism for the atomic oxygen in the UMLT region (Table 1.1). Figure 1.3 shows three atomic oxygen profiles at 30°S, 0 and 30°N on 15th, Sep., 2007. Atomic oxygen peak concentration at 30°S is around 20% larger than at 30°N. Atomic oxygen peak altitude at the equator (101 km) is around 3 km higher than at 30°S and 30°N (98 km). Atomic oxygen maximum at the mesopause is caused by several processes and an explanation was given by *Smith and Marsh* (2005) based on a dynamical-chemical numerical model simulation. Atomic oxygen volume mixing ratio increases with height due to its lower weight than for background molecules. There is a net photochemical production of atomic oxygen above 0.0006 hPa (around 96 km) and

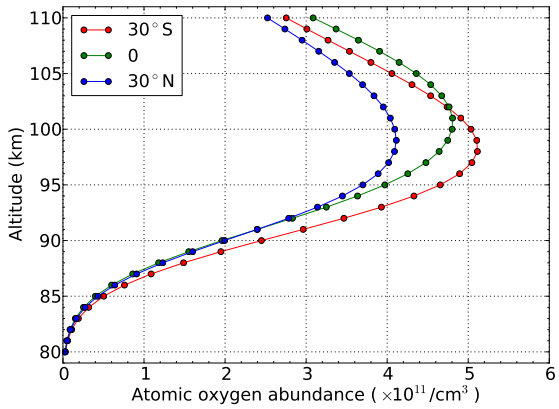

Figure 1.3: Atomic oxygen abundances at 30°S, 0 and 30°N for Sept., 2007. Atomic oxygen was calculated by the MSIS model for 22 local solar time.

a net loss below this altitude. The molecular diffusion tends to increase the atomic oxygen abundance below 105 km. The eddy diffusion acts to increase the atomic oxygen abundance below the mesopause, resulting in a rapid decline of the atomic oxygen abundance due to its shorter chemical lifetime. The advective transport relevant to tides leads to a minor net downwelling transport in the UMLT region. Therefore, the atomic oxygen abundance peaks at around 96 km and falls off slowly above this peak due to the molecular diffusion, but declines sharply below this peak owing to the eddy diffusion (*Russell et al.*, 2005).

The atomic oxygen concentration also shows prominent seasonal and long-term variations, such as Semi-Annual (SAO) and Annual (AO) oscillations, as well as 11-year solar cycle variation. The SAO is caused

by the semi-annual variation in diurnal tidal amplitude and the AO is relevant to the mean meridional circulation (*Shepherd et al.*, 2006a; *Smith*, 2012a). The solar cycle variation imprinted in atomic oxygen results from the solar ultraviolet radiation and energetic particle precipitation. Temporal variations of the MSIS atomic oxygen concentration with altitude at 30°N are displayed in Figure 1.4. A prominent AO is found. The annual oscillation peaks in winter seasons at 30°N. A strong 11-year solar cycle variation of the MSIS atomic oxygen is also found with a maximum around 2002 and a minimum around 2009, because the MSIS model is sensitive to the solar flux (*Picone et al.*, 2002). A factor of 4.12×10^6 molecules/100SFU (SFU: F10.7 cm solar flux unit of $10^{-22}\mathrm{Wm}^{-2}\mathrm{Hz}^{-1}$ (*Tapping*, 2013)) is found between MSIS atomic oxygen abundance and

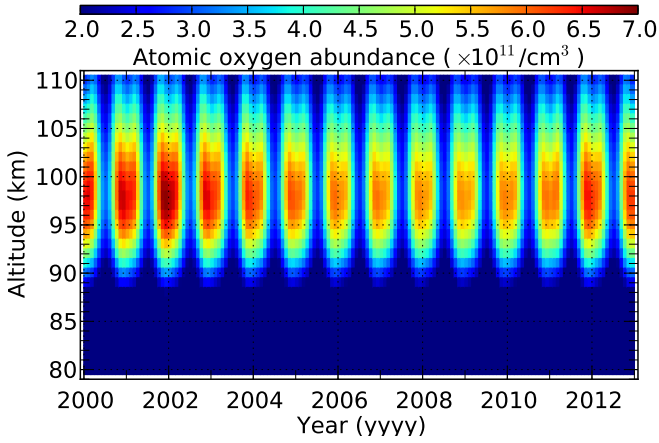

Figure 1.4: Time-altitude cross section of the MSIS atomic oxygen concentration at 30°N and 10 p.m..

the F10.7 cm solar flux and the atomic oxygen solar max/min difference is around 18% at 90–95 km.

The measurement of atomic oxygen in the mesopause region is rather difficult. Sounding rockets are the only technique until now to perform in-situ measurements in this region (*Hedin et al.*, 2009). In-situ measurements of ground state atomic oxygen were conducted for the first time by the mass spectrometry technique (*Offermann et al.*, 1981) and later by the resonance fluorescence technique using the 130 nm $O(^3S\text{-}^3P)$ transition (for an overview see, e.g., *Gumbel*, 1998). These in situ measurements show a consistent picture in the general shape of atomic oxygen profiles, but differ a lot in the absolute values (*Hedin et al.*, 2009).

Remote sensing is the most commonly-used method to perform atomic oxygen observations of this part of the atmosphere by ground-based, rocket- and space- borne instruments (e.g. *Haley et al.*, 2001; *Russell et al.*, 2005; *Smith et al.*, 2010; *Sheese et al.*, 2011; *Mlynczak et al.*, 2013b). Various airglow emissions and thermal emissions (e.g., O_3 daytime 9.6 μm bands) are often used as proxies for atomic oxygen. The airglow emissions are arising from excited atoms or molecules, such as O, O_2, and OH, by undergoing spontaneous quantum transitions, either electronically, vibrationally or rotationally. Atomic oxygen abundance can be derived from these airglow and thermal emissions in conjunction with corresponding photochemical models based on the assumption of photochemical balance.

Ground-based observations of O, O_2 and OH nightglow emissions have been used to determine parameterized atomic oxygen profiles based on the differences in the molecularities of these emissions (*Melo et al.*, 2001; *Haley et al.*, 2001). These measurements provide data with a good temporal coverage, but they are restricted to a few locations only.

Several rocket sounding campaigns have been conducted to observe the $O(^1S)$ green line, the O_2 atmospheric band and the OH nightglow emissions to derive atomic oxygen (e.g., *Dandekar and Turtle*, 1971; *Good*, 1976; *Witt et al.*, 1984; *Melo et al.*, 1996; *Iwagami et al.*, 2003; *Hecht et al.*, 2004). Some of these airglow measurements were used to investigate mechanisms of the airglow emissions and to develop photochemical models in combination with in situ atomic oxygen measurements. They were mainly OXYGEN/S35 in 1981 (*Witt et al.*, 1984), ETON (Energy Transfer in the Oxygen Nightglow) in 1982 (*Greer et al.*, 1986), OASIS (Oxygen Atom Studies In Space) in 1983 (*Murtagh et al.*, 1990) and NLTE (Non Local Thermodynamic Equilibrium) in 1998 (*Hedin et al.*, 2009). During the ETON campaign, the photochemical schemes of $O(^1S)$, O_2^* and OH nightglow emissions were developed by using different measurement techniques in the UMLT region (e.g., *Greer et al.*, 1986; *McDade et al.*, 1986; *McDade and Llewellyn*, 1986; *McDade and Llewellyn*, 1987; *Murtagh et al.*, 1990). Sounding rocket measurements achieve a very high vertical resolution, but are infrequently used due to their high expense.

Many satellite-borne airglow measurements of the $O(^1S)$, O_2 A-band, and OH^* emissions, as well as measurements of O_3 thermal emissions, have been performed to determine the atomic oxygen abundance in recent years. The $O(^1S)$ green line emission was measured by the WINDII instrument aboard the UARS (Upper Atmosphere Research Satellite) (*Russell et al.*, 2005), as well as the ISUAL (Imager of Sprites and Upper Atmospheric Lightning) instrument aboard the FORMOSAT-2 satellite (*Gao et al.*, 2012). O_2 A-band emission measurements were conducted by the HRDI (High Resolution Doppler Imager) instrument aboard the Upper Atmospheric Research Satellite (UARS) (*Hays et al.*, 1993) and the OSIRIS (Optical Spectrograph and Infrared Imager System) instrument on the Odin satellite (*Sheese et al.*, 2011). O_3 daytime thermal emissions were observed by the SABER instrument on the TIMED (Thermosphere Ionosphere Mesosphere Energetics Dynamics) satellite (*Smith et al.*, 2010). OH^* emissions were measured by the WINDII instrument, the OSIRIS instrument, and the SABER instrument on the TIMED satellite (*Mlynczak et al.*, 2013b). These measurements provide a global coverage of the data but are limited in local time sampling.

1.4 The SCIAMACHY instrument aboard the Envisat

The satellite measurements analyzed in this work stem from SCIAMACHY on Envisat (*Louet*, 2001). Envisat was developed by the European Space Agency (ESA) and launched on March 1st, 2002. The mission ended on April 8th, 2012. The satellite operated in a sun-synchronous orbit with an inclination of 98.55° and a mean altitude of 799.8 km. The mean local solar time during morning descending node crossing was around 10 a.m.. Aboard Envisat were nine instruments monitoring the Earth's land, ice, water, atmosphere based on a variety of measurement principles and one payload for guidance and control (*Louet*, 2001). The nine instruments are the Advanced Synthetic Aperture Radar (ASAR), the MEdium Resolution Imaging Spectrometer (MERIS), the Advanced Along Track Scanning Radiometer (AATSR), the Radar Altimeter 2 (RA-2), the MicroWave Radiometer (MWR), the Michelson Interferometer for Passive Atmospheric Sounding (MIPAS), the Global Ozone Monitoring by Occultation of Stars (GOMOS), the Scanning Imaging Absorption spectroMeter for Atmospheric CHartographY (SCIAMACHY), and the Laser Retro-Reflector (LRR). Figure 1.5 shows a sketch of Envisat with its nine instruments and other carriers.

MIPAS, GOMOS and SCIAMACHY are the payloads for the atmospheric research (*Gottwald et al.*, 2006). MIPAS is a mid-infrared Fourier

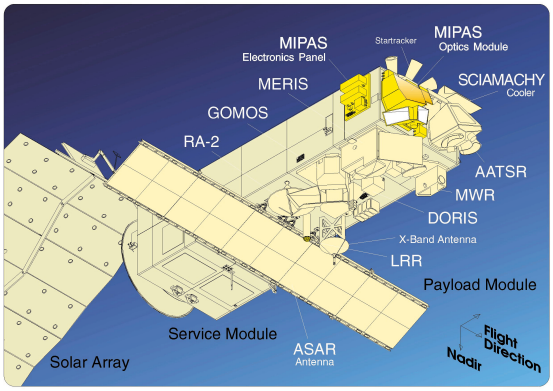

Figure 1.5: A sketch of Envisat. (photo:ESA)

transform spectrometer to detect limb emission spectra in the middle and upper atmosphere. GOMOS is a medium resolution spectrometer and observed the Earth limb in a stellar occultation mode. SCIAMACHY is a passive imaging spectrometer to record images from Earth surface, atmosphere and sun in different viewing modes. A detailed discussion of the SCIAMACHY instrument is given by *Gottwald et al.* (2006). A summary is introduced below.

Two observing geometries of SCIAMACHY are displayed in Figure 1.6. SCIAMACHY looks towards the sub-satellite point (nadir mode) and also looks along the satellite track into flight direction (limb mode). For the limb mode, the observation is performed in such a way that a swath of 960 km is recorded in horizontal direction within 1.5 s at a fixed tangent point. The line of sight moves upwards step by step at the end

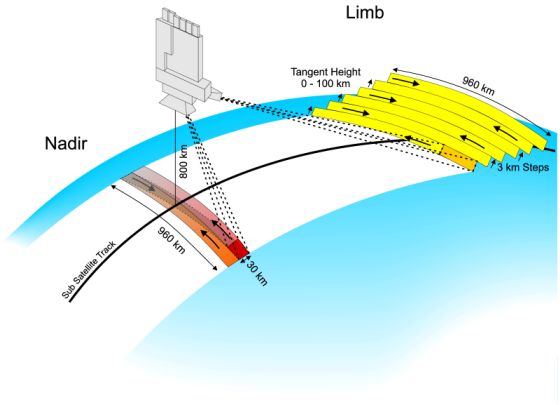

Figure 1.6: Viewing geometries of the SCIAMACHY. (*Noël et al.*, 2002)

of each scan, but the scan direction is reversed to the last observation (*Noël et al.*, 2002). Besides nadir and limb modes, SCIAMACHY also operates in occultation (sun and moon) and sub-solar viewing modes. The SCIAMACHY instrument has eight spectral channels which continuously cover three wavelength ranges, namely 214-1773 nm, 1934-2044 nm and 2259-2386 nm, as shown in Table 1.2. The spectral resolution varies from 0.22 nm to 1.48 nm depending on the channel.

Nighttime SCIAMACHY limb measurements are used in this work to derive the atomic oxygen abundance. The emissions analysed in this work are recorded in channel 3 ($O(^1S)$ green line spectra) and in channel 6 (OH spectra). The tangent altitudes for these measurements extend from 73 km to 148 km with a 3.3 km vertical resolution and the observed local solar time is around 10 p.m.. A detailed introduction to these two emissions

Table 1.2: SCIAMACHY eight spectral channels. (*Gottwald et al.*, 2006)

Channel	Spectral coverage (nm)	Resolution (nm)
1	214–334	0.24
2	300–412	0.26
3	383–628	0.44
4	595–812	0.48
5	773–1063	0.54
6	971–1773	1.48
7	1934–2044	0.22
8	2259–2386	0.26

will be given in Chapter 2 and Chapter 3, respectively.

Chapter 2

Nighttime O(^{1}S) green line emission measurements and modeling

The green line emission at 557.7 nm is produced by the spontaneous emission of $O(^1S\text{-}^1D)$, which can be observed during the whole day and visible in auroras. The green line emission peaks at around 96 km and an additional peak at around 170 km can be found in the thermosphere (daytime), which results from collisions of the abundant atomic oxygen with photoelectrons (*Dandekar and Turtle*, 1971; *Singh et al.*, 1996).

2.1 O(^{1}S) green line emission measurements

The green line emission was first investigated by *Rayleigh* (1924). The SAO, AO and some solar cycle dependence were derived from green line

measurements at three stations (Terling; Commonwealth Observatory, Mount Stromlo; Royal Observatory, Cape Town) (*Rayleigh and Jones*, 1935). Since then, the green line emission has been observed by many ground-based instruments (see, e.g., *Rayleigh*, 1924; *Rayleigh and Jones*, 1935; *Silverman*, 1970; *Fukuyama*, 1976, 1977; *Deutsch and Hernandez*, 2003; *Das*, 2011, and references therein), rocket-borne instruments (see, e.g., *Dandekar and Turtle*, 1971; *Offermann and Drescher*, 1973; *Greer et al.*, 1986, and references therein) and space-borne instruments (see, e.g., *Shepherd et al.*, 1999; *Russell*, 2001; *Gao et al.*, 2012; *Kaufmann et al.*, 2014; *Zhu et al.*, 2015).

Dandekar and Turtle (1971) derived atomic oxygen profiles from the rocket-borne green line measurements. They confirmed that the green line emission peaks at two altitudes: one is at approximately 100 km and another one is at above 150 km. *Offermann and Drescher* (1973) compared a series of atomic oxygen profiles derived from cryo-cooled mass spectrometer observations and photometer green line measurements based on the Chapman mechanism. The green line emission was also measured during the ETON campaign by launching seven rockets successively within 2.5 hours in March 23, 1982 at South Uist firing range (57.36°N, 7.38°W). Photometers and resonance lamps flown in the ETON campaign performed the airglow and atomic oxygen abundance measurements (*Greer et al.*, 1986). These measurements were used to investigate excitation and quenching mechanisms of $O(^1S)$ in combination with

molecular oxygen airglow measurements (*McDade et al.*, 1986). *Hecht et al.* (2004) used $O(^1S)$ green line emission measurements monitored by rocket-borne photometers in the Turbulent Oxygen Mixing Experiment (TOMEX) to derive the atomic oxygen concentrations, in combination with ground-based Na lidar and the thermosphere/ionosphere/mesopsphere/electrodynamics general circulation (TIME-GCM) model (*Roble and Ridley*, 1994).

The $O(^1S)$ green line emission has been measured by several spaceborne instruments and the atomic oxygen abundance was derived from these measurements (see Chapter 1). Recently, near ten-year green line measurements were conducted by the channel 3 of the SCIAMACHY instrument aboard the Envisat (*von Savigny and Lednyts'kyy*, 2013; *Lednyts'kyy et al.*, 2015). A typical monthly zonal mean limb green line spectrum measured by SCIAMACHY is displayed in Figure 2.1. Its peak emission rate is around 7.0×10^8 photons/s/cm^2/sr/nm. The SCIAMACHY green line measurements will be used to derive the atomic oxygen abundances based on the forward models stated below (see Chapter 5).

2.2 O(^{1}S) photochemistry

Chapman (1931) proposed a mechanism (the Chapman mechanism) to produce $O(^1S)$ in the mesosphere by considering the three-body recombi-

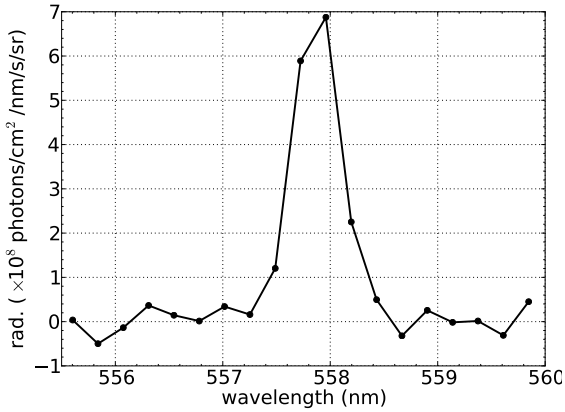

Figure 2.1: Monthly zonal mean limb green line spectrum at 92 km and 30°–35°N for September, 2008.

nation of atomic oxygen:

$$O + O + O \xrightarrow{k_{OOO}} O_2 + O(^1S) \tag{R2.1}$$

k_{OOO} ($\sim 4.8 \times 10^{-33}$ cm^6/s) is the atomic oxygen three-body recombination reaction rate constant. Then, *Barth and Hildebrandt* (1961) introduced a two-step mechanism to explain the production of $O(^1\mathrm{S})$ under the conditions of mesosphere, known as the "Barth Mechanism".

$$O + O + M \xrightarrow{k_{OOM}} O_2^* + M \tag{R2.2}$$

$$O_2^* + O(^3P) \xrightarrow{k'_{O_2^*O}} O(^1S) + O_2 \tag{R2.3}$$

M represents O_2 or N_2. k_{OOM} is the three-body recombination reaction rate constant. The numerical values of k_{OOM} and the following rate constants are given in Table tab-1 in Appendix A.1. $k'_{O_2^*O}$ is the reaction rate constant in the formation of $O(^1\mathrm{S})$ (Eq. R2.3).

Further laboratory measurements revealed that the measured rate constants favour the Barth mechanism, but not the Chapman mechanism (*Slanger and Black*, 1976). The nightglow measurement investigations also revealed that measured green line emission profiles are in good agreement with the ones yielded by measured atomic oxygen profiles if the Barth mechanism is used (*Slanger and Black*, 1977; *Witt et al.*, 1979). The reason is that the Chapman mechanism needs a large photochemical rate constant to produce a certain amount of green line volume emission rates.

O_2^*, mainly representing $O_2(^5\Pi_g)$, $O_2(c^1\Sigma_u^-)$, $O_2(A^3\Sigma_u^+)$, or $O_2(A'^3\Delta_u)$, is a highly electronically and vibrationally excited, metastable state of O_2 which can be de-excited by the emission of photons (Eq. R2.4), as described by the Einstein coefficient ($A_{O_2^*}$), and quenching by $O(^3\mathrm{P})$ (Eq. R2.3 and R2.5), O_2 (Eq. R2.6) and N_2 (Eq. R2.7) without undergoing long-range transport.

$$O_2^* \xrightarrow{A_{O_2^*}} O_2 + h\nu \qquad \text{(R2.4)}$$

$$O_2^* + O(^3P) \xrightarrow{k''_{O_2^*O}} O(^3P) + O_2 \quad \text{(R2.5)}$$

$$O_2^* + O_2 \xrightarrow{k_{O_2^*O_2}} O_2 + O_2 \quad \text{(R2.6)}$$

$$O_2^* + N_2 \xrightarrow{k_{O_2^*N_2}} N_2 + O_2 \quad \text{(R2.7)}$$

$A_{O_2^*}$ is the inverse radiative lifetime of O_2^*. $k''_{O_2^*O}$ is the quenching rate constant to de-excite O_2^* only (Eq. R2.5). The quantities $k_{O_2^*O}$ (= $k'_{O_2^*O}$ + $k''_{O_2^*O}$), $k_{O_2^*O_2}$ and $k_{O_2^*N_2}$ are the reaction rate constants for O_2^* quenching by O, O_2 and N_2, respectively. In particular, only some of the collisions between O_2^* and $O(^3\mathrm{P})$ produce $O(^1\mathrm{S})$, as described by reaction R2.3, while most O_2^* is merely de-excited by collisions with $O(^3\mathrm{P})$ without the production of $O(^1\mathrm{S})$ (Eq. R2.5). It is supposed that $O_2(c^1\Sigma_u^-)$ is the most favoured precursor of $O(^1\mathrm{S})$ and $O_2(A^3\Sigma_u^+)$ and $O_2(A'^3\Delta_u)$ are not responsible for the excitation of $O(^1\mathrm{S})$ (*Slanger and Black*, 1976; *Bates*, 1988c,a; *López-González et al.*, 1992; *Slanger et al.*, 2003). $O_2(^5\Pi_g)$ is thought to be another significant precursor of $O(^1\mathrm{S})$, which takes up around 50% quantum yields in the reaction R2.2 (*Wraight*, 1982; *Smith*, 1984; *Krasnopolsky*, 1986; *Bates*, 1988b), but the hypothesis is still undetermined (*Bates*, 1988a).

$O(^1\mathrm{S})$ can be de-excited into different radiative channels, namely the green line emission at 557.7 nm, emissions at 295.83 nm and 297.73 nm

arising from $O(^1S\text{-}^3P)$ spontaneous transitions, as shown in Figure 2.2. Figure 2.2 displays the quantum transition of atomic oxygen from various electronic states. With the exception of the $O(^1S)$ state, another two are $O(^1D)$ and $O(^3P)$. $O(^3P)$ has three sub-states, namely $O(^3P_0)$, $O(^3P_1)$ and $O(^3P_2)$. Several emissions are produced by the quantum transition from higher energy state to lower state, such as the red line at 630 nm from the $O(^1D\text{-}^3P_2)$ transition. The green line is much more prominent than the emissions arising from $O(^1S\text{-}^3P)$ transitions, which can be determined by

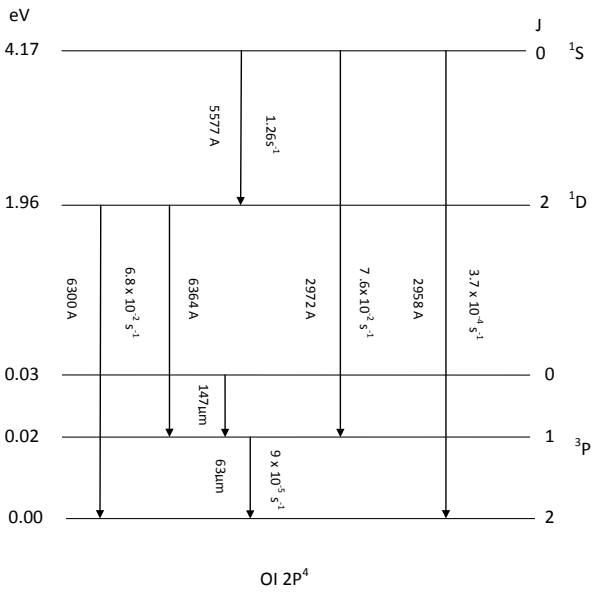

Figure 2.2: Radiative transitions between $O(^1S)$, $O(^1D)$ and $O(^3P)$. Arrows indicate directions of the quantum transition. (*Khomich et al.*, 2008)

the Einstein coefficient (the green line: A_{5577}=1.26 s^{-1}).

$$O(^1S) \xrightarrow{A_{5577}} O(^1D) + h\nu_{5577} \quad \text{(R2.8)}$$

$$O(^1S) \xrightarrow{A_{2958}} O(^3P_2) + h\nu_{2958} \quad \text{(R2.9)}$$

$$O(^1S) \xrightarrow{A_{2977}} O(^3P_1) + h\nu_{2977} \quad \text{(R2.10)}$$

A_{5577}, A_{2958} and A_{2977} are the Einstein coefficients for the transitions $O(^1\text{S-}^1\text{D})$, $O(^1\text{S-}^3\text{P}_2)$ and $O(^1\text{S-}^3\text{P}_1)$, respectively. The lifetime of $O(^1\text{S})$ can be represented as the inverse of the Einstein coefficient $A_{O_{1S}}$ (= A_{5577} + A_{2958} + A_{2977}). Beside spontaneous emissions, $O(^1\text{S})$ can also be de-excited by collisional quenching with O, O_2 and N_2.

$$O(^1S) + O \xrightarrow{k_{O_{1S}O}} O + O \quad \text{(R2.11)}$$

$$O(^1S) + O_2 \xrightarrow{k_{O_{1S}O_2}} O_2 + O \quad \text{(R2.12)}$$

$$O(^1S) + N_2 \xrightarrow{k_{O_{1S}N_2}} N_2 + O \quad \text{(R2.13)}$$

$k_{O_{1S}O}$, $k_{O_{1S}O_2}$, and $k_{O_{1S}N_2}$ are the reaction rate constants for $O(^1\text{S})$ quenching by O (Eq. R2.11), O_2 (Eq. R2.12) and N_2 (Eq. R2.13), respectively. Above reactions are generally relevant to the excitation and de-excitation of $O(^1\text{S})$.

2.3 Green line photochemical models

$O(^1\mathrm{S})$ is excited by chemical reactions and de-excited by spontaneous emissions or collisional quenching with $O(^3\mathrm{P})$, O_2, and N_2. The green line emission of $O(^1\mathrm{S})$ can be calculated by a numerical model taking into account the various excitation and de-excitation processes assuming steady state conditions, i.e., that the production and loss processes balance each other. Since the production of $O(^1\mathrm{S})$ is a two-step process, this needs to be applied for O_2^* and $O(^1\mathrm{S})$, resulting in the product of the two terms describing the production of the two states, respectively.

$$[O_2^*](A_{O_2^*} + k_{O_2^*O_2}[O_2] + k_{O_2^*N_2}[N_2] + k_{O_2^*O}[O]) = k_{OOM}[O]^2[M] \quad (2.14)$$

$$[O(^1S)](A_{O_{1S}} + k_{O_{1S}O_2}[O_2] + k_{O_{1S}O}[O] + k_{O_{1S}N_2}[N_2]) = k'_{O_2^*O}[O][O_2^*] \quad (2.15)$$

Therefore, abundances of O_2^* and $O(^1\mathrm{S})$ can be obtained:

$$[O_2^*] = \frac{k_{OOM}[O]^2[M]}{A_{O_2^*} + k_{O_2^*O_2}[O_2] + k_{O_2^*N_2}[N_2] + k_{O_2^*O}[O]} \quad (2.16)$$

$$[O(^1S)] = \frac{k'_{O_2^*O}[O][O_2^*]}{A_{O_{1S}} + k_{O_{1S}O_2}[O_2] + k_{O_{1S}O}[O] + k_{O_{1S}N_2}[N_2]} \quad (2.17)$$

The green line volume emission rate can be expressed as:

$$V_{1S} = [O(^1S)]A_{5577} \quad (2.18)$$

The symbols marked by square brackets represent species concentrations. The quenching of $O(^1\mathrm{S})$ by O and O_2 at 96 km are around $k_{O_{1S}O}[O]$=4.1 s^{-1} and $k_{O_{1S}O_2}[O_2]$=0.2 s^{-1}. The quenching of $O(^1\mathrm{S})$ by N_2 is not efficient ($k_{O_{1S}N_2}[N_2] \leq 8.2\times10^{-4}$ s^{-1} at 96 km) and is therefore often neglected (*Gobbi et al.*, 1992).

Equation 2.18 contains several rate constants, which are not known very well. This led to the situation that some rate constants in equation 2.18 were summarized in some studies (see below). This allowed to fit their values by the inter-comparison of different measurement techniques (resonance fluorescence and green line data) to obtain atomic oxygen abundance. From a molecular dynamics point of view, the upper atmosphere was considered in some way as a big laboratory to improve our knowledge about the rate constants involved.

The most prominent study in this context was the ETON rocket campaign (*Greer et al.*, 1986; *McDade et al.*, 1986). The outcome of this study was a simplified version of equation 2.18 and a set of rate constants giving a consistent picture of the multiple measurement techniques involved. The resulting model is usually known as the ETON model (hereinafter also referred to as 'eton') (*McDade et al.*, 1986; *Murtagh et al.*, 1990):

$$V_{1S}^{ETON} = \frac{A_{5577} k_{OOM} [O]^3 [M]}{(A_{O_{1S}} + k_{O_{1S}O_2}[O_2])(C_1[O] + C_2[O_2])} \tag{2.19}$$

In their model, C_1 and C_2 are fitting parameters. C_1 is relevant to the

quenching of O_2^* and $O(^1S)$ by atomic oxygen and C_2 is related to the quenching by O_2. Due to the almost constant O_2/N_2 mixing ratio, quenching by these two molecules (O_2 and N_2) is not distinguished in the ETON model. The ETON model has been validated by *Murtagh et al.* (1990) to assess the validity of proposed O and O_2 nightglow excitation parameters by *McDade et al.* (1986) by using a series of simultaneously measured green line and $O_2(b^1\Sigma_g^+ - X^3\Sigma_g^-)(0,\ 0)$ atmospheric band emissions by rocket-borne instruments. The assessment was performed in such a way that the measured green line emissions are compared with the simulated green line emissions from oxygen atmospheric band measurements using the proposed airglow parameters. *Murtagh et al.* (1990) found that they are in good agreement with each other under most conditions. It is worth noting that a systematic error may be inevitable to derive the atomic oxygen abundance from green line measurements utilizing these proposed parameters because the models of O_2 A-band and $O(^1S)$ rely on the same precursor states (O_2^*) and are not independent with each other (*Murtagh et al.*, 1990). A minor modification of the ETON model by adding the quenching of $O(^1S)$ by atomic oxygen and nitrogen was performed by *Gobbi et al.* (1992) in order to retrieve atomic oxygen from rocket green line measurements at Natal (5.8°S, 35.2°W) in December 1985 and November 1986. The deviations of the derived atomic oxygen abundances are less than 5% in comparison to the ETON model based on our calculation. The analysis of WINDII $O(^1S)$ green line observations

utilizing the ETON model gave a consistent picture with OH(8-3) $P_1(3)$ emissions observed by the same instrument (*Russell*, 2003), strongly supporting the choice of rate constants and fitting parameters utilized in the ETON model.

The second model considered in this work, compiled by *Khomich et al.* (2008) (the 'Khomich model', hereinafter also referred to as 'kho'), follows equation 2.18 in every detail, except for the quenching of $O(^1\mathrm{S})$ by N_2, which is regarded as irrelevant by several authors. This leads to the following expression:

$$\mathrm{V}_{1S}^{Kho} = \frac{A_{5577} k_{OOM} k'_{O_2^* O} [O]^3 [M]}{(A_{O_{1S}} + k_{O_{1S}O_2}[O_2] + k_{O_{1S}O}[O])(A_{O_2^*} + k_{O_2^* O_2}[O_2] + k_{O_2^* N_2}[N_2] + k_{O_2^* O}[O])} \tag{2.20}$$

The Khomich model has never been applied until now to retrieve atomic oxygen from global green line measurements.

A third model was introduced by *von Savigny and Lednyts'kyy* (2013) and *Lednyts'kyy et al.* (2015) (the 'Lednyts'kyy model', hereinafter also referred to as 'led'). This model is based on the ETON model but with significantly enhanced quenching by atomic oxygen. This model is currently under revision (v. Savigny and Lednyts'kyy, personal communication) and not considered in this work.

2.4 Quantitative analysis of different O(^{1}S) models

The two models introduced in the previous section lead to different $O(^1S)$ abundances. A quantitative analysis of the differences broken down into the individual processes involved is presented in this chapter. The numerical simulations presented here are based on the MSIS background atmosphere for mid latitudes and solar minimum conditions (for details see Figure 2.3). Other conditions are presented in the next section.

Volume emission rates (VERs) simulated by the ETON model is generally larger below 103 km, and smaller at higher altitudes (Figure 2.4). The $O(^1S)$ VERs peak at around 97 km and are 42% larger for the ETON

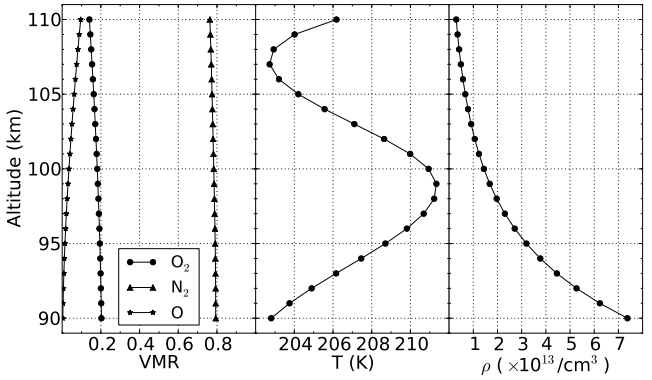

Figure 2.3: Profiles of O, O_2 and N_2 volume mixing ratios (VMR), as well as temperature (T) and total number density (ρ), from the MSIS empirical model at local solar time 10 p.m., 15, October, 2009, 25°N.

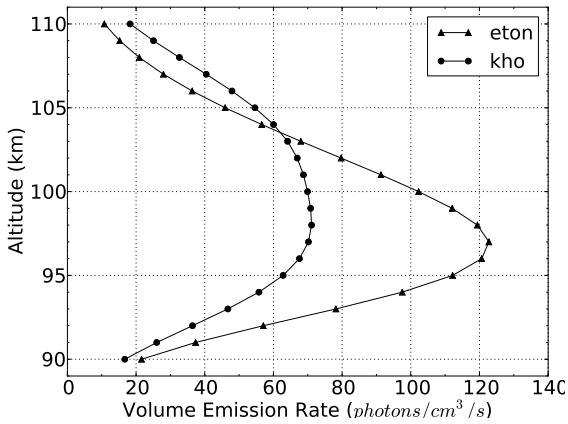

Figure 2.4: Profiles of volume emission rate simulated by the Khomich model (kho) and the ETON model (eton) for the atmospheric condition shown in Figure 2.3.

model simulations in comparison to VERs calculated by the Khomich model.

To detail the model differences, the loss terms in equations 2.19 and 2.20 are sorted into terms that are either constant, linearly or quadratically dependent on the various species abundances. They are rearranged in such a way that the relevant terms in the denominator of each model can be directly compared. These terms contain products of rate constants with (a): Einstein coefficient times N_2 or O_2 abundance; (b): N_2 or O_2 abundance squared; (c): Einstein coefficient and N_2 or O_2 abundance times O abundance; (d): Einstein coefficients squared. A compilation of these terms is given in Table 2.1.

Table 2.1: Rearranged loss terms for the ETON model and the Khomich model.

Term	Khomich	ETON
(a)	$\{A_{O_{1s}}(k_{O_2^*O_2}[O_2]+k_{O_2^*N_2}[N_2])$ $+A_{O_2^*}k_{O_{1s}O_2}[O_2]\}/k'_{O_2^*O}$	$C_2A_{O_{1s}}[O_2]$
(b)	$\{k_{O_{1s}O_2}[O_2](k_{O_2^*O_2}[O_2]+k_{O_2^*N_2}[N_2])\}/k'_{O_2^*O}$	$C_2k_{O_{1s}O_2}[O_2][O_2]$
(c)	$\{(k_{O_2^*O_2}[O_2]+k_{O_2^*N_2}[N_2]+k_{O_2^*O}[O]+A_{O_2^*})k_{O_{1s}O}[O]$ $+(k_{O_{1s}O_2}[O_2]+A_{O_{1s}})k_{O_2^*O}[O]\}/k'_{O_2^*O}$	$C_1(k_{O_{1s}O_2}[O_2]+A_{O_{1s}})[O]$
(d)	$A_{O_2^*}A_{O_{1s}}/k'_{O_2^*O}$	-

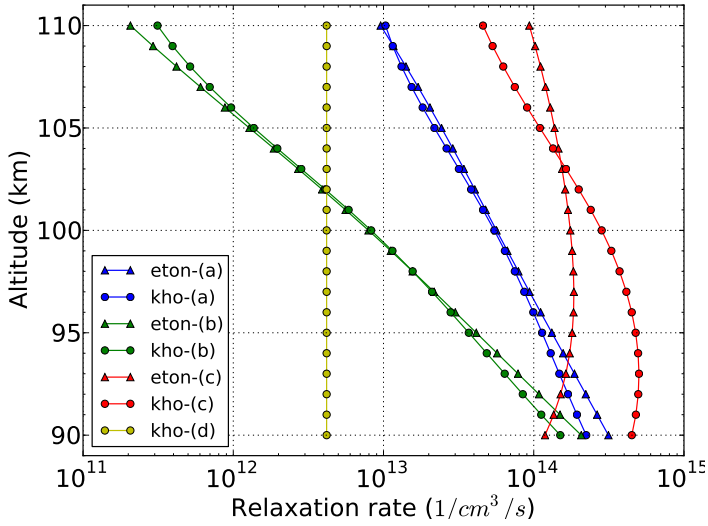

Figure 2.5: Profiles of the terms listed in Table 2.1 using the MSIS background atmosphere shown in Figure 2.3.

Figure 2.5 displays the altitude profiles of the different terms. The terms (a) and (b) are almost the same for each model. Large differences between the models show up in term (c). To determine which terms in (c) differ the most, a more detailed breakdown of the various components in this term has been performed and the results are illustrated in Table 2.2 and Figure 2.6. The largest difference between the models is the relaxation rate depending on the product of $[O]$ and $[O_2]$. This term is greatest at low altitudes and decreases with altitude, following the abundance of species involved. In the ETON model, this rate is about a factor of 10 smaller than in the Khomich model. The second relaxation term considered in the models is proportional to the Einstein coefficients and atomic oxygen abundance. This term is quite small in the Khomich model and about a factor of 10 larger in the ETON model. It is important at high altitudes, where relaxation via O_2 collisions is no longer relevant. The third of these is a term dependent on atomic oxygen density squared. Its vertical shape is determined by the abundance of atomic oxygen, peaking at about 100 km. It is not considered in the ETON model but it is also negligible in the Khomich model in comparison to other terms. Regarding the altitude shape of the total relaxation, the ETON model exhibits a somewhat flatter profile than the Khomich model. This will later result in a steeper decrease in the retrieved atomic oxygen profile at around the $[O]$ maximum altitude than for the Khomich model.

Since most of the terms analyzed above depend on the background at-

Table 2.2: Detailed breakdown of components in term (c) for the different photochemical models.

Term	**Khomich**	**ETON**
$[O][O_2]$	$k_{O_{1s}O}(k_{O_2^*O_2}[O_2]+k_{O_2^*N_2}[N_2])[O]/k'_{O_2^*O}$ $+k_{O_{1s}O_2}k_{O_2^*O}[O_2][O]/k'_{O_2^*O}$	$C_1 k_{O_{1s}O_2}[O_2][O]$
$A[O]$	$(A_{O_2^*}k_{O_{1s}O}+A_{O_{1s}}k_{O_2^*O})[O]/k'_{O_2^*O}$	$C_1 A_{O_{1s}}[O]$
$[O][O]$	$k_{O_2^*O}k_{O_{1s}O}[O][O]/k'_{O_2^*O}$	-

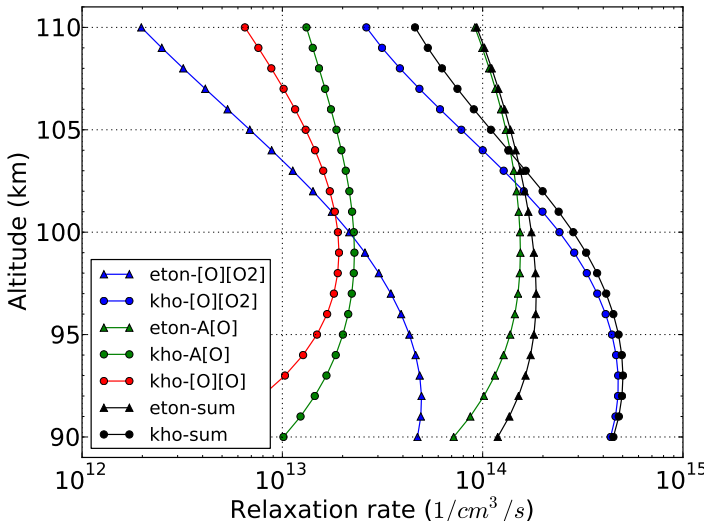

Figure 2.6: Profiles of relaxation rates in Table 2.2 for different models using the MSIS background atmosphere shown in Figure 2.3. The value of term (c) is given by a sum.

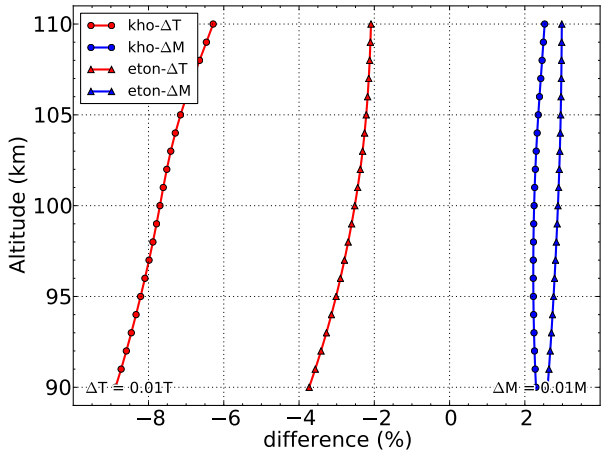

Figure 2.7: Differences of volume emission rates due to a 1% perturbation of temperature (T) and total density (M) for the two photochemical models.

mosphere, model differences will likely change for different atmospheric conditions. To analyse the overall sensitivity of simulated VERs on background atmospheric conditions, temperature and total density were perturbed and the resulting VER change is illustrated in Figure 2.7. Generally, VERs are anti-correlated with temperature and correlated with total density. The Khomich model shows a larger temperature sensitivity, which results from the adoption of temperature-dependent rate constants. VER simulated by the Khomich model decrease by 8% for a 1% increase in temperature (at 96 km), whereas the ETON model shows a weaker temperature dependence (3% decrease) in comparison to the Khomich model, which results from the adoption of simplified fitting parameters for the

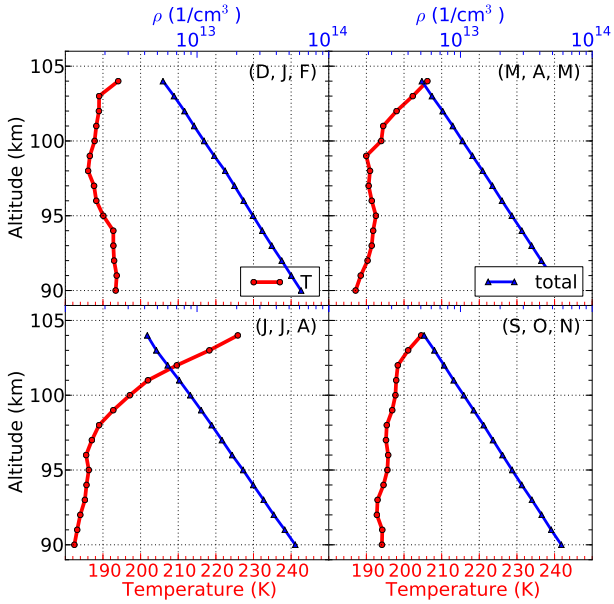

Figure 2.8: Temperature (red dot line) and total density (blue triangle line) profiles derived from SABER (between 9 p.m. and 11 p.m. local time) for four seasons in the year 2009 at 22.5°N. The profiles have been sampled at SCIAMACHY geo-locations.

ETON model. The dependence on the total density of the two models is fairly small (2-3% for a 1% change in total density).

To investigate to which extent the two $O(^1S)$ model fields differ in the course of a year, simulations for different atmospheric conditions as measured by SABER (Figure 2.8) are performed. Comparing temperature and total density for the different seasons reveals that between 90 and 100 km temperatures are around 190 K in winter and spring, and around 5 K higher in fall. In summer, temperature is 4–8 K lower than in winter

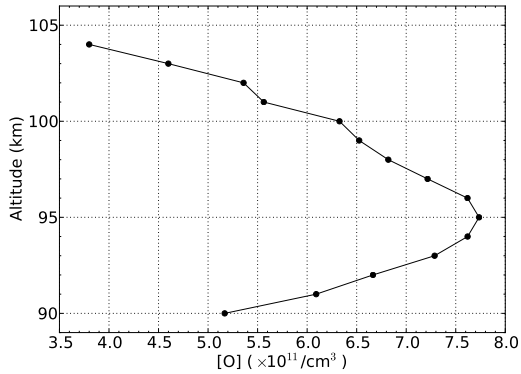

Figure 2.9: SABER atomic oxygen abundances for autumn in 2009 at 22.5°N.

and spring. The summer mesopause temperature is caused by adiabatic upward transport in the mesosphere (*Smith*, 2012b). Deviations are less than 10% at different seasons for SABER total densities. The mixing ratios of O_2 and N_2 are set to be 0.21 and 0.78, respectively. Atomic oxygen abundance is derived from SABER data (Figure 2.9) and peaks at around 95 km with the maximum concentration $7.7 \times 10^{11}/cm^3$.

The resulting volume emission rate profiles are shown in the left part of each panel of Figure 2.10. Solid lines in the right part of each panel of Figure 2.10 show percentage differences between the simulated results. As shown in Figure 2.4, VERs simulated by the Khomich model are larger than for the ETON model above around 96 km but smaller below this altitude. Below 100 km, the VERs simulated by the ETON model and the Khomich model agree within 25%. Above 100 km, the two model sim-

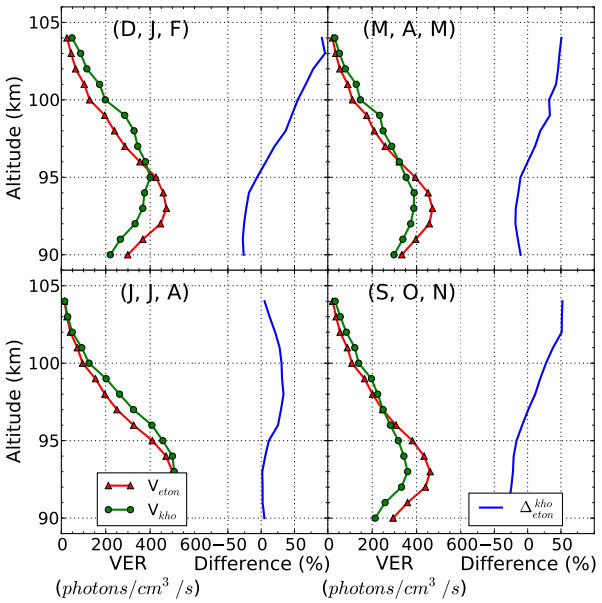

Figure 2.10: Volume emission rate profiles simulated by the ETON (eton) and Khomich (kho) models using SABER (sa) background atmosphere for four seasons in the year 2009 at 22.5°N. In each panel, left part: volume emission rate; right part: differences of volume emission rates (Δ^{kho}_{eton}: $\frac{V_{kho}-V_{eton}}{V_{eton}} \times 100$).

ulations can differ up to 100%. For summer conditions, the differences at high altitudes are significantly smaller (30% instead of 100%). As a general rule, $O(^1S)$ VERs and temperature are anti-correlated.

Chapter 3

Nighttime OH airglow emission measurements and modeling

Hydroxyl (OH) airglow emissions are produced by spontaneous transitions of excited hydroxyl molecules (OH^*). The transitions mainly happen within the same ground electronic state but with different initial and final vibrational and rotational states. The identification of OH emission bands in the nightglow was first understood by *Meinel* (1950) and, therefore, they are also called Meinel bands. They can be observed between 550 and 4400 nm and are most intense in the near infrared region. The emission layer peaks at around 87 km and extends about 8 km vertically (*Baker and Stair*, 1988; *Parihar*, 2008; *Gao et al.*, 2010).

3.1 Hydroxyl emission measurements

Hydroxyl airglow emissions have been widely observed by various ground-based photometers, spectrometers and interferometers since confirmed by *Meinel* (1950) (*Sivjee et al.*, 1972; *Offermann and Gerndt*, 1990; *Takahashi et al.*, 1996; *Greet et al.*, 1998; *Takahashi et al.*, 2002; *Liu et al.*, 2015). These remote-sensing measurements were used to derive rotational temperature and to investigate various wave signatures, such as gravity waves, tides, planetary waves, as well as seasonal and long-term variations (e.g., *Deutsch and Hernandez*, 2003; *Bittner et al.*, 2002; *Offermann et al.*, 2010; *French and Klekociuk*, 2011; *Das*, 2011; *Reid et al.*, 2014).

Hydroxyl emissions have been observed by rocket-borne photometers to investigate vertical and horizontal structures of the *OH* emission layer (*Baker and Stair*, 1988; *Clemesha and Takahashi*, 1996; *Hecht et al.*, 2004) and dynamical processes (dynamical transport and turbulent mixing) acting in the emission layer (*Hecht et al.*, 2004). *Baker and Stair* (1988) summarized rocket-borne hydroxyl airglow measurements from 34 rocket flights conducted by various investigators from 1956 to 1984 and found that the hydroxyl emission layer is about 8.4 km thick with a centre at around 87.4 km. Some of these measurements have been used to derive atomic oxygen abundances. *Good* (1976) was the first to derive atomic oxygen abundances from rocket-borne nighttime *OH* airglow

measurements. *McDade and Llewellyn* (1988) proposed expanded procedures for inferring atomic oxygen abundances from nighttime $OH(v$=7, 8, 9) Meinel band measurements and demonstrated that an effect of uncertainties of the unknown parameters on the atomic oxygen abundance was minor. *Hecht et al.* (2004) utilized OH(9-4) band emissions measured in TOMEX to derive atomic oxygen concentrations based on ground-based Na lidar measurements and TIME-GCM simulations (Chapter 3).

Different hydroxyl Meinel bands have been observed by many spaceborne instruments until now. For example, OH(9-4) band emissions were measured by the HRDI instrument (*Burrage et al.*, 1997) aboard the UARS and OH(9-3) band emission lines centred at 630 nm were observed by the ISUAL instrument aboard the FORMOSAT-2 satellite (*Nee et al.*, 2010). Other satellite measurements have been described in Chapter 1. Several of them have been utilized by different investigators to derive atomic oxygen abundances. *Russell* (2003) utilized OH(8-3) $P_1(3)$ emissions observed by the WINDII instrument aboard the UARS from 1991 to 1997 to infer atomic oxygen abundances. *Sheese et al.* (2014) derived atomic oxygen by using nighttime OH(5-1, 8-3, 9-4) band airglow emission measurements observed by OSIRIS aboard the Odin satellite. *Smith et al.* (2010) and *Mlynczak et al.* (2013b) inferred atomic oxygen from OH(8-6, 9-7) (2.0 μm) band emissions measured by Channel A of the SABER instrument aboard the TIMED satellite.

Hyperspectral *OH* emission data from the SCIAMACHY instrument

on Envisat were presented by *Kaufmann et al.* (2008). These data were used to derive chemical heating rates (*Kaufmann et al.*, 2010) and atomic hydrogen abundances (*Kaufmann et al.*, 2013). These data were also used by *von Savigny et al.* (2012) to investigate *OH* emission peak altitudes for different vibrational levels and *OH* relaxation mechanisms. A typical limb spectrum derived from SCIAMACHY channel 6 measurements is displayed in Figure 3.1. The emissions in the spectrum mainly belong to five *OH* Meinel bands (*OH*(2-0, 3-1, 4-2, 8-5, 9-6)). They are collected together by their band name using red line. The spectral range of *OH* emission bands may overlap with each other and we do not distinguish them clearly here. It is found that emissions emitted from *OH* lower vibrational states (*OH*(2-0, 3-1, 4-2)) are on average stronger than for

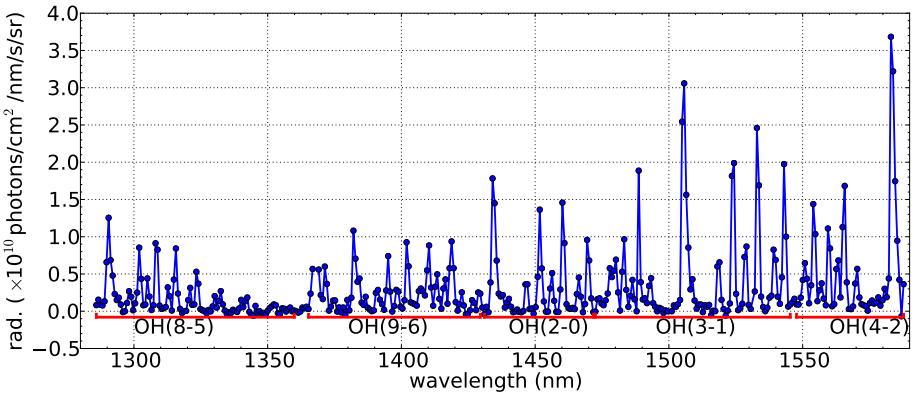

Figure 3.1: Limb spectrum derived from SCIAMACHY channel 6 measurements at tangent altitude around 86 km on April 5th, 2011 (119.8°E, 10.5°S).

higher vibrational states (OH(8-5, 9-6)).

3.2 Hydroxyl nightglow modeling

The exothermic reaction of H and O_3 was identified in the atmosphere by *Bates and Nicolet* (1950) to give rise to the major source of vibrationally excited OH^*.

$$H + O_3 \xrightarrow{k_{HO_3}} OH^* + O_2 \tag{R3.1}$$

k_{HO_3} represents the rate constant of the reaction R3.1. The numerical values of k_{HO_3} and the following rate constants are given in Table tab-4, tab-5 and tab-6 in Appendix A.4. The production rate of vibrationally excited OH^* is

$$P_{OH^*} = k_{HO_3} \cdot [H] \cdot [O_3] \tag{3.2}$$

The symbols marked by squared brackets are concentrations of corresponding species.

Hydroxyl radical is a diatomic molecule and has two electronic ground sub-states, namely $X^2\Pi_{\frac{3}{2}}$ and $X^2\Pi_{\frac{1}{2}}$, which result from a coupling of the electron spin and the orbital angular momentum (spin-splitting) (*Rousselot et al.*, 2000). Several percent larger population for $X^2\Pi_{\frac{3}{2}}$ levels in comparison to $X^2\Pi_{\frac{1}{2}}$ levels was recently reported by *Noll et al.* (2015) and further investigations are necessary. Therefore, it is assumed

here that excited hydroxyl radicals are equally distributed over the two electronic sub-states. The reaction R3.1 releases sufficient energy to populate excited OH up to the ninth vibrational level. It is common to give the nascent production rate ($P_0(v \leq 9)$) of a particular vibrational state, weighted by a distribution factor (or branching ratio) f_v:

$$P_0(v) = f_v \cdot P_{OH^*} \tag{3.3}$$

Several nascent production rates have been published (*Charters et al.*, 1971; *Ohoyama et al.*, 1985; *Klenerman and Smith*, 1987; *Adler-Golden*, 1997) and the rates derived by *Adler-Golden* (1997) are used here (For details, please refer to Appendix A.2).

The metastable excited hydroxyl radicals (OH^*) can be de-excited via radiative, chemical, and collisional relaxation processes. The radiative relaxation scheme is relevant to spontaneous emissions of OH^* and can be evaluated by Einstein coefficients ($A_{v,v'}$, $v' \leq v$).

$$OH(v) \xrightarrow{A_{v,v'}} OH(v') + h\nu \tag{R3.4}$$

v and v' are hydroxyl vibrational states before and after de-excitation, respectively. Several Einstein coefficient databases are available (*Mies*, 1974; *Langhoff et al.*, 1986; *Turnbull and Lowe*, 1989; *Goldman et al.*, 1998; *van der Loo and Groenenboom*, 2007; *Rothman et al.*, 2013). Einstein coefficients published by *van der Loo and Groenenboom* (2007) and

Rothman et al. (2013) are the latest two. In the following, the two Einstein coefficients are named as Trans and HITRAN, respectively. HITRAN is used in this work and, additionally, Trans is used for comparison. The reasons are detailed in Appendix A.3.

The vth vibrational state production rate due to radiative decay from a higher vibrational state v'' ($v < v'' \leq 9$) can be obtained:

$$P_{rad}(v) = N(v'') \cdot \sum_{v''>v}^{9} A_{v'',v} \tag{3.5}$$

where, $N(v'')$ is the total density of v''th vibrational state. Its loss rate to the v'th ($0 \leq v' < v$) vibrational state due to radiative decay can also be derived:

$$L_{rad}(v) = N(v) \cdot \sum_{v'=0}^{v-1} A_{v,v'} \tag{3.6}$$

where, $N(v)$ is the total density of vth vibrational state.

The partitioning of the chemical (Eq. R3.7) (*Makhlouf et al.*, 1995; *Russell*, 2001) and collisional (Eq. R3.8) (*Adler-Golden*, 1997) loss of $OH(v)$ with atomic oxygen is under discussion. Collisions with atomic oxygen tend to de-excite $OH(v)$ directly into the ground state, without exciting any intermediate states (*Adler-Golden*, 1997; *Kaufmann et al.*, 2008; *Smith et al.*, 2010; *Xu et al.*, 2012; *von Savigny et al.*, 2012). In principle, there are three relaxation schemes discussed in literature. They differ in the change of vibrational quantum numbers associated with a

collision of $OH(v)$ with N_2, O_2 or O. These three quenching schemes have been presented to simulate hydroxyl chemical and collisional relaxation processes (*McDade and Llewellyn*, 1987; *Adler-Golden*, 1997). The first one is a sudden-death quenching model. The key point of this model is that the excited hydroxyl molecule is directly de-excited to the ground state and loses its vibrational energy completely in a single step. The second one is a single-quantum quenching model. The change of quantum numbers is confined to $\Delta v = 1$, that is, the quenching ends up populating vibrational state $v' = v - 1$ from v. The last one is a multi-quantum quenching model. The lower vibrational states are populated in such a way that only a portion of excited hydroxyl radicals is quenched to each lower state. Rate constants for the multi-quantum model were determined by *Adler-Golden* (1997) using an exponential vibrational number gap scaling. A discussion regarding these three quenching models is given in Appendix A.4.

It is preferable to combine these three relaxation models together to account for quenching of $OH(v)$ by a collision with N_2, O_2 or O (*Adler-Golden*, 1997; *Kaufmann et al.*, 2008; *von Savigny et al.*, 2012). The sudden death model is used for quenching of $OH(v)$ by O. The corresponding rate constant derived from SABER OH nightglow measurements by *Xu et al.* (2012) is used here (Table tab-4). N_2 is an inefficient quencher for $OH(v)$ ($k_{N_2,(v,v')} \propto 10^{-13}$ cm^3/s) but the quenching of $OH(v)$ by O_2 is quite efficient ($k_{O_2,(v,v')} \propto 10^{-11}$ cm^3/s) (*Adler-Golden*, 1997). Therefore,

the single-quantum model is applied for the quenching of $OH(v)$ by N_2 and the multi-quantum model is adopted for the quenching of $OH(v)$ by O_2. This mixture has also been recommended by *Adler-Golden* (1997); *Kaufmann et al.* (2008); *von Savigny et al.* (2012) after their investigation to the $OH(v)$ relaxation mechanisms. The corresponding rate constants used by *Mlynczak et al.* (2013b) to derive atomic oxygen from SABER *OH* nightglow measurements are applied in this work (Table tab-5 and tab-6).

$$OH(v) + O \xrightarrow{k_{OHO}} H + O_2 \tag{R3.7}$$

$$OH(v) + O \xrightarrow{k_{O,(v,v')}} OH(v') + O \tag{R3.8}$$

$$OH(v) + O_2 \xrightarrow{k_{O_2,(v,v')}} OH(v') + O_2 \tag{R3.9}$$

$$OH(v) + N_2 \xrightarrow{k_{N_2,(v,v')}} OH(v') + N_2 \tag{R3.10}$$

k_{OHO}, $k_{O,(v,v')}$, $k_{O_2,(v,v')}$, and $k_{N_2,(v,v')}$ are the rate constants of reactions R3.7, R3.8, R3.9, and R3.10, respectively. The production and loss rates of excited hydroxyl radicals ($v \geq 1$) due to collisional quenching are as follows:

$$P_{col}(v) = N(v'') \cdot \sum_{v''>v}^{9} \left(k_{O,(v'',v)} \cdot [O] + k_{O_2,(v'',v)} \cdot [O_2] + k_{N_2,(v'',v)} \cdot [N_2]\right) \tag{3.11}$$

$$L_{col}(v) = N(v) \cdot \sum_{v'=0}^{v-1} \left(k_{O,(v,v')} \cdot [O] + k_{O_2,(v,v')} \cdot [O_2] + k_{N_2,(v,v')} \cdot [N_2]\right) \tag{3.12}$$

In addition, the loss rate contributed by the chemical reaction (R3.7) is

$$L_{che} = N(v) \cdot k_{OHO} \cdot [O] \tag{3.13}$$

The continuity equation can be used to describe the hydroxyl concentration variation in the vibrational quantum state v.

$$\frac{\partial N(v)}{\partial t} = P(v) - L(v) - N(v) \cdot (\nabla \cdot \vec{V}) \tag{3.14}$$

where, $N(v)$ is the total density of vth vibrational state and $P(v)$ is the total production rate of $OH(v)$ due to different relaxation processes. $L(v)$ is the total photochemical and collisional loss rate of $OH(v)$ and plays an important role in $OH(v)$ losses. $N(v) \cdot (\nabla \cdot \vec{V})$ represents the diffusion loss rate of $OH(v)$ and $\vec{V}$ is the velocity field. We need to verify the importance of each mechanism in the UMLT region.

A horizontal homogeneous atmosphere is assumed here to investigate photochemical and dynamical processes in the mesosphere. Vertical winds are generally less than 1 m/s in the mesosphere (*Xu and Smith*, 2003). For $OH(v)$ molecules, the vertical transport time scale is larger than 100 s with a 1 m/s vertical wind assumed and its diffusion time scale is much larger than 1000 s (*Xu et al.*, 2012). The lifetime varies from 1 ms for $OH(v = 9)$ to 30 ms for $OH(v = 1)$ at 85 km (*Xu et al.*, 2012). Therefore, the photochemical and collisional reactions are much faster than dynamical transport and diffusion. Thus, the hydroxyl radicals are

in chemical equilibrium for each vibrational level and $N(v) \cdot (\nabla \cdot \vec{V})$ can be neglected. On time-scales larger than the individual lifetime of each vibrational level (< 1s), the assumption of the steady state condition is feasible for all *OH* vibrational levels in the mesosphere, that is $\frac{\partial N(v)}{\partial t} = 0$.

Under the photochemical equilibrium, the total production rate equals the photochemical and collisional losses.

$$P(v) = L(v) \tag{3.15}$$

where,

$$P(v) = P_0(v) + P_{rad}(v) + P_{col}(v) \tag{3.16}$$

$$L(v) = L_{rad}(v) + L_{col}(v) + L_{che} \tag{3.17}$$

Except the *OH* 9th vibrational state, the production rates $P(v < 9)$ are not only populated by direct chemical exciting production, but also come from photochemical and collisional de-excitation of higher vibrational levels ($v < v'' \leq 9$). For the 9th vibrational state, the production rate P(v = 9) is only contributed by the chemical excitation ($P_0(v = 9)$).

Substituting for relevant terms in the equation 3.15 gives the total amount of hydroxyl molecule in vth (1st to 9th) vibrational quantum state,

$$N(v) = \frac{P_0(v) + \sum_{i=1}^{9-v} [A_{v+i,v} + k_{O,(v+i,v)} \cdot [O] + k_{O_2,(v+i,v)} \cdot [O_2] + k_{N_2,(v+i,v)} \cdot [N_2]] \cdot N(v+i)}{\sum_{i=0}^{v-1} [A_{v,i} + k_{O,(v,i)} \cdot [O] + k_{O_2,(v,i)} \cdot [O_2] + k_{N_2,(v,i)} \cdot [N_2]] + k_{OHO} \cdot [O]} \tag{3.18}$$

Due to the lack of knowledge about quenching of OH by O, both loss mechanisms (chemical and collisional loss) are kept here by adjusting rate constants (k_{OHO} and $k_{O,(v,i)}$) to switch off or on the mechanism.

Under thermal equilibrium condition, the hydroxyl radical rotational levels in each vibrational state follow the Boltzmann distribution with a rotational temperature T, which is assumed to be close to ambient kinetic temperature. Thus, the amount of hydroxyl radical for the (v, J) vibrational-rotational state is

$$N(v,J) = N(v)\frac{2(2J+1)}{Q_v(T)}exp(\frac{-hcE_v(J)}{kT}) \tag{3.19}$$

where, J is the total angular momentum which takes into account the angular momentum (N) and the electronic spin ($\pm\frac{1}{2}$) in such a way that J is equal to $N + \frac{1}{2}$ for the state $X^2\Pi_{\frac{3}{2}}$ and $N - \frac{1}{2}$ for the state $X^2\Pi_{\frac{1}{2}}$, h is the Planck constant, c is the speed of light, k is the Boltzmann constant, $E_v(J)$ is the rotational term value in cm^{-1} and $Q_v(T)$ is the rotational partition function

$$Q_v(T) = \sum_J 2(2J+1)exp(\frac{-hcE_v(J)}{kT}) \tag{3.20}$$

However, higher rotational levels ($J > 5.5$) of OH do not persist the local thermal equilibrium (LTE) hypothesis and these levels are overpopulated in comparison to predictions made under an assumption of the LTE (*Cosby and Slanger*, 2007; *Noll et al.*, 2015), which have been confirmed by OH nightglow measurements (*Pendleton et al.*, 1993; *Dodd et al.*,

1994). Therefore, only lower rotational levels ($J \leq 5.5$) were used by *Cosby and Slanger* (2007) and *Noll et al.* (2015) to derive rotational temperature from *OH* nightglow measurements. A more restrictive $J \leq 3.5$ is recommended by *Noll et al.* (2015) to persist the LTE and is applied in this work (see Table 3.1).

The Einstein coefficient ($A_{v,v'}$) used in equation 3.18 summarizes all the coefficients ($A^{(v,J)}_{(v',J')}$) of individual ro-vibrational transitions from the vth vibrational level to the v'th level. Assuming the rotational LTE, they can be thermally averaged:

$$A_{v,v'}(T) = \sum_{J}\sum_{J'} \frac{2(2J+1)}{Q_v(T)} exp(\frac{-hcE_v(J)}{kT}) A^{(v,J)}_{(v',J')} \tag{3.21}$$

where, $A^{(v,J)}_{(v',J')}$ characterizes the hydroxyl radical spontaneous emission probability from initial vibrational-rotational state (v, J) to final state (v', J'). $A_{v,v'}(T)$ depends weakly on temperature ($\sim$0.3% for a 50 K temperature variation) (*Xu et al.*, 2012). The whole radiative probability of the vth vibrational state can be derived as

$$A_v(T) = \sum_{v'}^{v-1} A_{v,v'}(T) \tag{3.22}$$

3.3 Methodology to derive atomic oxygen abundances from OH airglow measurements

The basic procedure to derive atomic oxygen abundance from OH^* nightglow measurements is based on the assumption of the chemical balance of ozone during nighttime. In the UMLT region, ozone is produced by the three-body recombination reaction of atomic and molecular oxygen:

$$O + O_2 + M \xrightarrow{k_{OO_2M}} O_3 + M \qquad \text{(R3.23)}$$

M represents background gases and k_{OO_2M} is the three-body recombination rate constant. The most important ozone destruction reaction is the equation R3.1 (*Moreels et al.*, 1977). Another minor ozone destruction reaction is

$$O + O_3 \xrightarrow{k_{OO_3}} O_2 + O_2 \qquad \text{(R3.24)}$$

k_{OO_3} is the rate constant of the reaction R3.24. This reaction contributes around 10% ozone loss in the nighttime (*Smith et al.*, 2008).

The lifetime of ozone depends on the ambient temperature and the atomic hydrogen abundance in the mesosphere and is generally less than a few minutes during night (*Smith and Marsh*, 2005). Therefore, it is a good approximation to assume that the production (reaction R3.23) of

ozone is balanced by its loss (reaction R3.1 and reaction R3.24) (*Smith and Marsh*, 2005; *Smith et al.*, 2008) and can be described by the following expression:

$$k_{OO_2M} \cdot [O] \cdot [O_2] \cdot \rho \approx k_{OO_3} \cdot [O] \cdot [O_3] + k_{HO_3} \cdot [H] \cdot [O_3] \tag{3.25}$$

where ρ is the background atmospheric total density. The second term on the right is proportional to the abundance of vibrationally (highly) excited OH^* and can be expressed by the OH^* production rate P_{OH^*} leading to the following term to obtain the atomic oxygen abundance:

$$[O] = \frac{P_{OH^*}}{k_{OO_2M} O_2 \rho - k_{OO_3}[O_3]} \tag{3.26}$$

The algorithm has been used by many investigators (*Russell*, 2003; *Smith et al.*, 2010; *Mlynczak et al.*, 2013b). The OH^* nightglow observations can be considered as an atomic oxygen proxy measurement. However, the retrieval procedure involves various rate constants, whose uncertainties affect the error budget of the derived atomic oxygen abundance. Suitable choice of the spectral window of the measurements avoids most of these uncertainties. In practice, the spectral window is restricted to emissions of the highest vibrational state of OH, which avoids most of the uncertainties associated with the relaxation pathways of OH. Therefore, SCIAMACHY OH(9-6) band emission measurements are used to derive atomic oxygen concentrations in Chapter 6 for the same purpose

(see Figure 3.1).

3.4 Quantitative analysis of *OH*(9-6) band simulations

The volume emission rate ($VER^{(v,J)}_{(v',J')}$) for each emission line can be derived (*Mies*, 1974)

$$VER^{(v,J)}_{(v',J')} = N(v,J) \cdot A^{(v,J)}_{(v',J')} \tag{3.27}$$

This equation is used to simulate volume emission rates (VERs) of individual lines in the *OH*(9-6) band. The accuracy of these radiances depends on the relevant uncertainties in the forward model which are related to the chemical balance of ozone and production and loss processes of *OH* vibrational level 9. Effects of using the Einstein coefficients and the ozone balance assumption are illustrated below.

Table 3.1: *OH*(9-6) band Einstein coefficients derived from HITRAN and Trans databases. Einstein coefficients are summed for each line due to unresolved Λ-type doublets.

Einstein coefficient	$O_1(1.5)$	$O_1(2.5)$	$Q_2(0.5)$	$P_2(1.5)$	$P_2(0.5)$	$P_1(1.5)$
HITRAN	62.64	25.88	35.68	67.72	73.16	45.80
Trans	54.09	22.23	30.85	58.95	63.49	39.81

Since the latest two Einstein coefficient databases are available, it is preferable to compare differences of OH(9-6) band simulations by a use of different Einstein coefficients. The used Einstein coefficients are given in Table 3.1. The HITRAN data is found approximately 13% larger than the Trans data for the OH(9–6) band Einstein coefficients. OH(9-6) band VERs between 1377–1400 nm can be simulated from equation 3.27 based on the two Einstein coefficients (Figure 3.2). OH(9-6) VERs show a Gaussian shape peaking at an altitude of 87 km with a half width of 8–10 km. VERs based on the HITRAN Einstein coefficients are generally 13% larger than for the Trans Einstein coefficients. It is found that differences

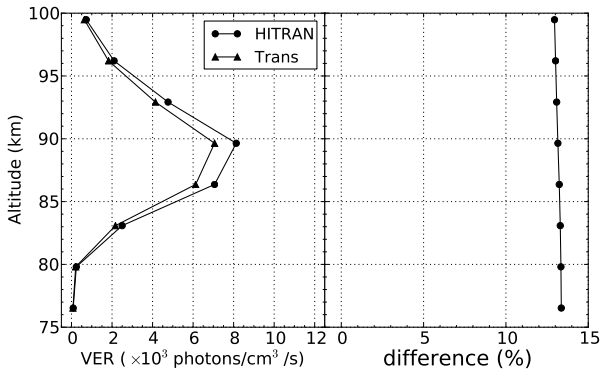

Figure 3.2: Simulations of $OH(9-6)$ band volume emission rates (left panel) between 1377–1400 nm using HITRAN and Trans Einstein coefficients and percentage differences (right panel). The background atmosphere is derived monthly mean SABER measurement at 9–11 p.m. and 35°N–40°N for November, 2005. O_2 and N_2 volume mixing ratios are 0.21 and 0.78, respectively.

of Einstein coefficients could nearly linearly map to the simulated VERs, which is caused by a similar $9th$ radiative probability $A_9(T)$ ($\sim$199.25 s^{-1} at 200 K) derived from HITRAN and Trans.

The ozone loss due to collisions with atomic oxygen is small compared to the loss due to reaction with atomic hydrogen, as stated above. Therefore, some atomic oxygen retrieval schemes neglect this process completely (*Russell*, 2003; *Mlynczak et al.*, 2013b). VERs are affected by this approximation by 1% at 90 km and up to 12% at 100 km (Figure 3.3).

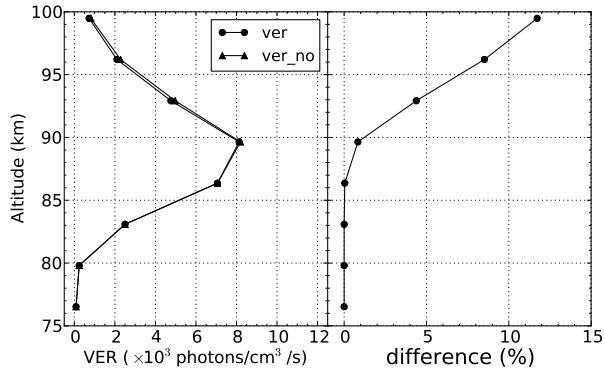

Figure 3.3: Simulations of $OH(9-6)$ band volume emission rates (left panel) between 1377–1400 nm and percentage differences (right panel). Triangle line shows the VERs without considering the ozone loss due to collisions with atomic oxygen. The background atmosphere is the same with the one used in Figure 3.2.

Chapter 4

Retrieval approach

The retrieval can be regarded as an approach to solve an inverse problem in the presence of indirect measurements of interested properties. Generally, the inverse problem is ill-conditioned and may not have a unique solution. A method how to solve an ill-conditioned inverse problem has been thoroughly presented by *Rodgers* (2000).

First of all, a forward model $\boldsymbol{F}$ is needed, which simulates the actual measurements $\boldsymbol{y}$. The forward model $\boldsymbol{F}$ maps the state vector onto radiance measurements under consideration of the real physical processes, influences of the instrument and all the other constraints based on our understanding of the measurements. It is a frequent practice to distinguish forward model parameters $\boldsymbol{b}$ and state variables $\boldsymbol{x}$ which, in the field of atmospheric remote sensing, consists of abundance of trace gases, temperature, instrument line shape, etc. The latter are those quantities, which are fitted in the inversion process, while the former are model parameters,

which need to be known a-priori. This leads to the following expression:

$$\boldsymbol{y} = \boldsymbol{F}(\boldsymbol{x}, \boldsymbol{b}) + \boldsymbol{\varepsilon} \tag{4.1}$$

Seen from optimal estimation theory, the error term $\boldsymbol{\varepsilon}$ represents stochastic measurement errors, only. In most retrievals, it includes also systematic measurement uncertainties as well as forward model parameter uncertainties.

4.1 Inverse issue

From an abstract point of view, the inverse solution of equation 4.1 is the following expression:

$$\boldsymbol{x} = \boldsymbol{F}^{-1}(\boldsymbol{y}) \tag{4.2}$$

However, $\boldsymbol{F}^{-1}$ cannot be given explicitly in many cases. The solution of the inverse problem is often not unique due to the measurement error $\boldsymbol{\varepsilon}$.

It is common to solve the inverse problem by minimizing the differences between the forward model simulations and the actual measurements utilizing a mathematical norm, namely the cost function (χ^2):

$$\min\{[\boldsymbol{F}(\boldsymbol{x}) - \boldsymbol{y}]^T \mathbf{S}_{\varepsilon}^{-\mathbf{1}} [\boldsymbol{F}(\boldsymbol{x}) - \boldsymbol{y}]\} \tag{4.3}$$

where, $\mathbf{S}_{\varepsilon}$ represents a covariance matrix of the measurement noise. To

guarantee the uniqueness of a physically meaningful solution, a regularization term is added to the cost function by introducing an a-priori state $\boldsymbol{x_a}$:

$$\chi^2 = [\boldsymbol{F}(\boldsymbol{x}) - \boldsymbol{y}]^T \mathbf{S}_\varepsilon^{-1} [\boldsymbol{F}(\boldsymbol{x}) - \boldsymbol{y}] + (\boldsymbol{x} - \boldsymbol{x}_a)^T \mathbf{S}_\mathbf{a}^{-1} (\boldsymbol{x} - \boldsymbol{x}_a) \tag{4.4}$$

where, $\mathbf{S_a}$ is defined as the covariance matrix of the a-priori state $\boldsymbol{x}_a$ in optimal estimation theory.

4.1.1 Tikhonov regularisation

As pointed out above, the regularisation is often adopted to dampen influences of measurement noise on the retrieval results. In general, it combines a regularisation matrix $\mathbf{S}_\mathbf{a}^{-1}$ and the a-priori state $\boldsymbol{x}_a$ which reflects priori knowledge of an atmospheric state. However, in many cases realistic covariances ($\mathbf{S_a}$) are not available and other regularization operators are applied.

Tikhonov regularisation (*Tikhonov and Arsenin*, 1977) is applied in this work. In general, a Tikhonov regularization matrix can be considered as the superposition of a diagonal matrix and several extra-diagonal matrices. The diagonal matrix is called a zero-order Tikhonov matrix ($\mathbf{L_0}$). It constrains the absolute value of the solution. $\mathbf{L_1}$ is the first order derivative operator. It is often used as an extra-diagonal matrix, playing the role to smooth the state vector by means of the first order derivatives with

respect to altitude.

The inverse covariance matrix $\mathbf{S_a^{-1}}$ and Tikhonov regularization matrices are related through the following expression:

$$\mathbf{S_a^{-1}} = \mathbf{L^T L} = w_0 \mathbf{L_0^T L_0} + w_1 \mathbf{L_1^T L_1} + w_2 \mathbf{L_2^T L_2} + \cdots w_n \mathbf{L_n^T L_n} \qquad (4.5)$$

where, w_0, w_1, w_2, ..., and w_n are positive weighting factors. $\mathbf{L_n}$ is the n-order derivative operator and n is 0, 1, 2, $\cdots$. The weighting factor should be constructed in such a way that the two different terms in equation 4.4 are more or less the same for the final solution. Several methods exist to obtain the optimal weighting factors, such as the L-curve criterion (*Hansen*, 1992). In this work, Tikhonov regularization is considered up to the 1st degree and the optimal weighting parameters are set 'ad hoc', as discussed in Appendix A.5.

4.1.2 Minimization algorithm

To minimize the cost function (Eq. 4.4), we apply the n-form Gauss-Newton iteration algorithm. The Gauss-Newton iteration is a first-order derivative Newton-type minimisation method (*Rodgers*, 2000).

$$\boldsymbol{x}_{i+1} = \boldsymbol{x}_a + (\mathbf{K_i^T S_\varepsilon^{-1} K_i} + \mathbf{S_a^{-1}})^{-1} \mathbf{K_i^T S_\varepsilon^{-1}} [\boldsymbol{y} - \boldsymbol{F}(\boldsymbol{x}_i) + \mathbf{K_i}(\boldsymbol{x}_i - \boldsymbol{x}_a)] \quad (4.6)$$

where, $\mathbf{K_i}$ is the first derivative matrix of the forward model, the Jacobian matrix, $\frac{\partial \boldsymbol{F}(\boldsymbol{x}_i)}{\partial \boldsymbol{x}}$. The algorithm converges quickly in the vicinity of the minimum (*Madsen et al.*, 2004; *Lourakis and Argyros*, 2005).

4.2 Diagnostics

Diagnostic quantities are essential to evaluate the quality of the retrieval, such as the averaging kernel, contribution matrix, resolution, errors, and degrees of freedom. A thorough discussion is presented by *Rodgers* (2000).

4.2.1 Averaging kernel and contribution matrix

The solution of a regularized inversion problem, as described above, will have some bias associated with the regularization applied. Since the strength of the regularization is linked to the measurement covariance error, the latter affects the solution as well. In retrieval theory, it is common to distinguish the 'true' solution $\boldsymbol{x}$ of an inverse problem and what is obtained from the regularized problem ($\boldsymbol{x_r}$):

$$\boldsymbol{x_r} = (\mathbf{I_n} - \mathbf{A})\boldsymbol{x_a} + \mathbf{A}\boldsymbol{x} + \mathbf{G}\boldsymbol{\varepsilon} \tag{4.7}$$

Two fundamental quantities in this context are

$$\mathbf{G} = (\mathbf{S_a^{-1}} + \mathbf{K^T S_\varepsilon^{-1} K})^{-1} \mathbf{K^T S_\varepsilon^{-1}} \tag{4.8}$$

$$\mathbf{A} = \mathbf{GK} \tag{4.9}$$

The contribution matrix $\mathbf{G}$ is the pseudo inverse of $\mathbf{K}$ with the regularisation and quantifies the sensitivity of the retrieval result to the measurement. The averaging kernel $\mathbf{A}$ ideally is an identity matrix, describing the sensitivity of the retrieval result to the true atmospheric state, on the other hand, to the regularization, and to the a-priori information. The sum over a row of the averaging kernel matrix quantifies the contribution of the measurement and is close to 1 for a well constrained retrieval (*Rodgers*, 2000).

The first term on the right hand side of the equation 4.7 can be interpreted as the contribution from the a-priori state and should be kept as small as possible for the retrieval result. The second term describes the contribution of the true atmospheric state. The third term is the retrieval error, caused by the measurement noise $\boldsymbol{\varepsilon}$.

For limb measurements, the averaging kernel row for a well constrained retrieval reaches maximal values at altitudes close to the corresponding tangent altitudes of the measurement. The full width at half maximum (FWHM) of this distribution characterizes the spatial resolution of the measurement. This resolution gives an insight into the amount

of smoothing introduced by the inversion. The reciprocal of the diagonal entry of **A** indicates the information content of the measurement for the grid element.

4.2.2 Errors

A retrieved quantity is affected by different sources of uncertainty. First of all, it depends on the uncertainty of the forward model parameter. This was addressed in the previous chapters and will be quantified in the following chapters. The forward model parameters mainly consist of rate constants and Einstein coefficients in the work. Their resulting uncertainties can be obtained by an expression:

$$\mathbf{S_f} = \mathbf{G}\mathbf{K_b}\mathbf{S_b}\mathbf{K_b^T}\mathbf{G^T} \tag{4.10}$$

where, $\mathbf{K_b}$ is the Jacobian matrix of forward model parameters and $\mathbf{S_b}$ is a covariance matrix for the forward model parameter error. The uncertainty resulting from each parameter is calculated individually and a root sum square of these individual uncertainties quantifies the leading error of forward model parameters. Other sources of uncertainty are relevant to the regularization strategy, the a-priori information, and the measurement noise, in which way the regularization affects the retrieval result. For the Tikhonov regularization, the smoothing error mainly comes from

the derivative operators in the equation 4.5.

$$\mathbf{S_s} = (\mathbf{A} - \mathbf{I})\mathbf{S_a}(\mathbf{A} - \mathbf{I})^{\mathbf{T}} \tag{4.11}$$

In contrast, the retrieval noise is easier to evaluate than the smoothing error, determined by $\mathbf{G}\boldsymbol{\varepsilon}$. In general, the noise $\boldsymbol{\varepsilon}$ is normally unbiased and its covariance can be reconstructed as a diagonal matrix $\mathbf{S}_\varepsilon$. Thus, the retrieval noise can be expressed as

$$\mathbf{S_m} = \mathbf{G}\mathbf{S}_\varepsilon\mathbf{G}^{\mathbf{T}} \tag{4.12}$$

The total error due to regularization smoothing and measurement noise is

$$\mathbf{S} = \sqrt{\mathbf{S_s}^2 + \mathbf{S_m}^2} = (\mathbf{K}^{\mathbf{T}}\mathbf{S}_\varepsilon^{-\mathbf{1}}\mathbf{K} + \mathbf{S_a^{-1}}) \tag{4.13}$$

Some other errors can also be quantified when its covariance matrix is available, such as the forward model error, due to the approximation of the correct physics behind the model. All the errors can be classified as random or systematic errors dependent on their variabilities between consecutive measurements, but they may change their attributes due to the time scale. Generally, retrieval noise is regarded as a random quantity, while the smoothing introduced by regularisation is considered as a systematic error.

4.2.3 Degrees of freedom

After a solution was found, the cost function χ^2 is normally expected to be equivalent to the number of measurements or the number of degrees of freedom. *Rodgers* (2000) distinguishes between d_s, which attributes to the state known as "degrees of freedom for signal", and d_n, which results from measurement noise called as "degrees of freedom for noise" from χ^2. Thus,

$$\chi^2 = d_s + d_n \tag{4.14}$$

where,

$$d_s = trace([(\mathbf{S_a^{-1}} + \mathbf{K^T S_\varepsilon^{-1} K})^{-1} \mathbf{K^T S_\varepsilon^{-1} K}]) = trace(\mathbf{A}) \tag{4.15}$$

$$d_n = trace([(\mathbf{S_a^{-1}} + \mathbf{K^T S_\varepsilon^{-1} K})^{-1} \mathbf{S_a^{-1}}]) \tag{4.16}$$

Chapter 5

Atomic oxygen retrieved from SCIAMACHY O(^{1}S) green line measurements

In this chapter, the implementation of the retrieval of the atomic oxygen abundance is described in the UMLT region using the $O(^1S)$ forward model introduced in Chapter 2, the limb observations of SCIAMACHY at 557 nm and the retrieval approach presented in the previous chapter. Data pre-filtering, the actual retrieval setup, and the retrieval performance are described. A detailed uncertainty analysis is performed. The resulting data are analyzed with respect to its spatial and temporal distribution.

5.1 Monthly zonal mean green line limb measurements

Due to the low signal-to-noise ratio (on the order of 1, see Figure 5.4) of the SCIAMACHY green line observations, monthly averaged zonal mean data are needed for all subsequent analyses. Envisat is a sun-synchronous-orbit satellite and goes across polar regions. Therefore, a portion of limb measurements is contaminated by aurora in the polar region and energetic particles in the South Atlantic Anomaly (SAA). Auroral $O(^1\mathrm{S})$ green line emission is responsible for the contamination in the polar region and the production of $O(^1\mathrm{S})$ is most likely owing to the dissociative recombination of O_2^+ and electrons ($O_2^+ + e \rightarrow O + O(^1S)$) (*Shepherd et al.*, 1995). SAA located roughly at (50°S, 10°N) and (100°W, 40°E) and has an increased particle background owing to the weak geomagnetic field. Thus, the $O(^1\mathrm{S})$ green line emission can be enhanced due to the electron precipitation in SAA (*Wiens et al.*, 1999). The introduced $O(^1\mathrm{S})$ forward model in Chapter 2 is invalid to simulate these contaminated green line emissions. Therefore, the contaminated measurements should be screened out first.

To avoid these contaminations, some procedures are necessary to screen contaminated measurements out before zonal averaging is performed. Firstly, spectral radiance correction was performed by subtracting an offset, which is calculated by averaging measurement spectral ra-

diances above 115 km, from each limb measurement below 115 km. No green line emissions are found to be observed by SCIAMACHY above this altitude through a visual inspection.

Secondly, profiles located at (50°S, 10°N) and (100°W, 40°E) are excluded to avoid the effects of SAA. Thirdly, for the purpose of screening out the influenced profiles by aurora, the aurora effect should be considered along the entire line of sight of the observation near the polar region. An empirical aurora model developed by *Zhang and Paxton* (2008) was used to simulate the aurora activity at the observation time. The empirical model was trained with global Far UltraViolet (FUV) measurements by the Global UltraViolet Imager (GUVI) aboard the TIMED satellite. It depends on the Kp index and local magnetic time, only. The Kp index can excellently quantify the disturbances in the geomagnetic field. Model output is the mean energy and energy flux of precipitating electrons in the aurora oval. Figure 5.1 represents an aurora oval simulation for a Kp index 3 as an example. The aurora oval is shaped around the geomagnetic pole in both hemispheres by the geomagnetic field and, therefore, a ring structure can be found in Figure 5.1. In the following analysis, all profiles are excluded, which were measured at geo-locations with low electron precipitation at a mean energy larger than 0.1 keV. The empirical value of 0.1 keV was chosen here after testing several mean energy values as the threshold and, then, the aurora effect is found negligible along the line of sight for limb measurements.

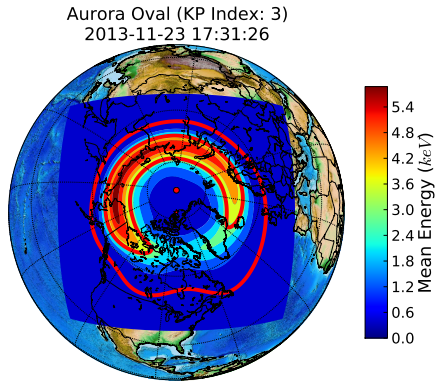

Figure 5.1: Mean electron energy as simulated with the aurora model for 17:31 UTC, 23, Nov, 2013. The Kp index is 3. The color bar indicates the value of the mean energy flux. The red contour lines indicate the 0.1 keV (outside) and 3 keV (inside) mean energy of precipitating electrons, respectively.

The effect of filtering out spectra contaminated by high energy electrons can be clearly seen in zonal mean green line data (Figure 5.2). The entire profile is enhanced and a strong green line signal can be observed up to the middle thermosphere for these cases. Filtering out these regions makes the zonal mean profiles look very similar to mid- an low- latitude data, as expected.

After screening out all contaminated profiles, the largest and smallest 5% of the measurements (10–100 measurements) at each sampling point are discarded before averaging in order to screen out outliers. Then, the total number of profiles in each latitude bin is illustrated in Figure 5.3

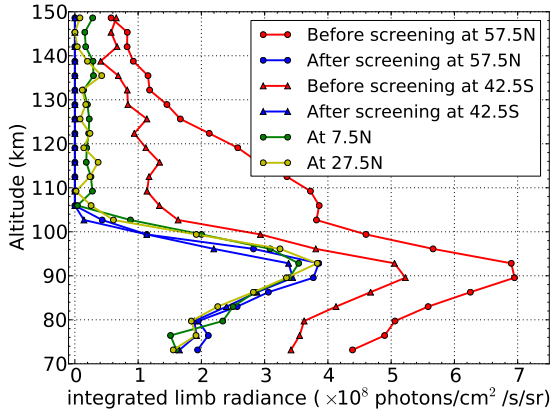

Figure 5.2: Spectrally integrated green line limb radiance profiles at 42.5°S and 57.5°N before and after screening out the aurora effects. Profiles at 7.5°N and 27.5°N are also given for comparison. The data were averaged over 5° in latitude and 1 month in time.

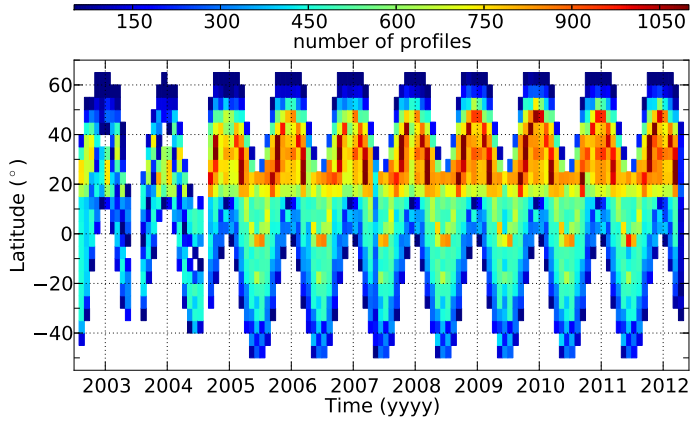

Figure 5.3: The number of zonally averaged profiles in each latitude bin from August 2002 to April 2012.

for the operational time of SCIAMACHY. The latitudinal coverage of the nighttime limb spectra is from about 50°S to 60°N. The restriction of the latitudinal coverage in comparison to the ground track of the satellite is caused by the seasonality of solar illumination and various calibration measurements made at the night-side of the satellite orbit. The amount of nighttime limb measurements increased significantly in 2004 due to a change in the SCIAMACHY instrument operations (e.g., *Kaufmann et al.*, 2010). Generally, the number of averaged profiles for each latitude bin is small in most cases at these latitudes (e.g. 50°N), but rises up to 1000 at certain latitudes and times.

The quality of the zonal mean spectra can be evaluated by calculating standard deviations of averaged spectra at each sampling point. Figure 5.4 displays the zonal mean spectra and their standard deviations at 96 km for different latitudes, as well as the median spectra for comparison. The noise error of individual spectra is around 0.6×10^9 photons/s/cm^2/sr/nm. The signal-to-noise ratio is around 1 at low latitudes and rises up to 2 at middle latitudes for the raw measurements. For the zonal mean spectra, the signal-to-noise ratio is significantly enhanced and reaches up to approximately 35 at 32.5°N. In addition, median and mean spectra show a consistent picture, indicating that the data determination stated above is feasible.

The spectra were averaged from October, 2002 to April, 2012 based on the procedure presented above. These mean spectra were used to de-

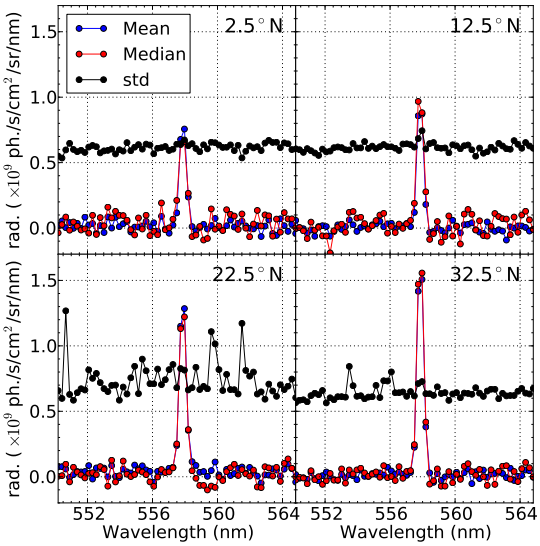

Figure 5.4: Limb radiances of zonal mean spectra and their standard deviations as measured by SCIAMACHY at 96 km in October, 2005. The median spectra is also given.

rive atomic oxygen abundances. Figure 5.5 displays a typical profile of the measured $O(^1S)$ zonal mean spectra for several altitudes for October 2008 at 20°N–25°N. Reasonable signal-to-noise values (S/N>1) are obtained up to about 102 km. The largest S/N is found to be approximately 20 at around 92 km and the measurement S/N below 92 km is also larger than 12, which is caused by the line-of-sight across the green line peak emission layer at around 96 km.

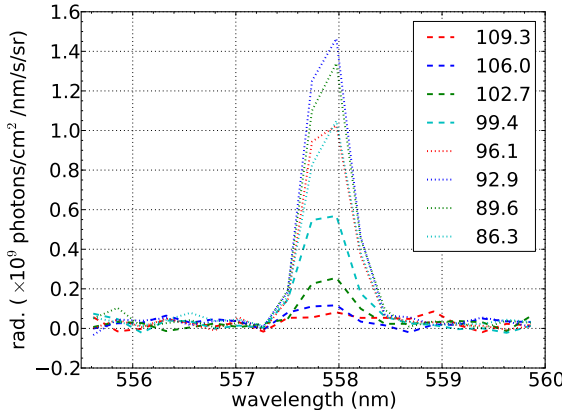

Figure 5.5: SCIAMACHY monthly zonal mean limb green line spectra for October 2008 at 20°N–25°N. The tangent altitudes (km) of the spectra are shown in the legend.

5.2 Atomic oxygen retrieval

5.2.1 Retrieval

A description of the retrieval set up is given first. The O_2 and N_2 volume mixing ratios needed in the forward model were taken from MSIS. Atomic oxygen initial guess and a-priori values were taken from MSIS, as well. Temperature and total density data were derived from co-located SABER measurements at 9–11 p.m.. The ETON model were used. The retrieval altitude grid is the same as tangent altitudes of the line of sight, which differ by less than 20 m along the year for similar latitudes (*von Savigny et al.*, 2012). The altitude regime is set at 73–115 km. The mea-

surement noise covariance is represented by the noise covariance at 552–557 nm and 559–564 nm for each spectrum.

The optimal estimation method presented in Chapter 4 was used to derive atomic oxygen abundances from the SCIAMACHY green line measurements. A global fit approach is used, i.e., an entire profile of atomic oxygen is used to simulate a sequence of limb green line emission spectra at 555.5–559.8 nm to fit the measurements. A combination of zero- and first- order Tikhonov regularization (*Tikhonov and Arsenin*, 1977) was applied here to integrate into the cost function to stabilize the retrieval. A detailed discussion of the regularization term construction is described in Appendix A.5. The baseline regularisation strength is adjusted in such a way that the altitude resolution of the retrieved values is of the order of the instrumental vertical field of view (about 3.3 km).

A retrieval procedure is implemented based on the typical profile of green line measurements stated above at 20°N–25°N for October, 2008. Atomic oxygen abundances, radiative offsets, a green line spectral peak position, and a instrument line shape are the derived quantities. The latter two parameters are set to be constant with altitude. The values of radiative offset are all around -5.0×10^6 photons/cm^2/s/sr/nm. The FWHM of the instrument line shape is 0.449 nm and no spectral shift ($\delta\lambda < 0.1$ nm) is found.

The atomic oxygen abundances derived from these measurements are presented in Figure 5.6. Only values at 89.6–106.0 km are shown in the

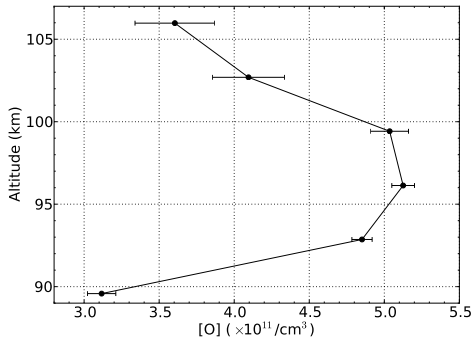

Figure 5.6: Zonal mean atomic oxygen abundance derived from SCIAMACHY green line measurements at 20°N–25°N for October, 2008 based on the ETON model. Error bars represent the statistical uncertainty due to the measurement noise.

figure, which are thought to be derived from reliable SCIAMACHY measurements. Causes will be illustrated later. The atomic oxygen abundance peaks at around 96 km and reaches up to $5.1 \times 10^{11}/\mathrm{cm}^3$. Error bars indicate the statistical uncertainty due to the measurement noise.

5.2.2 Retrieval diagnostics

The vertical profile of these measured spectrally integrated radiances is displayed in Figure 5.7. The radiances peak at around 93 km and reach up to 8.0×10^8 photons/cm^2/s/sr. Measurement errors are consistent in the altitude regime. The derived parameters are used to simulate the measured radiances as well. The simulations and the measurements show a consistent picture above 85 km. Deviations below 85 km may result from

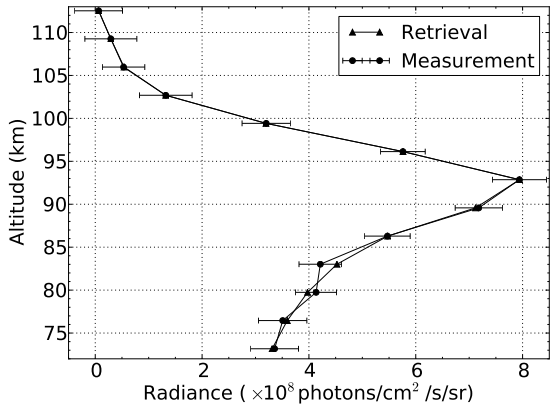

Figure 5.7: Integrated green line limb radiances derived from measurements and simulations at 20°N–25°N for October, 2008. Error bar indicates the measurement noise.

derived atomic oxygen abundances which are thought to be not realistic below 89 km.

Diagnosing the retrieval results is performed following the procedure introduced in Chapter 4. Six degrees of freedom for the signal are found in the data. Figure 5.8 represents the averaging kernel (Figure 5.8(a)) and the vertical resolution profile (Figure 5.8(b)) of the retrieval. Rows of the averaging kernel are shown from 89.6 km to 106.0 km and one row corresponds to one tangent altitude. The peak value of each curve below 105 km equals approximately to 1 at its corresponding tangent altitude, indicating that derived atomic oxygen abundances are real and not the a-priori. Contributions from adjacent tangent point measurements are negligible. However, the peak value at 106 km is around 0.7 and a significant

contribution to the retrieval result comes from adjacent point measurements, resulting in a broadened vertical resolution (Figure 5.8(b)). Curves for tangent points below 89.6 km and above 106 km are not shown here, because no useful signals were obtained at these tangent points. Therefore, the retrieval results below 89 km and above 105 km are skipped, as shown in Figure 5.6. The vertical resolution in Figure 5.8(b) is represented by the full width of half maximum (FWHM) of each curve in Figure 5.8(a) and is given from 89.6 km to 106 km. All the resolution values are around 3.3 km and equals to the SCIAMACHY vertical field of view, except the resolution (4.6 km) at 106 km.

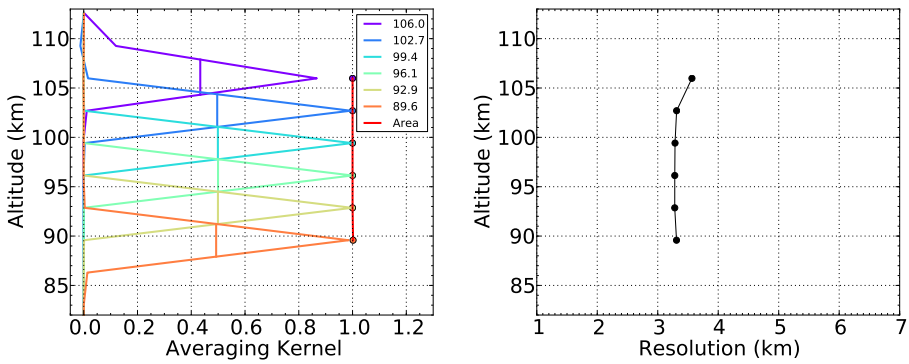

(a) Averaging kernel

(b) Vertical resolution

Figure 5.8: The averaging kernel and the vertical resolution of the retrieval. The curve labelled as 'Area' represents the sums over rows of the averaging kernel.

5.2.3 Systematic uncertainties of retrieved atomic oxygen

Systematic uncertainties stem from uncertainties in model parameters and uncertainties in background atmospheric parameters, which cannot be measured by SCIAMACHY. Thus, the uncertainty of the retrieved atomic oxygen abundance due to model parameter errors is evaluated using the uncertainties in the rate constants, given in Table tab-1, following the procedure introduced in Chapter 4. The uncertainty of $k_{O_1SO_2}$ is the largest one and reaches up to 41%. The uncertainty of k_{OOM} is 30% (for details refer to Appendix A.1). The uncertainties of C_1 and C_2 are around 5% and 13%, respectively. The Einstein coefficient uncertainties (A_{5577} and A_{O_1S}) are around 8%.

For retrieved atomic oxygen abundance, the largest source of uncertainty results from k_{OOM}: A 30% uncertainty affects retrieved atomic oxygen by about 11% at 90 km, which rises up to 14% at 106 km (Figure 5.9). The uncertainty of $k_{O_1SO_2}$ has a strong effect on the atomic oxygen uncertainty (up to $\sim$5%) at low altitudes. Uncertainties of all other forward model parameters together affect atomic oxygen by another 4.5% so that the overall (root sum square) error due to the rate constants is of the order of 13% at 90 km and 15% at 106 km.

To evaluate the effect of uncertainties in the background atmosphere, the real SABER temperature errors evaluated by *García-Comas et al.*

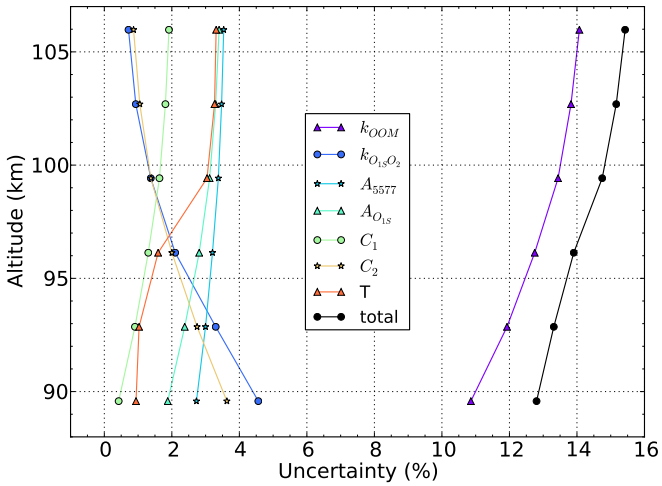

Figure 5.9: Percentage uncertainties of simulated atomic oxygen densities utilizing the ETON model due to the uncertainties in the individual rate constants (Table tab-1) and SABER temperature (T). The curve labelled as 'total' is the root sum square of individual errors. For details see text.

(2008) are adopted. The SABER kinetic temperature combined systematic error resulting from non-LTE kinetic parameters is within 1.5 K ($\sim$1%) below 95 km and within 4–5 K ($\sim$3%) at 100 km in general. The uncertainty in temperature affects the total density by 1% below 95 km and 3% at 100 km due to the hydrostatic equilibrium. Uncertainties in the volume mixing ratio of O_2 and N_2 are negligible. The uncertainty of temperature maps nearly linearly into the atomic oxygen uncertainty and it is around 1% at 89–95 km and 3% at 99–106 km. Adding temperature uncertainties results in an overall uncertainty of 13% at 90 km and 15% at 106 km, as shown in Figure 5.9. The smoothing error and the noise

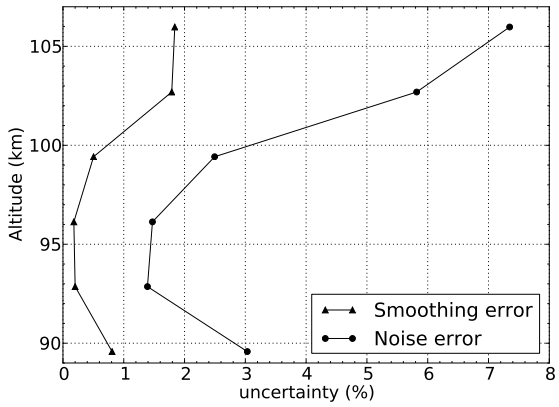

Figure 5.10: Percentage uncertainties of the smoothing error and the retrieval error.

error are generally below 3% except for the noise error (around 7% at 106 km) at the upper most altitudes (Figure 5.10), which is caused by the low signal to noise ratio of the measurements above 100 km. The noise error is larger than the smoothing error by a factor of 4.

5.2.4 Comparison to derived atomic oxygen based on the Khomich model

To assess the impact of the underlying $O(^1S)$ photochemical model, it is straightforward to derive atomic oxygen abundances from the same green line measurements but based on the Khomich model. All the setups are the same as stated above except the photochemical model. The atomic oxygen abundance uncertainty due to model parameter errors is

illustrated in Figure 5.11, firstly. Some authors do not specify the uncertainty of their rate constant measurements. In that case, we assume a 10% uncertainty for the rate constant, as *Sheese et al.* (2011) did when evaluating the uncertainty of atomic oxygen abundances derived from O_2 A-band airglow measurements by OSIRIS aboard the Odin satellite. The largest source of uncertainty, again, is due to k_{OOM}, resulting in around 14% uncertainty in atomic oxygen abundance. $k'_{O_2^*O}$, k_{O_1SO} and $k_{O_2^*N_2}$ are the important sources of uncertainty for the model parameters and an uncertainty of 10% for each parameter results in about 4% uncertainty in

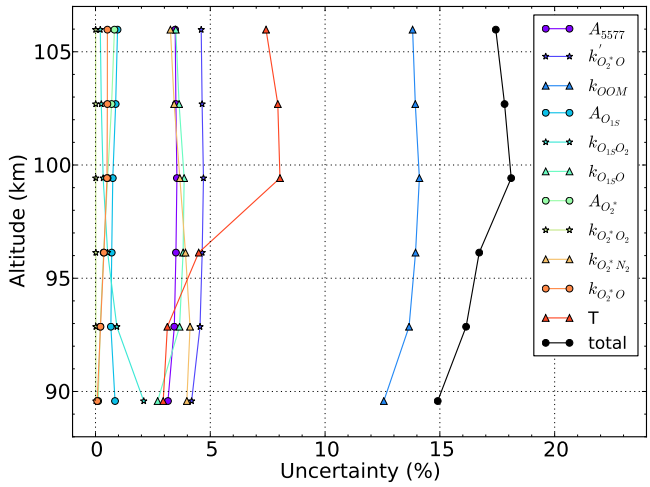

Figure 5.11: Percentage uncertainties of derived atomic oxygen abundances utilizing the Khomich model due to the uncertainties in the individual rate constants (Table tab-1) and SABER temperature (T). The curve labelled as 'total' is the root sum square of individual errors.

atomic oxygen abundance. The resulting atomic oxygen uncertainty due to A_{5577} is around 3%. Other rate constants affect retrieved atomic oxygen abundance weakly (<1%). The background temperature above 97 km leads to an uncertainty of around 8% for derived atomic oxygen. In summary, the total uncertainty of the retrieved atomic oxygen abundance due to model parameters and the background atmosphere is around 17%. In addition, the smoothing error is similar to the ETON one but the noise error is around 40% larger below 100 km (not shown).

For comparison, atomic oxygen abundances based on the ETON model (O^{scia}_{eton}) and the Khomich model (O^{scia}_{kho}) are also displayed in Figure 5.12. Atomic oxygen abundance uncertainties due to rate constants

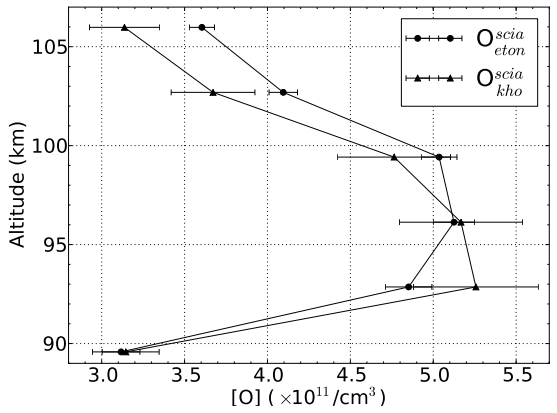

Figure 5.12: Atomic oxygen abundances (O^{scia}_{kho} and O^{scia}_{eton}) derived from the green line measurements at 20°N–25°N for October, 2008 based on the Khomich model and the ETON model. Error bars represent uncertainties due to rate constants which are different in the two models.

which are different in the two models are also given in error bars. O^{scia}_{eton} is approximately 12% larger than O^{scia}_{kho} above 96 km. O^{scia}_{kho} peak altitude is lower than for O^{scia}_{eton}. In addition, error bars indicate that O^{scia}_{kho} and O^{scia}_{eton} are consistent below 100 km.

5.3 Analysis of retrieval results

Atomic oxygen abundances have been derived from the near ten-year record of SCIAMACHY green line measurements. All the set-ups are kept the same as stated in last section and two atomic oxygen data sets were created: O^{scia}_{eton} and O^{scia}_{kho}. The two photochemical models (ETON and Khomich) lead to different atomic oxygen abundances as retrieved from the same SCIAMACHY measurements (see Figure 5.12). A validation and an intercomparison of the two datasets are performed below.

5.3.1 Retrieval validation

To assess an agreement of the retrieval results with model results, HAMMONIA (Hamburg Model of the Neutral and Ionized Atmosphere) perpetual runs performed by *Schmidt et al.* (2006) are used in this work. HAMMONIA is a general circulation model covering the atmospheric altitude range from the earth's surface up to an altitude of around 250 km (*Schmidt et al.*, 2006). Seasonal mean retrieved atomic oxygen profiles (O^{scia}_{eton} and O^{scia}_{kho}) in 2009 at 20°N–30°N are displayed in Figure 5.13.

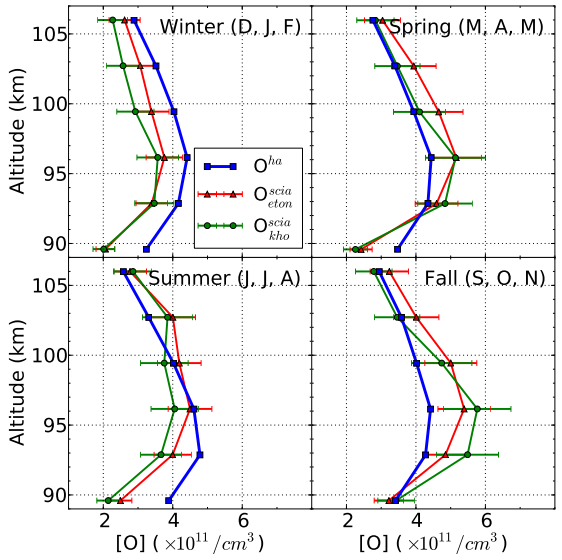

Figure 5.13: Profiles of the retrieved SCIAMACHY atomic oxygen based on the ETON and Khomich models for four seasons in 2009 at 20°N–30°N. Calendar months in each season are also given. For comparison, profiles derived from the HAMMONIA model are also provided. Uncertainties due to rate constants and measurement noises are given.

Also shown are corresponding HAMMONIA model data (O^{ha}) for perpetual solar minimum conditions.

Deviations of up to 20% are found when comparing retrieved atomic oxygen concentrations using the ETON model and the Khomich model (O^{scia}_{eton} and O^{scia}_{kho}). Peak abundances are 4–6$\times 10^{11}$/cm^3. The HAMMONIA atomic oxygen concentrations peak at 96 km with peak abundance around 4×10^{11}/cm^3, and are comparable to the retrieved SCIAMACHY atomic oxygen.

5.3.2 Latitudinal distribution of derived atomic oxygen datasets

The latitudinal distribution of atomic oxygen concentrations for 2009 based on the ETON model and the Khomich model are displayed in Figure 5.14 to investigate global similarities and differences of the two datasets. The atomic oxygen concentrations have been interpolated into 1.0 km altitude grid resolution from original 3.3 km grid. The derived atomic oxygen concentrations (O_{kho}^{scia} and O_{kho}^{scia}) show highest values at mid latitudes in both hemispheres and reach up to $8 \times 10^{11}/\mathrm{cm}^3$. During springtime, the peak concentration in the southern hemisphere is larger than in northern hemisphere. In autumn this imbalance is reversed. The altitude of the atomic oxygen peak varies with latitude. At mid latitudes it is at about 95 km, whereas it is about 5 km lower at equatorial latitudes. The lowered equatorial peak is connected to a deep depression of atomic oxygen about 8 km higher up. This pattern is especially prominent during equinox and results from vertical movements associated to solar tides (*Zhang and Shepherd*, 1999; *Smith et al.*, 2010). It was found by *Smith et al.* (2010) when analyzing local time variation of atomic oxygen volume mixing ratio (vmr) derived from SABER channel A (2.0 μm band emissions) measurements at 10°S–10°N.

The altitude–latitude cross sections of atomic oxygen abundances show pronounced spatial structures in both equinox and solstice seasons,

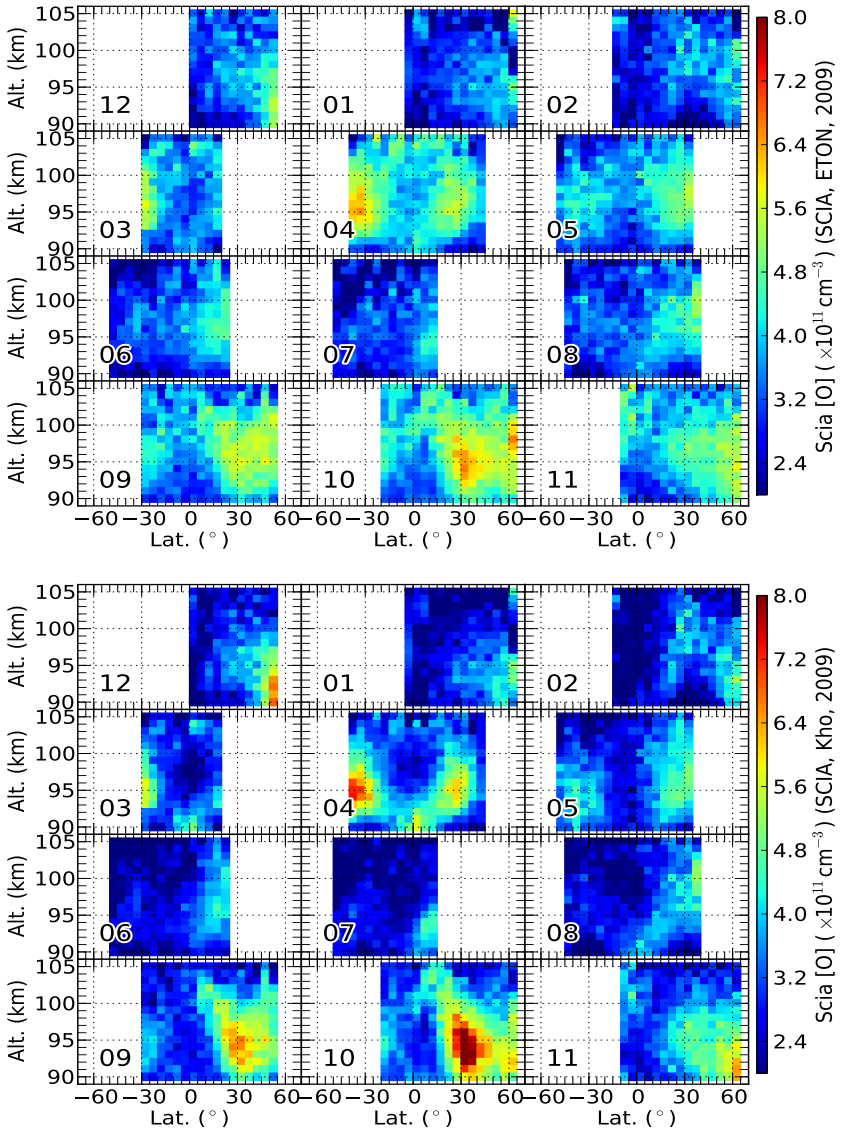

Figure 5.14: Latitude–altitude cross sections of atomic oxygen abundances retrieved from green line emission measurements of SCIAMACHY for the year of 2009 based on the ETON model (Top) and the Khomich model (Bottom). Numbers given in panels indicate the calendar months.

though these structures differ in shape. These structures coincide with similar shapes in the background temperature (Figure 5.15(a)). They are most likely caused by atmospheric tides, which transport the abundant atomic oxygen abundances from higher altitudes downward. Similar tidal structures in atomic oxygen were also observed by the WINDII and SABER instruments (see, for example, Figure 8 in (*Russell et al.*, 2005), or Figure 6 in (*Smith et al.*, 2010)). Both *Russell et al.* (2005) and *Smith et al.* (2010) identified the structures with the signature of the diurnal migrating tide characterized by a distinctive (1, 1) Hough mode latitudinal structure, with maximum amplitude over the equator and with two further maxima at 30°S and 30°N, but somewhat smaller amplitude and 180-degree phase-shifted.

Since similarities of the two datasets are discussed above, it is straightforward to analyze their differences. The maximum concentration of O_{kho}^{scia} is larger than for O_{eton}^{scia} at mid latitudes and the peak height of O_{kho}^{scia} is lower than for O_{eton}^{scia}, which was also found in Figure 5.13. However, concentrations of O_{kho}^{scia} are much smaller than for O_{eton}^{scia} over the tropical region at 95–105 km.

Latitudinal deviations of the two atomic oxygen data sets in April 2009 are given to illustrate the differences in detail (Figure 5.15(b)). Generally, atomic oxygen concentrations agree very well at mid latitudes and exhibit larger discrepancies in the tropical region. Deviations of retrieved atomic oxygen based on the ETON and Khomich models are typically

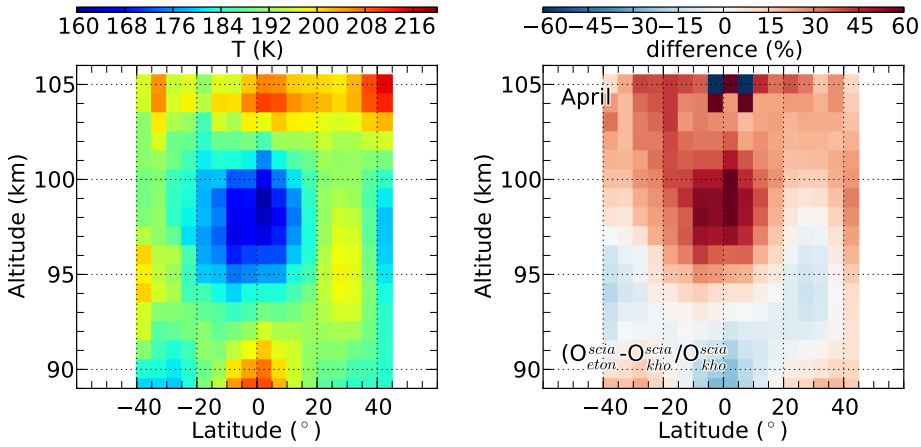

Figure 5.15: (a): Latitudinal SABER temperature for April, 2009. (b): Percentage deviations ((O^{scia}_{eton}-O^{scia}_{kho})/$O^{scia}_{kho}\times$100) of retrieved atomic oxygen concentrations using the ETON and Khomich models for April, 2009.

±20% below 100 km, as found in Figure 5.13, and 30% at higher altitudes, except for the tropics. Deviations are found up to 60% at 95–102 km and up to 30% in the vicinity of 90 km over the equatorial region. Since the photochemical models presented in the chapter 2 depend differently on temperature, some differences in the spatial distribution of atomic oxygen are imprinted by the temperature fields. High temperature leads to derive larger atomic oxygen abundances for the Khomich model than for the ETON model. By comparison to temperature fields (Figure 5.15(a)), a high correlation is found between structures of temperature and deviations.

5.4 Temporal variations of atomic oxygen abundances

The ten-year record of SCIAMACHY measurements offers a good opportunity to study long-term variations. The 10-year data record of retrieved atomic oxygen abundances at 20°N–25°N is presented in Figure 5.16(a). Other latitudes can be found in Figure fig-3 in Appendix A.6. On annual timescales, pronounced semi-annual (SAO) and annual (AO) variations are found in different latitudes. Multi-year variations are affected by the solar UV radiation. The production of atomic oxygen is directly driven by solar UV flux through the photolysis of molecular oxygen by the radiation of the Schumann-Runge continuum (135–175 nm) and the Schumann-Runge bands (175–242 nm). Recent observations of solar UV flux (*Yeo et al.*, 2014) indicate that solar radiation in the Schumann-Runge continuum and the Schumann-Runge bands varies about 28% and 4%, respectively, along the 23rd solar UV cycle. Model calculations (*Schmidt et al.*, 2006) predict that atomic oxygen volume mixing ratio (vmr) change about 4% along the solar cycle due to these changes in solar UV radiation (see later).

Since several publications (*Deutsch and Hernandez*, 2003; *Clemesha et al.*, 2005; *Liu and Shepherd*, 2008; *Das*, 2011; *Reid et al.*, 2014) analyze the temporal evolution of vertically integrated green line emissions, we present SCIAMACHY VERs as well. This gives a good opportunity to

verify the long-term radiometric stability of the SCIAMACHY Channel 3 data. The 10-year data record of SCIAMACHY VERs at 20°N–25°N is illustrated in Figure 5.16(b) and can be directly compared to the atomic oxygen data in Figure 5.16(a). Other latitudes can be found in Figure fig-4 in Appendix A.6.

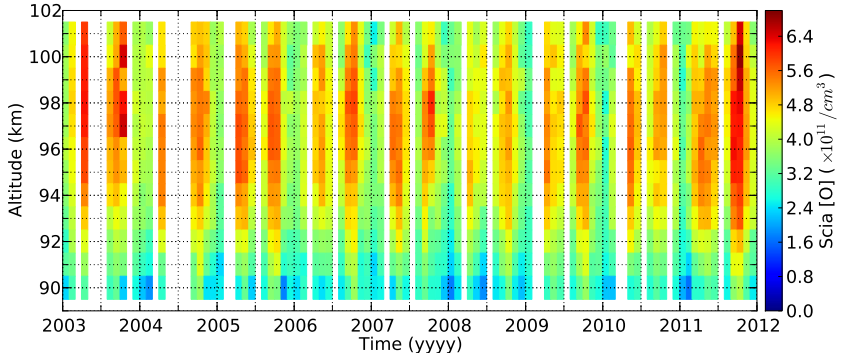

(a)

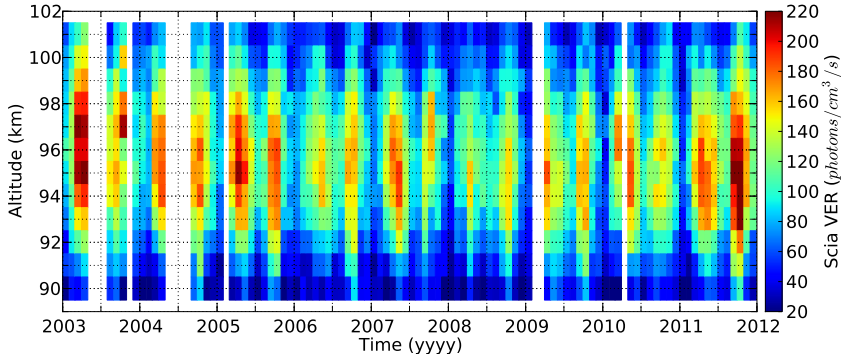

(b)

Figure 5.16: Temporal distribution of atomic oxygen abundances (a) and green line volume emission rates (b) from 2003 to 2011 at 20°N–25°N.

5.4.1 Harmonic analysis

The near ten-year data set of monthly vertical mean atomic oxygen abundances between 90 km and 103 km at 20°N–30°N is analyzed first as an example to introduce the analysis procedure. To quantify the short-term as well as long-term oscillations in the data, a Lomb-Scargle analysis (*Lomb*, 1976; *Scargle*, 1982) is performed to identify the dominant frequencies in the data (Figure 5.17). Strong signals are found at semi-annual and annual periods, while another four small peaks at 14, 16.5, 20 and 26 months are below the 99% confidence level and are not significant. The data at other latitudinal bands show similar periodograms.

The impact of the 11-year solar cycle is quite small in comparison to

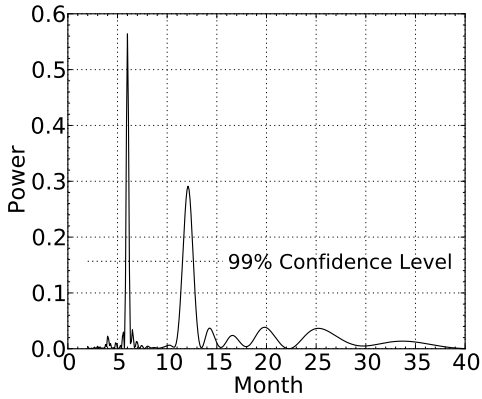

Figure 5.17: Lomb-Scargle periodogram of vertically integrated atomic oxygen abundance between 90 km and 103 km at 20°N–30°N over near ten years.

the SAO and AO oscillations, although the solar cycle variation is clearly visible in the data. To analyze the significant contributions quantitatively and to extract a potential solar influence, we perform a multi-linear regression analysis using the following equation:

$$\mathrm{y} = \mathrm{A}_{SAO} cos[\tfrac{2\pi}{6}(t - P_{SAO})] + A_{AO} cos[\tfrac{2\pi}{12}(t - P_{AO})] + A_{F107} F107(t - \mathrm{shift}) + \mathrm{offset} \tag{5.1}$$

where, F107 is the F10.7 cm solar flux proxy in units (SFU) of $10^{-22}\mathrm{Wm}^{-2}\mathrm{Hz}^{-1}$ (*Tapping*, 2013). A_{F107} is the amplitude of the F10.7 cm solar flux. A_{SAO}, A_{AO}, P_{SAO} and P_{AO} are the amplitudes and phases of the SAO and AO, respectively. The fitting parameters are the amplitudes and phases of the SAO and AO, supplemented by a factor (A_{F107}) scaling the F10.7 cm solar flux proxy and a constant term. The "shift" is the time lag of the solar cycle impact while the "offset" is the mean value of the time series. The uncertainty of the fitting parameters is estimated using a bootstrap analysis (*Efron*, 1979). Specifically, bootstrapping is applied to the fitting results y to create new datasets by adding the randomly resampled residuals of the measurements and the fitting results. Then, new fitting parameters can be calculated from the new datasets. Repeating this procedure several times gives a set of fitting parameters, whose standard deviation is taken as an estimate for the uncertainty of these quantities.

To illustrate the quality of the harmonic fit, we show the analysis of retrieved atomic oxygen concentrations at 20°N–30°N (Figure 5.18). The

fit captures all of the seasonal and long-term variations very well. SAO and AO dominate the seasonal variations. The SAO is found with maxima in April and October and with minima in June and January. Its amplitude is around 15%. The AO is also clearly visible, with maxima near the summer solstices and minima near the winter solstices and its amplitude

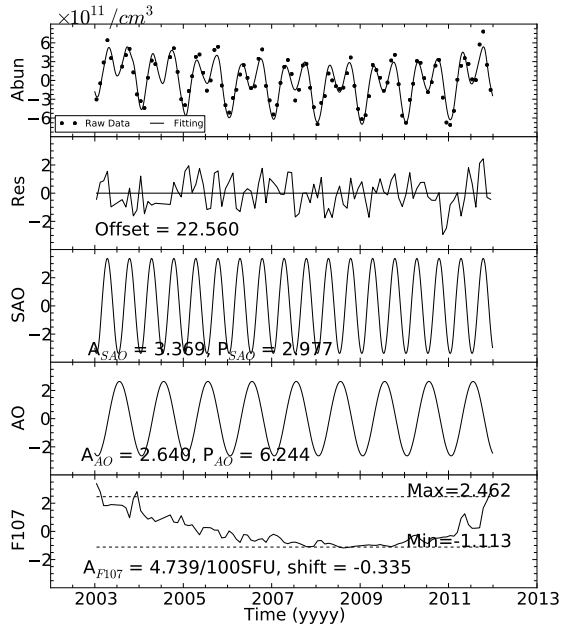

Figure 5.18: Harmonic analysis of column averaged atomic oxygen concentration ($\times 10^{11}/cm^3$) from 90 km to 103 km at 20°N–30°N for 2002–2012. The upper panels show the measured data minus the offset value given in the second panel and the multi-linear regression considering all the components. The second panel shows the fitted offset and the residual between the regression and the observations. The other panels show individual fitting components, as indicated in the axes labels.

is around 12%. Furthermore, it is found that the solar minimum (2009) to solar maximum variation (2003) is about 16% for this case and that the time lag between F10.7 cm flux and atomic oxygen is negligible (0.3 months).

The procedure stated above is also applied to analyse atomic oxygen abundances derived from SCIAMACHY O(^1S) green line measurements at other latitudes, as well as corresponding VERs. In general, the temporal evolution of the data shows annual and semi-annual oscillations with typical amplitudes of 5–15% for atomic oxygen and of 15–30% for VERs. Annual mean differences of atomic oxygen densities between the maximum (2002) and minimum (2008) of the 23rd solar cycle reveal variations of 5% at 90 km and 25% at 102 being in phase with the solar flux. The solar cycle variation will be discussed regarding to VERs and atomic oxygen abundances in detail below.

5.4.2 The impact of solar cycle on VERs

Several investigations of solar cycle impact have been performed by monitoring column O(^{1}S) nightglow emissions. *Takahashi et al.* (1984) found a correlation between green line emissions and the solar activity from six-year (1977–1982) nightglow measurements at 23°S. *Deutsch and Hernandez* (2003) found the green line emissions are in phase with solar activities based on ground-based long-term observations of six stations.

Clemesha et al. (2005) utilized the ratio of intensities of the green line emission and the O_2 (0, 1) band emission at 865 nm, observed by a multi-channel photometer at Cachoeira Paulista (23°S, 45°W) to investigate the solar cycle variation and found a 56% solar max./min. variation (a mean amplitude of 22%). *Liu and Shepherd* (2008) analyzed de-seasonalized integrated green line emissions measured by the WINDII instrument from 1991 to 1997 and found a linear correlation with F10.7 cm solar flux. *Das* (2011) investigated sixteen-year nighttime green line observations at Kiso (35.79°N, 137.63°E), Japan by ground-based photometers and found the solar max./min. variation of the solar cycle variation is around 44% (a mean amplitude of 18%), which is recalculated and confirmed by *Reid et al.* (2014) using a harmonic fit. A (41±11)% solar max./min. variation (a mean amplitude of (17±7)%) was found by *Reid et al.* (2014) when investigating over the 15-year period green line emission measurements by filter photometers at the Buckland Park Field Station (34.6°S, 138.6°E) near Adelaide, Australia. A latitude dependence is found between green line emission rate and the F10.7 cm solar flux and the correlation for mid latitudes is larger than for low latitudes (*Liu and Shepherd*, 2008), which is likely caused by the large-scale mesospheric circulation (*Liu and Shepherd*, 2008).

SCIAMACHY O(^{1}S) volume emission rates differ by 30-50% between 11-year solar max and min conditions (Figure 5.19). A pronounced latitudinal dependence of this difference is observed, which is most pro-

nounced in the equatorial region. WINDII observed even larger variations of O(^{1}S) VERs along the 22nd solar cycle (60% at 10°S–35°N) (*Liu and Shepherd*, 2008). In contrast to SCIAMACHY, WINDII did not observe these meridional variations in the solar cycle dependence. Instead, the relative variations of volume emission rates are almost constant for all latitudes. It should be noted that WINDII on UARS was flying in a precessing satellite orbit with changing local time over latitude, which makes the two measurements difficult to compare without the help of a tidal model.

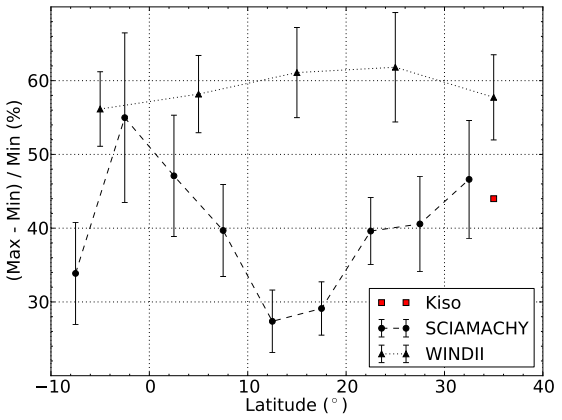

Figure 5.19: Solar cycle impact on vertical mean SCIAMACHY green line volume emission rate from 90 km to 102 km between 10°S and 35°N. The solar cycle effect derived from WINDII measurements is also included (*Liu and Shepherd*, 2008). Red square shows the solar max/min difference at Kiso station (35.79°N, 137.63°E). Error bars show the fitting parameter errors evaluated by the bootstrap analysis.

A local time dependence of the 11-year solar cycle in the green line radiance was indeed observed by ground based measurements at Kiso (35.79°N, 137.63°E) and the maximum dependency was found at around midnight (*Das*, 2011). Measurements of the WINDII and SCIAMACHY satellite instruments near 35°N observed the solar max/min differences of around 57% and 47%, respectively. It is found that the derived solar max/min difference from SCIAMACHY data at 35°N is comparable to the value (44%, red square in Figure 5.19) derived from the nearly coincident ground-based green line radiance measurements at Kiso (35.79°N, 137.63°E). An interesting result of the analysis in this work is that the influence of the 11-year solar cycle on SCIAMACHY green line emission rates increases with altitude (Figure 5.20): from 31% at 91 km to 58% at

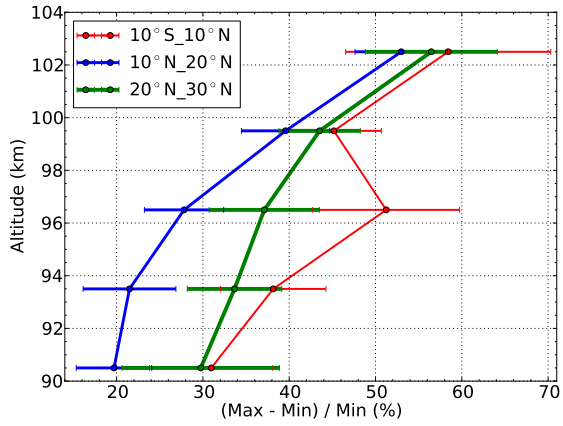

Figure 5.20: Solar cycle impact on SCIAMACHY green line volume emission rate at 5°S–5°N, 10°N–20°N and 25°N–35°N.

103 km for the equatorial latitudes; from 20% to 52% at 10°N-20°N; and from 30% to 56% at 25°N-35°N. The WINDII team did not publish vertically resolved O(^{1}S) data to compare with. The reason for this vertical increase will be discussed later.

5.4.3 The impact of solar cycle on atomic oxygen abundances

Retrieved atomic oxygen abundances will likely show a similar response to the 11-year solar cycle as the green line VERs, although the amplitude will likely differ. 11-year solar cycle max/min differences for vertical mean atomic oxygen concentrations (O^{scia}_{eton} and O^{scia}_{kho}) at 90–95 km are displayed in Figure 5.21. The altitude regime from 90 km to 95 km is chosen in order to compare to SCIAMACHY and SABER data derived from *OH* nightglow measurements in Chapter 7. The solar max/min differences vary by 5–15% for O^{scia}_{eton} and by 10–20% for O^{scia}_{kho} at 10°S–35°N. The solar cycle dependence of the retrieved atomic oxygen concentrations depends strongly on the latitude, which is most pronounced at 35°N.

For comparison, Figure 5.21 also shows the solar max/min differences of the averaged HAMMONIA atomic oxygen abundances at 22:00 LT between 90–95 km. The HAMMONIA run utilized in this work is a perpetual model run for constant solar max/min conditions typical for the years September, 1986 (solar minimum) and November, 1989 (solar maximum)

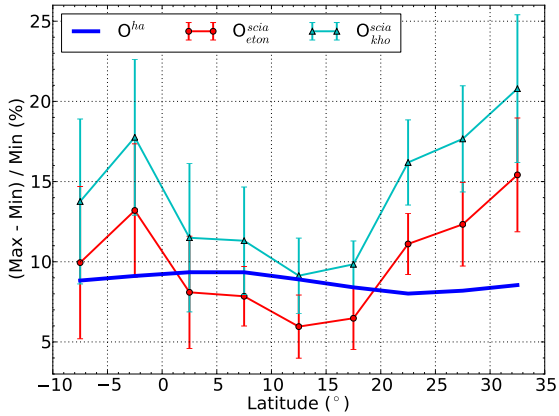

Figure 5.21: Solar cycle impact on vertical mean atomic oxygen concentrations from 90 km to 95 km between 10°S and 35°N. The impact on atomic oxygen derived from HAMMONIA (O^{ha}) is also included.

(*Schmidt et al.*, 2006). The solar minimum to solar maximum variation is around 9% between 10°S and 35°N, showing no pronounced latitudinal structure in the HAMMONIA atomic oxygen data set.

An altitude dependence of the solar cycle affect is observed in atomic oxygen density as well (Figure 5.22, for 0°-20°N). For O^{scia}_{eton}, the solar max/min difference increases from 9% at 90 km to 27% at 102 km. Larger solar max/min difference is derived from O^{scia}_{kho}, 18% at 90 km and 33% at 102 km. In general, the solar max/min difference increases by a factor of 2 to 3 from 90 km to 102 km.

Higher solar max/min differences are always obtained for the retrieved atomic oxygen if the Khomich model is used. One reason for this differ-

ence of the solar cycle response is the stronger temperature dependence of the Khomich model. SABER temperature depends on the solar flux at a rate of 4–6 K/100SFU between 50°S and 50°N ((*Forbes et al.*, 2014)). To investigate, in which way temperature changes affects the atomic oxygen solar cycle response, the retrieval was repeated considering a time-constant temperature profile (monthly zonal mean SABER data at (35° ± 5°)N, October, 2008) and altitudinal solar max/min differences were calculated (Figure 5.22). For retrieval results using the time-constant temperature profile, the derived solar cycle impact is around 2–6% weaker. It is also found that variations of the solar max/min difference due to applied background atmosphere for the Khomich model are larger than for the ETON model by a factor of 2.

Any trend or solar cycle dependence observed in species concentration versus geometric altitudes can either be caused by an expansion or shrinking of the entire atmosphere or by particular processes related to selected species, only. In this work, atomic oxygen abundance is analyzed on geometric altitudes. Most satellite payloads observing the mesosphere/lower thermosphere region (like SCIAMACHY) deliver their data on these coordinates, since they lack reliable pressure/temperature measurements to deliver their data on, e.g., pressure coordinates. For the same reason, derived species abundances can hardly be expressed as mixing ratios. To separate the solar cycle effect in the two, we repeat our solar cycle analysis for atomic oxygen mixing ratio (vmr) and total density separately

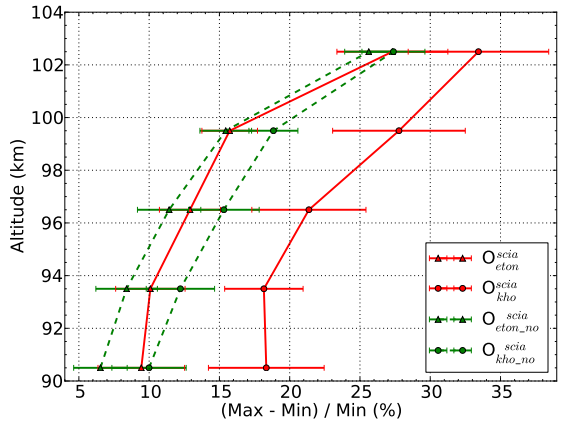

Figure 5.22: Solar cycle impact on retrieved atomic oxygen concentrations as function of altitude at 0°–20°N based on different photochemical models and background atmospheres. The dashed green lines show results from a retrieval utilizing a time-constant background atmosphere (for details see text). $O^{scia}_{eton\_no}$: the ETON model utilizing a constant background atmosphere; $O^{scia}_{kho\_no}$: the Khomich model utilizing constant background atmosphere.

based on the HAMMONIA data (Figure 5.23).

The breakdown of the solar max/min differences into volume mixing ratio (vmr, photochemistry) and total density (hydrostatics) reveal a similar picture in HAMMONIA. The atomic oxygen mixing ratio response to the 11-year solar cycle is nearly constant in altitude in the mesopause region (around 3–4% for HAMMONIA, Figure 5.23). The solar cycle has a far larger effect on total density: from 6% at 92 km to 11% at 102 km in HAMMONIA data. The differences were calculated at fixed geometric altitudes. This means, that the positive altitude gradient of the solar cycle

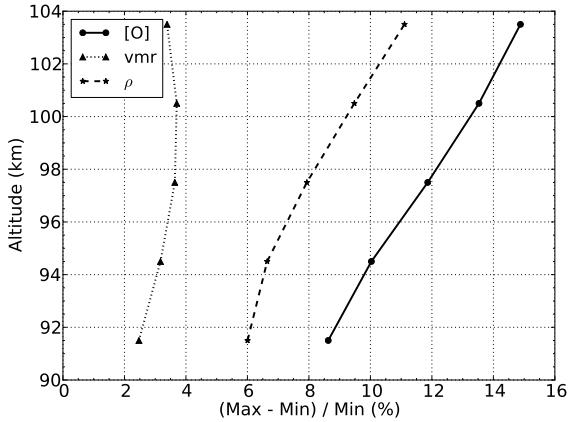

Figure 5.23: Altitudinal distribution of solar cycle impact on HAMMONIA atomic oxygen concentration ([O]), atomic oxygen mixing ratio (vmr) and total density (ρ) at 0°–20°N.

response of atomic oxygen abundance is likely caused by the expansion of the atmosphere and not by the photochemistry of atomic oxygen in the UMLT region. The expansion/shrinking of the atmosphere along the solar cycle is much more relevant for the atomic oxygen concentration (as measured on geometric altitudes) than variations of the solar UV flux.

Finally, it should be mentioned that the relative variations of atomic oxygen abundance along the 11-year solar cycle are based on data measured at 10 p.m. local solar time, and similar analyses based on data measured at other local times may differ for the following reason: atomic oxygen moves upwards and downwards during the day due to atmospheric tides, resulting in lower or higher values at one particular altitude. In gen-

eral, this variation cannot be expressed as a simple factor, which scales [O] at one particular local time with respect to [O] at another local time, independent of solar activity. Therefore, it cannot be expected that solar max/min ratios are independent of solar local time. This was confirmed by *Das* (2011), who found that the solar cycle impact on the green line emission rate is dependent on the local time, changing from 15% to 30% during the night and reaching its maximum at midnight.

Chapter 6

Atomic oxygen retrieved from SCIAMACHY OH airglow measurements

OH airglow emissions were observed in several channels by the SCIAMACHY instrument, as introduced in Chapter 1. Spectra arising from *OH*(9–6) band at 1377–1400 nm are utilized to derive atomic oxygen in the further analysis. This reduces the uncertainties introduced by the relaxation scheme significantly, as discussed in Chapter 3. Monthly zonal mean spectra in 5-degree latitude bin are used in order to allow for a comparison to atomic oxygen derived from SCIAMACHY $O(^1S)$ green line measurements in Chapter 5. To illustrate the data quality, *OH*(9–6) band spectra from one typical SCIAMACHY measurement profile are displayed in Figure 6.1. The maximum signal-to-noise ratio is up to 700 for this data.

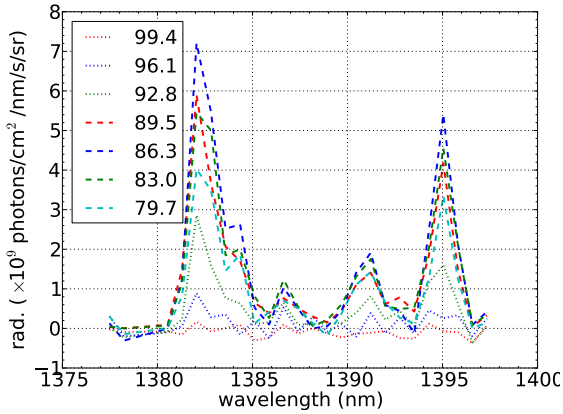

Figure 6.1: SCIAMACHY monthly zonal mean OH(9–6) band spectra for November 2005 at 35°N–40°N. The tangent altitudes for the spectra are shown in the legend in kilometres.

6.1 Atomic oxygen retrieval from OH(9–6) band measurements

6.1.1 Retrieval set up

The retrieval procedure to derive atomic oxygen abundance from OH radiances is set up in a similar way as for $O(^1S)$. The Gauss-Newton iteration algorithm was adopted to minimize a cost function involving the weighted deviations between the OH(9–6) band simulations and the real measurements by measurement noise covariances. The Tikhonov regularization was applied to the retrieval to stabilize the reconstruction process (*Tikhonov and Arsenin*, 1977). Since SCIAMACHY could not mea-

sure atmospheric parameters (O_2, O_3, N_2, temperature, and total density), the co-located SABER measurements (temperature, total density and O_3) were utilized. Only profiles measured between 9 p.m. and 11 p.m. were chosen here. The volume mixing ratios of O_2 and N_2 were set 0.21 and 0.78, respectively.

Proper physical parameters for the OH forward model have been discussed in Chapter 3 and a summary is listed as follows: For the collisional removal reaction of vibrationally excited OH^* with atomic oxygen a rate constant of $(6.465 \pm 0.785) \times 10^{-11} cm^3 s^{-1}$ derived by *Xu et al.* (2012) was applied; The rate constants for the quenching of OH^* by N_2 and O_2 used by *Mlynczak et al.* (2013b) were adopted and the nascent distribution (Table tab-2) derived by *Adler-Golden* (1997) was used here. The Einstein coefficients and line positions were derived from the HITRAN-2012 database (*Rothman et al.*, 2013). Other relevant rate constants were given in Table tab-4 in Appendix A.4.

6.1.2 Retrieval results and diagnostics

A retrieval is performed based on the typical SCIAMACHY OH(9–6) band measurements at 73–106 km and 35°N–40°N for November, 2005 (see Figure 6.1). Atomic oxygen abundances, radiative offsets, spectral peak position shift, and instrument line shape are the derivations. The latter two parameters are set to be constant with altitude. The radiative

offsets vary within $\pm 1.2 \times 10^8$ photons/cm^2/s/sr/nm and the spectral peak position shift is near zero (0.05 nm). The FWHM of the instrument line shape is approximately 1.3 nm.

Derived atomic oxygen abundances from the SCIAMACHY *OH*(9–6) band radiances are presented in Figure 6.2 at 80–96 km. The atomic oxygen abundance reaches up to approximately 7×10^{11}/cm^3 at 96 km. The statistical uncertainty due to the measurement noise is indicated by error bars. Large errors are found at altitudes above 95 km and below 83 km (see Figure 6.6), and relative errors reach up to 6% at 96 km, owing to the low signal to noise ratio of the measurements, and 16% at 80 km, due to the low *OH* emission signals at these altitudes.

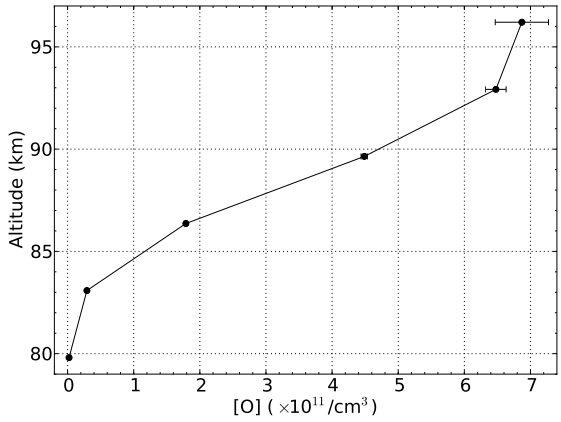

Figure 6.2: Zonal mean atomic oxygen abundance derived from SCIAMACHY *OH*(9–6) band measurements at 35°N–40°N for November, 2005. Error bars represent the statistical uncertainty due to the measurement noise.

The vertical profile of measured spectrally integrated OH(9–6) band radiances between 1380 nm and 1397 nm is displayed in Figure 6.3. The radiances reach up to 3.1×10^{10} photons/cm^2/s/sr at approximately 86 km. Error bars due to measurement noise are very small, indicating that the applied spectra have high signal to noise ratio. The corresponding OH(9–6) band simulations using the derived parameters are also shown in Figure 6.3 and are in good agreement with the measurements.

The averaging kernel and the vertical resolution for the retrieval are given in Figure 6.4. The retrieval results are significant between 80 and 96 km. At these altitudes, the measurement contribution (sum over each row of the averaging kernel) is about one and averaging kernels peak at

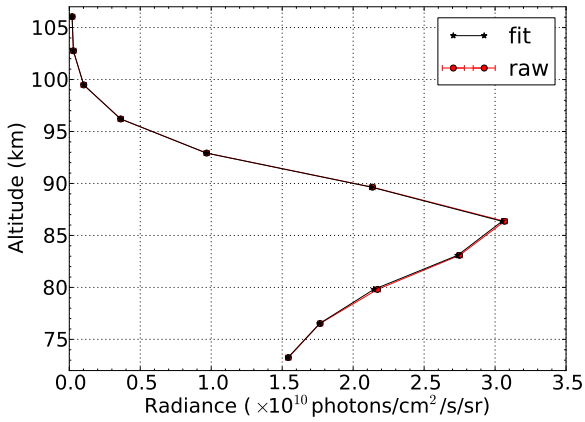

Figure 6.3: Measured and simulated integrated OH(9–6) band limb radiances between 1380 nm and 1397 nm at 35°N–40°N for November, 2005. Error bars represent the measurement noise.

the corresponding tangent altitudes (Figure 6.4(a)), which indicate that derived atomic oxygen abundances are real and not the a-priori. The FWHMs are around 3.3 km (Figure 6.4(b)), equalling to the sampling distance.

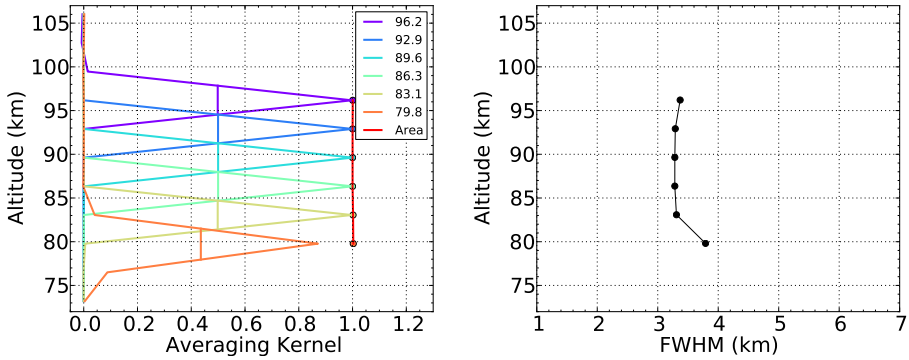

(a) Averaging kernel

(b) Vertical resolution

Figure 6.4: The averaging kernel and the vertical resolution of the retrieval. FWHM of each curve is given to indicate the vertical resolution of the retrieval. Degrees of freedom for signal are approximately 8.

6.1.3 Assessment of uncertainties

The relevant uncertainties in the forward model are related to parameters of production and loss processes of OH vibrational level 9. It is instructive to evaluate the uncertainty of the retrieved atomic oxygen resulting from these physical parameters. The uncertainties of k_{OO_2M} (rate constant for the three-body recombination of O, O_2 and background molecules), k_{HO_3}

(rate constant for the recombination of H and O_3) and k_{OO_3} (rate constant for the recombination of O and O_3) are approximately 19%, 17% and 53% (at 200 K, for details refer to Table tab-4), respectively. The uncertainty of k_{OHO} (rate constant for the collision of OH and O) is around 12%. No uncertainty is specified for the the 9th nascent distribution factor (f_9), rate constants regarding to $OH(v = 9)$ collisions with O_2 ($k_{O_2}(9)$), N_2 ($k_{N_2}(9)$), and Einstein coefficients (A). The used nascent distribution factor is approximately 6% larger than the one used by *Mlynczak et al.* (2013b) and the difference is applied as the factor uncertainty (see, Table tab-2). A perturbation of 10% is adopted for the unspecified $k_{O_2}(9)$, $k_{N_2}(9)$ and A.

Figure 6.5 shows the atomic oxygen derivation uncertainties associated with the various parameters as a function of altitude. The largest uncertainty source is k_{OO_2M} below 90 km, resulting in an uncertainty of 17% for derived atomic oxygen. Above this altitude, k_{OO_3} is the largest uncertainty source and the resulting uncertainty increases substantially from 10% at 90 km to 80% at 96 km. The uncertainty of f_9 and A map nearly linearly into the atomic oxygen uncertainty by around 6% and 10%, respectively. The resulting atomic oxygen uncertainty due to 10% $k_{O_2}(9)$ is around 5%. Other rate constants affect retrieved atomic oxygen abundance weakly (<2%). It is worth noting that the uncertainty of k_{HO_3} does not affect the atomic oxygen abundance because $k_{HO_3} \cdot [H] \cdot [O_3]$ is essentially what is measured by SCIAMACHY.

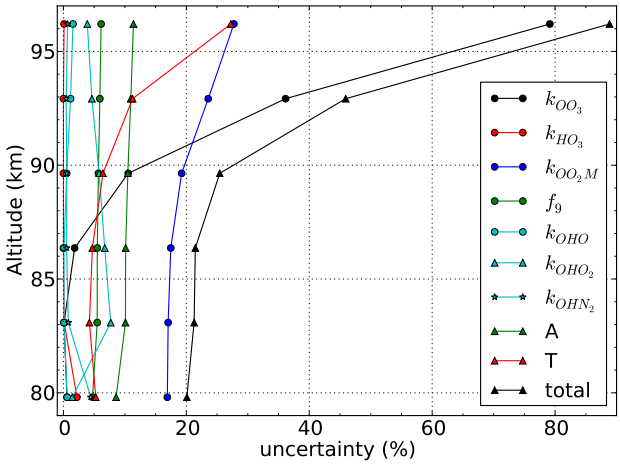

Figure 6.5: Percentage uncertainties of the retrieved atomic oxygen introduced by uncertainties of the forward model parameters and background atmosphere.

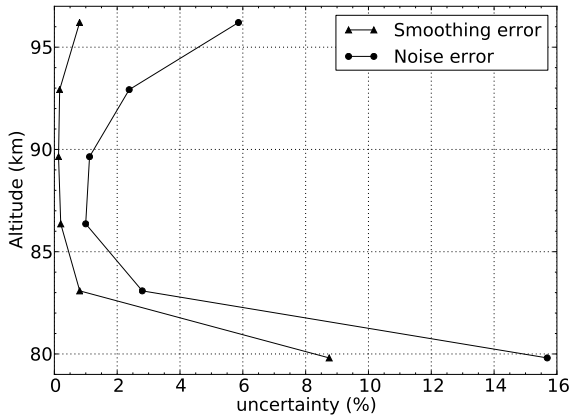

Figure 6.6: Percentage uncertainties of the smoothing error and the retrieval error.

The SABER temperature errors, 1.5 K ($\sim$ 1%) below 95 km and within 4–5 K ($\sim$ 3%) at 100 km, evaluated by *García-Comas et al.* (2008) are applied. The uncertainty of atomic oxygen increases from 5% below 90 km to 27% at 96 km due to the uncertainty of the SABER temperature. An overall resulting atomic oxygen uncertainty from these parameters is approximately 21% below 90 km, which rises up to 90% at 96 km. In addition, the smoothing error and the noise error are generally below 3% except for the upper and lower most altitudes (Figure 6.6). The noise errors are approximately 30–50% larger than the smoothing errors.

6.1.4 Retrieval scheme validation and comparison to SABER

For the inter-comparison of atomic oxygen retrieved here with other datasets, particular attention is paid to the validation of the forward model. SABER data gives a good opportunity to perform this test, because the radiance data, the retrieval model and the retrieval results are published (*Mlynczak et al.*, 2013b). The SABER channel A radiometric observations cover a spectral range of 1.9–2.2 μm, namely the 2.0 μm emission. This spectral range covers OH(9-7, 8-6) ro-vibrational bands. The unfiltered 2.0 μm emission rate is applied in the validation, which has been corrected from filtered data due to band pass and transparency of the filter.

It is set up the SCIAMACHY forward model in the same way as

Mlynczak et al. (2013b) set up the SABER forward model, except for the Einstein coefficients. Einstein coefficients based on HITRAN-2012 are used, which differ by about 7% from the values used by *Mlynczak et al.* (2013b). The differences are around 6% from the utilized values by *Mlynczak et al.* (2013b) according to the calculation of the SABER science team (*Mlynczak et al.*, 2013b) and it is consistent with the calculation in this work. A detailed discussion relevant to the effect of the usage of different Einstein coefficients is given in Appendix A.7. An important detail is that in the *OH* model of *Mlynczak et al.* (2013b) and in the reconstructed model the ozone loss owing to the reaction with atomic oxygen is omitted. That is,

$$k_{OO_2M} \cdot [O] \cdot [O_2] \cdot \rho \approx k_{HO_3} \cdot [H] \cdot [O_3] \tag{6.1}$$

A profile derived from the SABER database at 35°N–40°N for November, 2005 is applied to perform the reconstruction. The reconstructed SABER atomic oxygen data as well as published SABER data agree within 7% (Figure 6.7), as expected from the usage of different Einstein coefficients. This agreement can be considered as a validation of the SCIAMACHY *OH* retrieval scheme. In addition, a comparison is performed to atomic oxygen abundances derived from SCIAMACHY (Figure 6.2). Up to 30% deviation is found between the retrieved atomic oxygen from the SCIAMACHY and SABER data.

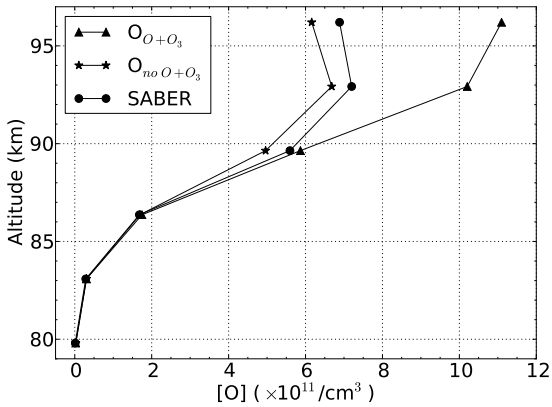

Figure 6.7: Nighttime atomic oxygen abundances derived from SABER *OH* 2.0 μm radiances at 35°N–40°N for November, 2005. The dotted line (SABER) shows the atomic oxygen derived from the SABER database. The triangle line (O_{O+O_3}) represents the reconstructed atomic oxygen profile considering the ozone loss due to collisions with atomic oxygen and the star line ($O_{no\ O+O_3}$) is the reconstructed atomic oxygen profile without considering this loss mechanism.

6.1.5 $O + O_3$ contribution to the retrieval

The reaction of ozone and atomic oxygen is another loss mechanism of ozone. This loss mechanism was not considered to derive atomic oxygen from SABER *OH* airglow measurements by *Mlynczak et al.* (2013b). It is straightforward to reconstruct SABER atomic oxygen data with our scheme by considering this mechanism. Up to 60% difference is caused by this loss mechanism (Figure 6.7). Smaller atomic oxygen concentrations are derived from *OH* airglow emissions if the loss of ozone by reac-

tion with atomic oxygen is neglected. SCIAMACHY OH airglow measurements offer another good opportunity to evaluate the contribution of the reaction $O + O_3$ to the retrieval results.

Neglecting the $O + O_3$ quenching is an important factor in the intercomparison of SABER data with SCIAMACHY atomic oxygen data. Therefore, its effect is analyzed for monthly zonal mean SCIAMACHY data at different latitudes (Figure 6.8). Up to 60% deviations are found for the two datasets at atomic oxygen abundance peak altitudes. Deviations

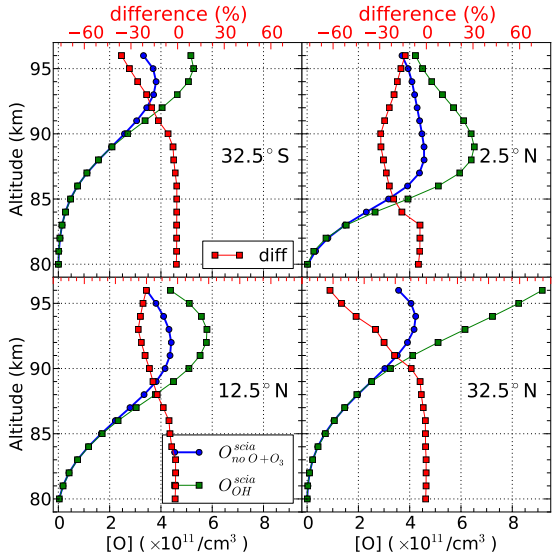

Figure 6.8: Atomic oxygen derived from monthly zonal mean SCIAMACHY OH airglow measurements with (O^{scia}_{OH}) and without ($O^{scia}_{no\ O+O_3}$) consideration of the reaction $O + O_3$ for April, 2005. Red square lines display percentage deviations of atomic oxygen abundances.

below 85 km is quite small. The atomic oxygen peak altitude is shifted by about 2 km to lower altitudes, if this loss process is neglected. Relative differences between the two retrieval runs are illustrated in Figure 6.9(b). The differences are 10–50% and the latitude-altitude differences show a pattern that is similar to the Hough modes describing the diurnal migrating tide. It indicates that differences of two type of derivations are mainly found in mid latitudes above 90 km and over equatorial region between 84 km and 93 km. This results from higher ozone loss by collisions with atomic oxygen due to high temperature (Figure 6.9(a)). The

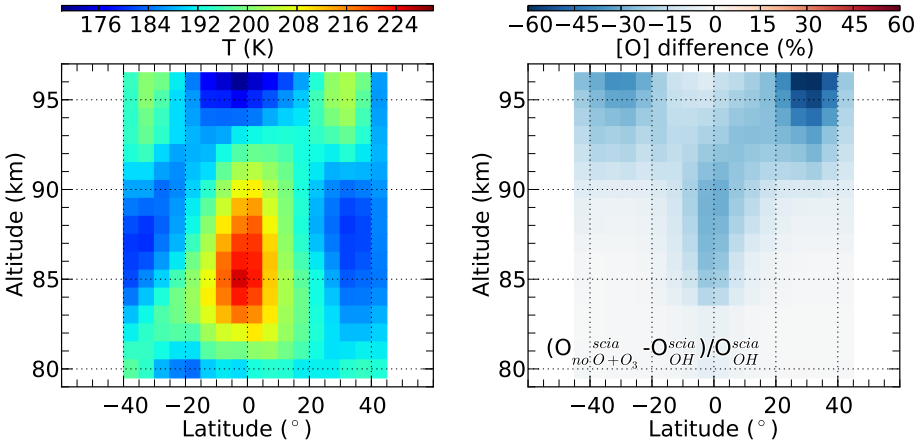

Figure 6.9: (a): Latitudinal temperature from SABER for April 2005. (b): Percentage differences of derived SCIAMACHY zonal mean atomic oxygen abundances based on two assumptions of ozone loss for April 2005.

deviations show a similar morphology as the temperature with local maxima at 95 km (206 K) in the mid latitudes and at 85 km (225 K) over the equatorial region. Abundance differences are very small below 84 km for the two atomic oxygen datasets. It is worth noting that the differences between SCIAMACHY and SABER atomic oxygen data are large (30%, Figure 6.2 and Figure 6.7), although they both rely on highly excited OH measurements. Considering forward model differences increases this difference even further. A more detailed assessment of differences between the two datasets is presented in Chapter 7.

6.2 Latitudinal and temporal variations

Global zonal mean atomic oxygen concentrations, as well as $OH(9-6)$ band volume emission rates, are derived from SCIAMACHY OH airglow measurements for the time period from 2003 to 2011. The latitudinal and temporal distributions of retrieved atomic oxygen abundances look similar to the data derived from $O(^1S)$ measurements (Figure fig-8, Figure fig-9 and Figure fig-10 in Appendix A.8).

The same analysis procedure utilized for the derived atomic oxygen from the green line measurements is adopted to investigate the individual variational components in the data. For OH(9–6) band volume emission rates at 80–95 km, SAO signals are found with a pronounced maxima ($\sim$24%) over the equatorial region. The signals decrease progressively in

southern and northern hemispheres towards the poles. This is also found in SABER *OH* nightglow measurements by *Gao et al.* (2010) with a maxima around 21% at 80–100 km over the equator region. AO signals are much weaker than the SAO signals. They show a weak maxima ($\sim$10%) over the equatorial region and a minima between 15°N and 20°N. For derived atomic oxygen abundances at 80–95 km, SAO amplitudes peak at 25% over the equatorial region and decrease towards the poles. AO amplitudes are less than 10% and have a maxima at around 10°N. AO signals in both datasets are 14% weaker than SAO signals. However, larger AO signals are found over the mid latitudes by the ground-based *OH* nightglow measurements (*Shefov*, 1969). One possible reason for weaker AO signals in the satellite measurements is that the satellite measurements are only conducted at one local solar time and may be not in the tidal phase with large tidal magnitude. In addition, a linear relationship is found between *OH* VER and atomic oxygen variations, which is consistent with an estimate made by *Shepherd et al.* (2006b).

Since near ten-year atomic oxygen abundances have been derived from SCIAMACHY *OH* nightglow measurements, it is straightforward to investigate the solar cycle variation imprinted in the atomic oxygen data. Figure 6.10(a) shows the solar maximum to minimum variation of the vertically mean atomic oxygen from 80 km to 95 km. The solar max/min differences are between 10% and 15% from 10°S to 20°N. The latitudinal structure is similar to what is found in the atomic oxygen derived

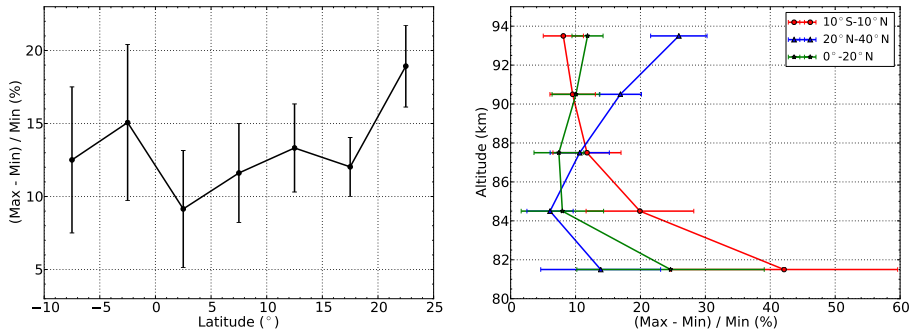

(a) (b)

Figure 6.10: Latitudinal distribution (a) and altitude dependence (b) of solar cycle variations of atomic oxygen concentrations derived from the SCIAMACHY *OH* nightglow measurements.

from SCIAMACHY green line measurements. A comparison to them at 90–95 km will be performed in Chapter 7, as well as the solar cycle effect derived from SABER atomic oxygen dataset for the same observational time span. Figure 6.10(b) displays solar max/min differences with altitude at several latitude bins (10°S–10°N, 0°–20°N and 20°N–40°N, respectively). The max/min differences decrease from 42% at 81 km to 8% at 93 km between 10°S and 10°N. At 0°–20°N, the max/min differences increase from 8% to 12% above 84 km. They are comparable to the differences found in the atomic oxygen derived from green line measurements based on the ETON model. The differences increase from 6% at 84 km to 26% at 93 km between 20°N and 40°N. It has been found that the atomic oxygen max/min variation is mainly driven by total density com-

pression/expansion variation during solar cycle in the investigation of the derived atomic oxygen from green line measurements.

Chapter 7

Intercomparison of various atomic oxygen datasets

SCIAMACHY measurements allow to derive the atomic oxygen abundance by means of two different atomic oxygen proxies, namely $O(^1S)$ (Chapter 5) and OH (Chapter 6) nightglow emissions. This allows to cross-check the results and verify the underlying photochemical models. Atomic oxygen measurements by SABER and WINDII instruments provide two additional datasets, which can be used for comparison.

The SABER atomic oxygen dataset was already introduced in the previous chapter. The data used here were derived from OH airglow measurements by the SABER 2.0 μm channel and averaged at 9–11 p.m. in 5-degree latitude bin. The SABER data used here covered the same period of time as the SCIAMACHY data. The WINDII instrument was aboard the UARS satellite and measured $O(^1S)$ and OH airglow emissions from late 1991 to 1997. The WINDII atomic oxygen data product is based on

OH(8-3) P_1(3.5) line measurements at lower altitudes and $O(^1S)$ green line measurements at higher altitudes (*Russell et al.*, 2005). Differences between WINDII and other instrument data (SCIAMACHY and SABER) are expected due to the different observational time span. The WINDII measurements are collected in such a way that only profiles measured at local solar time 9–11 p.m. are considered for this comparison. WINDII measurements are averaged monthly in 5-degree latitude bin after screening out SAA and aurora effects consistent with SCIAMACHY data.

In order to make a sophisticated comparison with the atomic oxygen, the retrieval has been repeated using WINDII and SCIAMACHY green line and OH nightglow measurements, based on the MSIS background atmosphere. Due to the lack of knowledge of $O(^1S)$ and OH forward model rate constants used by *Russell* (2003), the forward models and relevant rate constants are reset to what is used in this work, but a comparison of the original and reconstructed atomic oxygen abundances is made (see Figure 7.1). For the retrieval from WINDII $O(^1S)$ green line measurements, the ETON model is used and rate constants and Einstein coefficients are the same with what we used for the retrieval from SCIAMACHY green line measurements (Table tab-1). Following the retrieval approach of *Russell* (2003), chemical loss of ozone by reaction with atomic oxygen is neglected in the derivation of WINDII atomic oxygen data from OH(8-3) P_1(3.5) emission measurements and all the parameters needed are the same with what we utilized to derive atomic oxygen

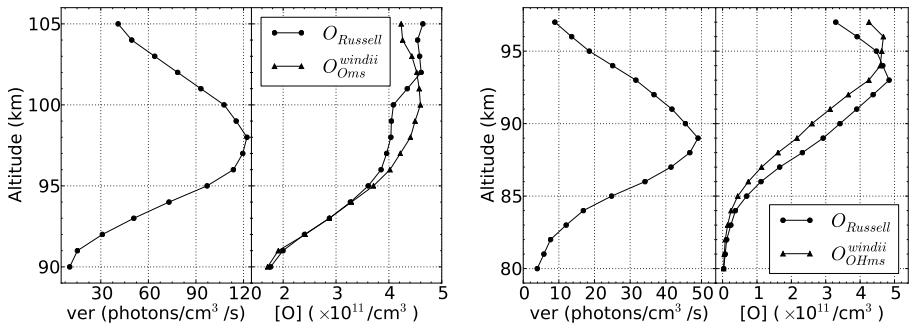

Figure 7.1: (a): Green line volume emission rates (left) and atomic oxygen abundances (right) calculated by *Russell* (2003) ($O_{Russell}$) and in this work (O_{Oms}^{windii}) at (47.6°E, 29.5°N) on 22:11:49 LT 03, Dec., 1991. (b): *OH*(8-3) P_1(3.5) volume emission rates (left) and atomic oxygen abundances (right) calculated by *Russell* (2003) ($O_{Russell}$) and in this work (O_{OHms}^{windii}) at (146.1°E, 29.0°N) on 22:39:32 LT 14, Nov., 1991. The background atmosphere is calculated by the MSIS (ms) model.

from SCIAMACHY *OH* nightglow measurements in Chapter 6.

To illustrate the differences of atomic oxygen abundances derived by *Russell* (2003) and the ones reconstructed in this work, green line (left panel, Figure 7.1(a)) and *OH*(8-3) P_1(3.5) line (left panel, Figure 7.1(b)) volume emission rates are derived from the WINDII database and the retrieval procedure is performed with the same retrieval setup stated above. Abundance differences derived from WINDII green line measurements are less than 12% (right panel, Figure 7.1(a)). Peak abundances derived from WINDII *OH*(8-3) P_1(3.5) measurements are similar but peak alti-

tude is shifted by 1 km, resulting up to 30% differences for the atomic oxygen out of peak altitude (right panel, Figure 7.1(b)). To some extent, the newly derived atomic oxygen abundances (O^{windii}_{Oms} and O^{windii}_{OHms}) from WINDII data in this work are comparable to derived by *Russell* (2003).

As stated in the chapter 5, the solar cycle effect plays a significant role in the variation of atomic oxygen abundances. Therefore, for comparison of the datasets under a similar solar flux condition, the WINDII measurements in 1993 and the SCIAMACHY measurements in 2004 are chosen here. The years 1993 and 2004 are both in the descending phase of solar cycle 22 and 23, respectively. The solar flux magnitude is comparable in these two years with a yearly average value at around 110 SFU. Atomic oxygen abundances derived from these datasets at 20°–35°N in September, 1993/2004 are given in Figure 7.2 to give an overview of the comparison. In-situ atomic oxygen abundances measured by rocket-borne mass spectrometers using the cryo-cooled, shock-freezing technique (*Trinks et al.*, 1978; *Offermann et al.*, 1981) are also displayed in the figure, which are thought the most accurate atomic oxygen measurements so far (*Hedin et al.*, 2009). These in-situ measurements were conducted in different local solar times at 37°–40°N and only dynamical processes contribute to variations of the atomic oxygen abundances due to their long lifetime. Therefore, it is still meaningful to compare them with derived atomic oxygen abundances in this work.

Atomic oxygen ($[O^{scia}_{eton}]$, $[O^{scia}_{Oms}]$ and $[O^{windii}_{Oms}]$, see the caption of Figure

7.2) derived from $O(^1S)$ green line measurements are comparable (< 7%) with abundances peaking at around $5.5 \times 10^{11}/cm^3$, especially for $[O^{scia}_{Oms}]$ and $[O^{windii}_{Oms}]$ though measured in different years (Figure 7.2). 18% difference is found between $[O^{scia}_{kho}]$ and $[O^{scia}_{eton}]$ at atomic oxygen peak altitude.

SABER atomic oxygen abundance ($[O^{saber}_{OH}]$) reaches up to $8.2 \times 10^{11}/cm^3$ and is 40% larger than the derived atomic oxygen ($[O^{scia}_{OH}]$) from SCIAMACHY *OH* nightglow measurements above 90 km, but around 30% smaller than the derivations at around 85 km in mid latitudes. It is worth noting that the SABER $[O^{saber}_{OH}]$ was calculated by *Mlynczak et al.* (2013b) without considering the ozone loss by collisions with atomic oxygen and a 30–50% larger atomic oxygen value would be derived from SABER *OH* nightglow measurements if considering this loss mechanism (see Figure 6.7). Atomic oxygen abundances ($[O^{windii}_{OHms}]$ and $[O^{scia}_{OHms}]$) derived from WINDII $OH(8-3)$ $P_1(3.5)$ emission measurements (1993) and SCIAMACHY $OH(9-6)$ band emission measurements (2004) using MSIS background atmosphere are also given. $[O^{scia}_{OHms}]$ is around 16% larger than $[O^{windii}_{OHms}]$ above 87 km but its abundance peak altitude is around 2 km lower.

Atomic oxygen abundances ($[O^{saber}_{OH}]$) are approximately 30% larger than the ones derived from $O(^1S)$ green line measurements. $[O^{scia}_{OH}]$ is around 10% smaller than the atomic oxygen abundance ($[O^{scia}_{eton}]$) derived from $O(^1S)$ green line measurements at peak altitudes. Peak altitude of

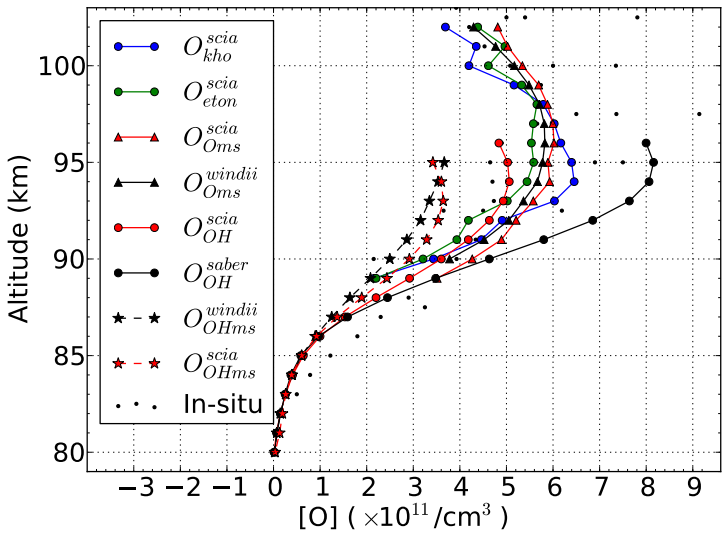

Figure 7.2: Atomic oxygen abundances at 20°–35°N in September, 1993/2004. O^{scia}_{kho} and O^{scia}_{eton}: atomic oxygen derived from SCIAMACHY $O(^1S)$ green line measurements based on Khomich and ETON models using SABER background atmosphere, respectively. O^{windii}_{Oms} and O^{scia}_{Oms}: atomic oxygen derived from WINDII in 1993 and SCIAMACHY $O(^1S)$ green line measurements in 2004 based on the ETON model using MSIS background atmosphere, respectively. O^{saber}_{OH}: atomic oxygen derived from SABER OH nightglow measurements. O^{scia}_{OH}: atomic oxygen derived from SCIAMACHY OH nightglow measurements using SABER background atmosphere. O^{windii}_{OHms} and O^{scia}_{OHms}: atomic oxygen derived from WINDII in 1993 and SCIAMACHY in 2004 OH nightglow measurements, respectively, using MSIS background atmosphere without considering ozone loss due to atomic oxygen. In-situ: atomic oxygen abundances measured by rocket-borne mass spectrometers (For details, please refer to the text).

atomic oxygen data derived from *OH* nightglow measurements is around 2 km lower than for the data derived from $O(^1S)$ green line measurements. Atomic oxygen abundances ($[O^{scia}_{eton}]$, $[O^{scia}_{kho}]$, and $[O^{scia}_{OH}]$) are comparable to in-situ measurements though differences also exist. Generally, a good agreement can be found between atomic oxygen abundances derived from SCIAMACHY $O(^1S)$ green line and *OH* nightglow measurements. In the following subsections the differences between the various datasets presented in Figure 7.2 are illustrated in a more comprehensive way.

7.1 Intercomparison of atomic oxygen datasets based on $O(^1S)$ and *OH* nightglow observations from the same instrument

Atomic oxygen datasets derived from SCIAMACHY $O(^1S)$ ($[O^{scia}_{eton}]$ and $[O^{scia}_{kho}]$) and *OH*(9–6) ($[O^{scia}_{OH}]$) nightglow observations can be used to verify the instrument characterization and consistency, because $O(^1S)$ and *OH*(9–6) emissions were observed by the SCIAMACHY channel 3 and channel 6, respectively. The other reason is to validate the underlying forward models, which are based on different photochemical processes - at least for most part.

The spatial distribution in these atomic oxygen datasets is similar (see Figures 5.14 and fig-8), although some features, such as the tidal struc-

tures, are more pronounced in the green line data. These differences are likely caused by the temperature dependence of rate coefficients, which might not be accurately given (if at all) in the rate constants. Figure 7.3 shows latitudinal deviations of derived atomic oxygen datasets at 89–95 km in 2009. It is found that $[O_{OH}^{scia}]$ is roughly up to 20% larger than $[O_{eton}^{scia}]$ between 30°S and 30°N (Figure 7.3(Top)). At latitudes poleward of 45°N, up to 60% differences are found between $[O_{OH}^{scia}]$ and $[O_{eton}^{scia}]$ at around 92–95 km. Large $[O_{eton}^{scia}]$ (up to 30% larger) is also found in April at 30°S at around 95 km. This is caused by the lower peak altitudes of $[O_{OH}^{scia}]$ than for $[O_{eton}^{scia}]$ and $[O_{kho}^{scia}]$ in mid latitudes, as shown in Figure 7.2. Similar phenomena are also found in deviations of $[O_{OH}^{scia}]$ and $[O_{kho}^{scia}]$ (Figure 7.3(Bottom)), but deviations, up to 50% at around 95 km in mid latitudes, are even larger than for $[O_{OH}^{scia}]$ and $[O_{eton}^{scia}]$.

A correlation diagram is a common mean to visualize and quantify the interdependency of the two datasets. Figure 7.4 displays scatter plots of different datasets derived from SCIAMACHY green line measurements (ETON model: $[O_{eton}^{scia}]$; Khomich model: $[O_{kho}^{scia}]$) and OH measurements ($[O_{OH}^{scia}]$) between 50°S and 50°N at 89–95 km in 2009. A linear fit is performed to give a rough estimate of the consistency between different data sets. The consistency between $[O_{eton}^{scia}]$ and $[O_{OH}^{scia}]$ is better than for $[O_{kho}^{scia}]$ and $[O_{OH}^{scia}]$, which can be verified by the fitting slopes (see Figure 7.4(a) and Figure 7.4(b)). $[O_{kho}^{scia}]$ is smaller for small atomic oxygen abundances (up to 4.0×10^{11}/cm^3), but is larger for larger values in com-

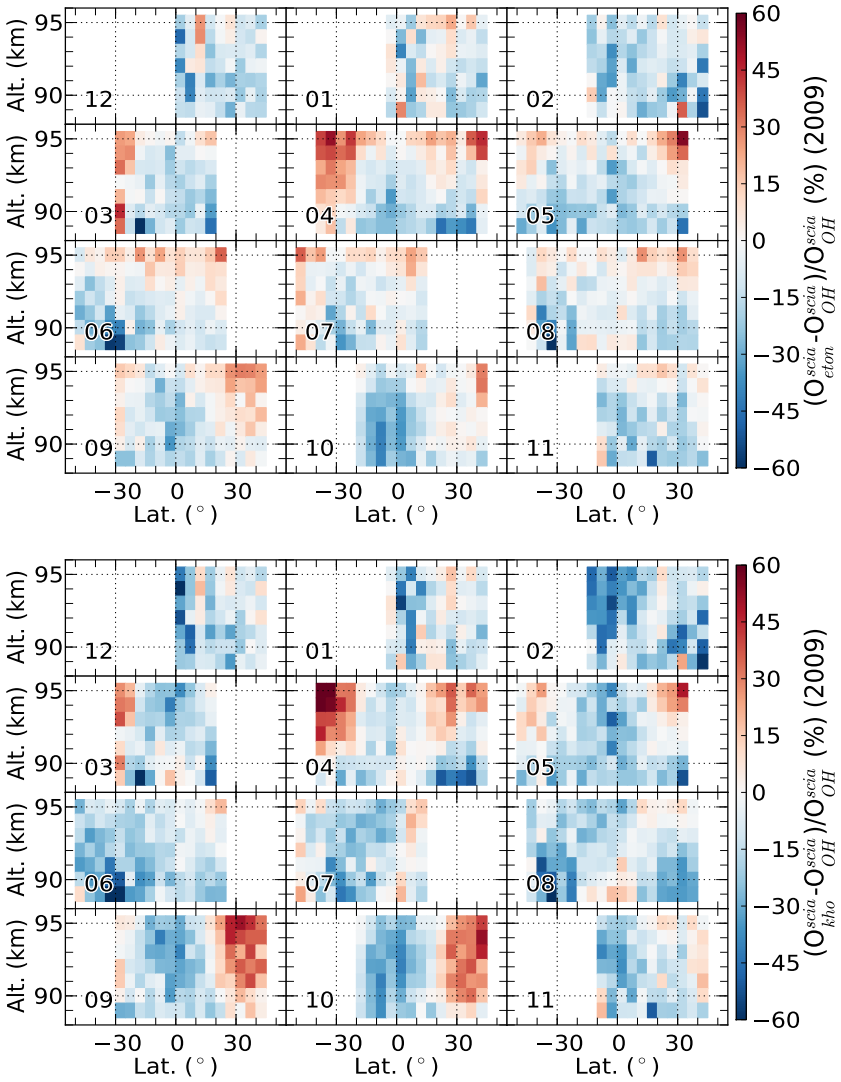

Figure 7.3: Differences between different atomic oxygen datasets at 89–95 km in 2009. Top: deviations between atomic oxygen derived from SCIAMACHY *OH* nightglow measurements ($[O^{scia}_{OH}]$) and $O(^1S)$ nightglow measurements based on the ETON model ($[O^{scia}_{eton}]$); Bottom: deviations between $[O^{scia}_{OH}]$ and atomic oxygen derived from $O(^1S)$ nightglow measurements based on the Khomich model ($[O^{scia}_{kho}]$).

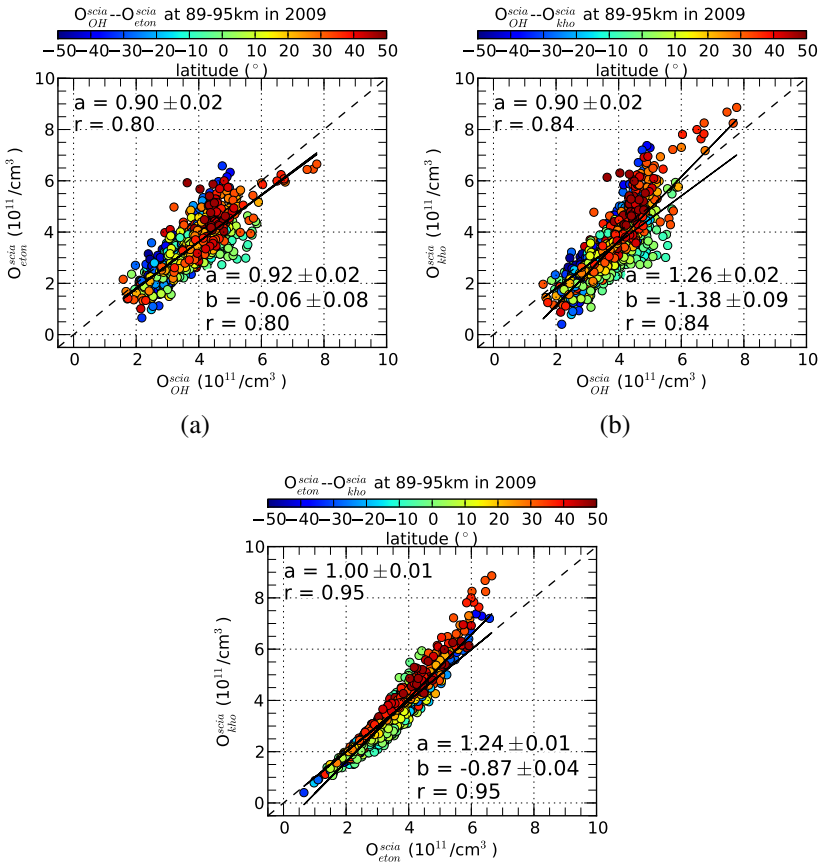

Figure 7.4: Scatter plots of derived atomic oxygen from SCIAMACHY $O(^1S)$ green line (ETON model: $[O^{scia}_{eton}]$; Khomich model: $[O^{scia}_{kho}]$) and OH ($[O^{scia}_{OH}]$) nightglow measurements between 50°S and 50°N at 89–95 km in 2009. The color bar shows the latitudes. The dashed line shows the bisector (slope=1). The solid lines show linear fits to the data. One only fits one parameter (a in upper left corner) and another fits two parameters (a and b in lower right corner). a and b represent the slope and y-intercept of the fitting line, respectively. r represents the correlation coefficient of the fitting. (a): scatter plot of $[O^{scia}_{OH}]$ and $[O^{scia}_{eton}]$; (b): scatter plot of $[O^{scia}_{OH}]$ and $[O^{scia}_{kho}]$; (c): scatter plot of $[O^{scia}_{eton}]$ and $[O^{scia}_{kho}]$.

parison to $[O_{OH}^{scia}]$. A similar phenomenon is also found between $[O_{eton}^{scia}]$ and $[O_{kho}^{scia}]$ (Figure 7.4(c)), which is caused by the extremely small abundances at equator and large values at mid latitudes for $[O_{kho}^{scia}]$ (see Figure 5.14).

Deviations and scatter plots between these datasets for other years are also investigated as the year 2009 and a similar morphology can be found in these datasets. In general, the analysis of $[O_{eton}^{scia}]$ gives a consistent picture with $[O_{OH}^{scia}]$. $[O_{kho}^{scia}]$ is approximately 30% smaller than $[O_{OH}^{scia}]$ at low latitudes, but up to 50% larger at latitudes poleward of 30°S and 30°N.

7.2 Intercomparison of atomic oxygen abundances derived from SABER and SCIAMACHY measurements

OH nightglow measurements have been conducted by the SABER instrument in the same period as the SCIAMACHY instrument. It affords a good opportunity to make a comprehensive comparison. The preliminary result shows that $[O_{OH}^{saber}]$ is around 30% larger than $[O_{OH}^{scia}]$.

Zonal mean differences between SCIAMACHY ($[O_{OH}^{scia}]$) and SABER ($[O_{OH}^{saber}]$) atomic oxygen abundances derived from *OH* nightglow measurements are illustrated in Figure 7.5 for 2009. The most striking fea-

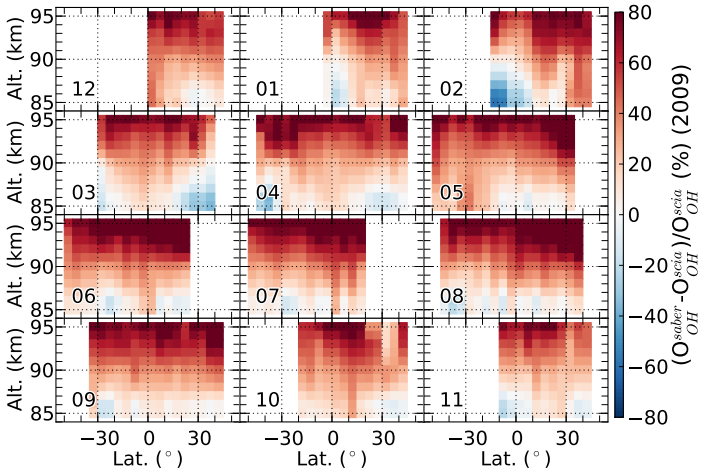

Figure 7.5: Monthly mean zonal mean deviations of $[O_{OH}^{scia}]$ and $[O_{OH}^{saber}]$ in 2009. The color bar shows the percentage deviation.

ture in these plots is the increasing difference of the two datasets with increasing altitude. Below 90 km, the two datasets agree within ±20%, but above 90 km, $[O_{OH}^{saber}]$ becomes much larger than $[O_{OH}^{scia}]$ and the deviation reaches up to around 80% in latitudes poleward of 40°N and 40°S. Another key point is that $[O_{OH}^{saber}]$ is derived from SABER *OH* nightglow measurements without considering the ozone loss by collisions with atomic oxygen (*Mlynczak et al.*, 2013b). If this process would be considered in the SABER retrieval, the derived $[O_{OH}^{saber}]$ will increase by another 20–50%, as we found in the chapter 6.

Figure 7.6 shows a scatter plot of derived atomic oxygen from SCIAMACHY and SABER *OH* nightglow measurements in 2009 at 85–95

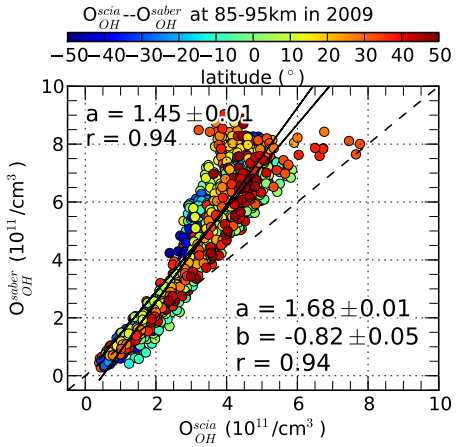

Figure 7.6: Scatter plot of atomic oxygen derived from SCIAMACHY and SABER *OH* nightglow measurements in 2009 at 85–95 km. The color bar indicates the latitude. The dashed line shows the bisector (slope=1). The solid lines show linear fits to the data. One only fits one parameter (a in upper left corner) and another fits two parameters (a and b in lower right corner). a and b represent the slope and y-intercept of the fitting line, respectively. r represents the correlation coefficient of the fitting.

km. Two datasets agree quite well for small atomic oxygen abundances (up to about 3.5×10^{11}/cm^3)), but differ by 50% on average for larger values. $[O^{saber}_{OH}]$ is much larger than $[O^{scia}_{OH}]$ at around atomic oxygen peak altitudes.

Smith et al. (2010) found that $[O^{saber}_{OH}]$ is 2–5 times larger than atomic oxygen abundances calculated by reference models (*Llewellyn and McDade*, 1996; *Picone et al.*, 2002) and abundances derived from WINDII measurements (*Russell et al.*, 2005). A comparison to the $[O^{saber}_{OH}]$ and

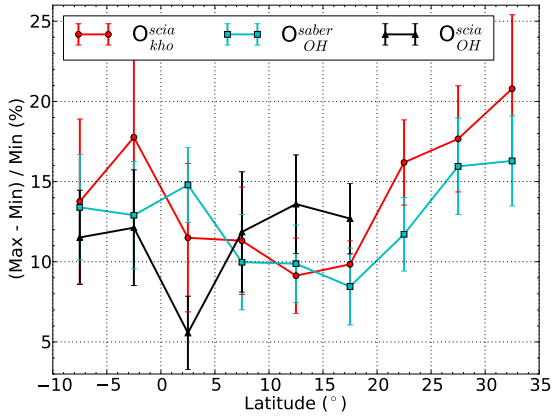

Figure 7.7: Latitudinal distribution of solar cycle variations of atomic oxygen abundances of SABER ($[O_{OH}^{saber}]$) and SCIAMACHY ($[O_{OH}^{scia}]$ and $[O_{kho}^{scia}]$).

$[O_{OH}^{scia}]$ has also been performed from the year 2005 to 2011. Similar phenomena are found from their deviations like in 2009 and a factor up to 2 is found here for $[O_{OH}^{saber}]$ compared to $[O_{OH}^{scia}]$. It turns out that a large atomic oxygen concentration can be derived from SABER *OH* nightglow measurements.

The time series of SABER data exhibits similar patterns as the SCIAMACHY data (Appendix A.9). Solar max/min differences imprinted in SABER data (Figure 7.7) vary in a range between 8% and 16% from 10°S to 35°N at 90–95 km. For comparison, solar max/min differences derived from SCIAMACHY data ($[O_{OH}^{scia}]$ and $[O_{kho}^{scia}]$) are also displayed. These derived max/min differences are comparable. Solar max/min differences

derived from $[O_{kho}^{scia}]$ and $[O_{OH}^{saber}]$ show a consistent picture in the latitudinal structure.

7.3 Intercomparison of atomic oxygen abundances derived from WINDII and SCIAMACHY measurements

Atomic oxygen abundances have been derived from WINDII $O(^1S)$ green line measurements ($[O_{Oms}^{windii}]$) and $OH(8-3)\ P_1(3.5)$ nightglow measurements ($[O_{OHms}^{windii}]$) using the MSIS background atmosphere in the work. It is straightforward to compare them to the SCIAMACHY data ($[O_{Oms}^{scia}]$ and $[O_{OHms}^{scia}]$) to assess the characterization of the measurements, though the measurements are conducted in different solar cycles. For comparison to the datasets under a similar solar flux condition, the WINDII data in 1993 and the SCIAMACHY data in 2004 are chosen here.

Latitudinal deviations of atomic oxygen abundances derived from WINDII measurements in 1993 and SCIAMACHY measurements in 2004 are shown in Figure 7.8. Deviations of 20% are found between $[O_{Oms}^{scia}]$ and $[O_{Oms}^{windii}]$ and reach up to 40% in some latitudes (Figure 7.3(Top)). The quantities derived from WINDII measurements are mostly larger than for SCIAMACHY measurements below 96 km, but smaller above this altitude. $[O_{OHms}^{scia}]$ and $[O_{OHms}^{windii}]$ agree fairly well between 87

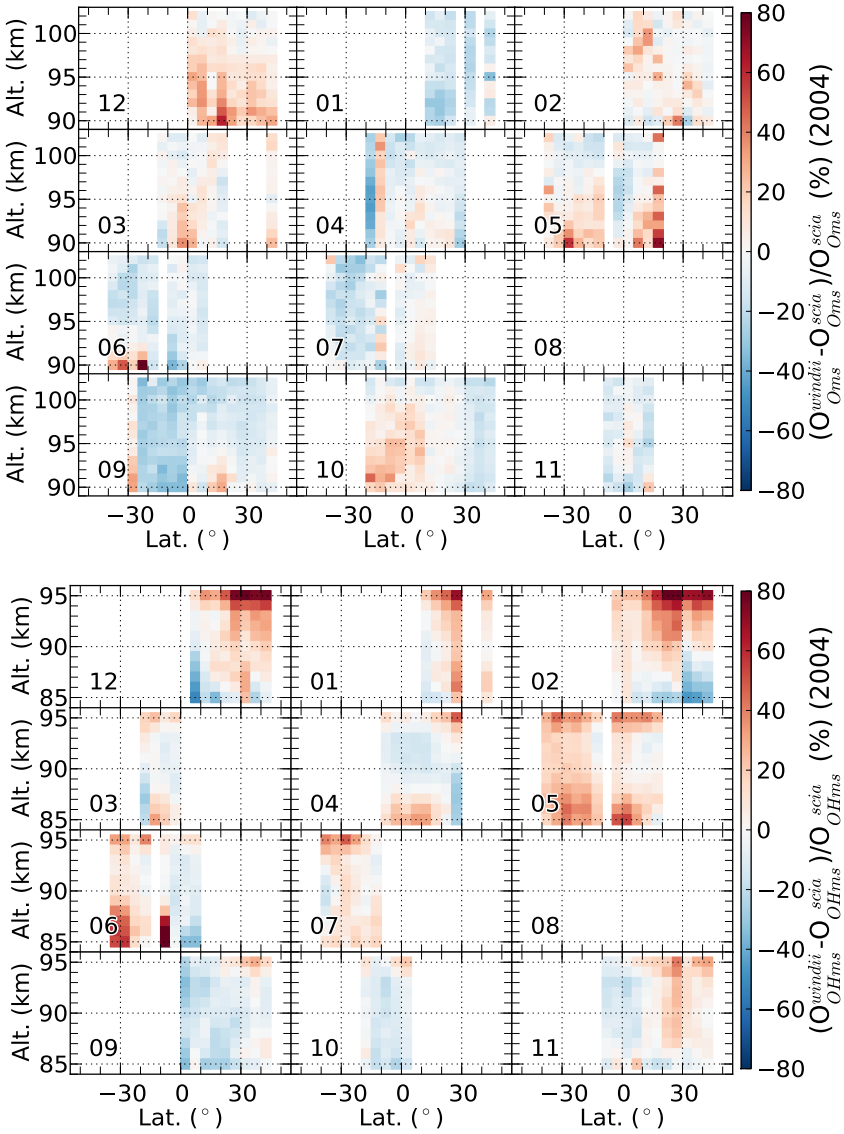

Figure 7.8: Latitudinal deviations of atomic oxygen derived from $O(^1S)$ green line measurements (Top) at 90–102 km and from *OH* nightglow measurements (Bottom) at 85–95 km measured by WINDII in 1993 and SCIAMACHY in Nov. 2004. The color bar shows the percentage deviations.

km and 93 km but large deviations (up to 80%) are found at around 85 km and 95 km, especially in solstice seasons (Figure 7.3(Top)). Dynamic factors may be responsible to the large deviations, as expected, due to the different observational time periods. A better agreement is found in fall and deviations are less than 20%.

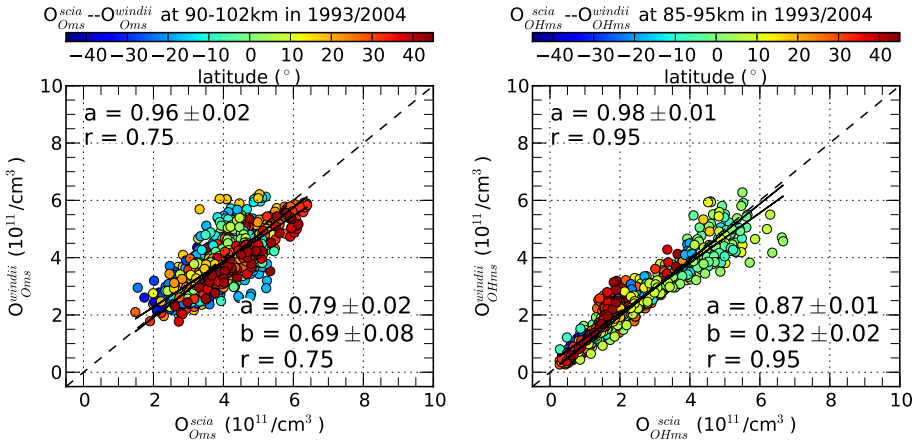

Figure 7.9: Scatter plots of data derived from WINDII measurements in 1993 and SCIAMACHY measurements in 2004 between 45°S and 45°N. The color bar indicates the latitude. The dashed line shows the bisector (slope=1). The solid lines show linear fits to the data. One only fits one parameter (a in upper left corner) and another fits two parameters (a and b in lower right corner). The parameters a and b represent the slope and y-intercept of the fitting line, respectively. The parameter r represents the correlation coefficient of the fitting. (a): scatter plot of derived atomic oxygen from WINDII and SCIAMACHY $O(^1S)$ green line measurements at 90–102 km; (b): scatter plot of derived atomic oxygen from WINDII and SCIAMACHY *OH* nightglow measurements at 85–95 km.

Scatter plots of atomic oxygen abundances derived from WINDII and SCIAMACHY $O(^1S)$ green line and OH nightglow measurements are displayed in Figure 7.9. Atomic oxygen abundances derived from $O(^1S)$ green line measurements have a good agreement with each other, shown in Figure 7.9(a). Large atomic oxygen values are preferably derived from SCIAMACHY measurements at higher latitudes and from WINDII measurements at lower latitudes. The linear fitting slope (0.96) indicates that these two datasets are consistent with each other in some extent. Atomic oxygen concentrations derived from OH nightglow measurements are shown in Figure 7.9(b). A better agreement is found than for atomic oxygen abundances derived from $O(^1S)$ green line measurements, because both slopes of the two applied fitting strategies are close to 1 and the correlation coefficient is 0.95. In general, the quantities derived from these measurements show quite a good agreement with each other, though the measurements by WINDII and SCIAMACHY were conducted in the different solar cycles.

Chapter 8

Conclusions

The main objective of this work is the derivation and analysis of the atomic oxygen abundance in the mesopause region based on SCIAMACHY airglow measurements. The dataset nearly covers the entire Envisat operational phase from 2003 to 2011. The OH and $O(^1S)$ airglow emission measurements were used here, which gave information about atomic oxygen in different, but overlapping altitude regions.

Two forward models have been applied to simulate SCIAMACHY green line and OH nightglow limb measurements, respectively. To simulate the $O(^1S)$ green line emission rates, two photochemical models, namely ETON and Khomich, were used, which are different in simplifications and used rate constants. The resulting atomic oxygen profiles extend from about 90 to 105 km. Number densities at the atomic oxygen peak altitude were typically 4–7$\times 10^{11}$/cm^3. Atomic oxygen uncertainties arising from the uncertainties in the $O(^1\mathrm{S})$ forward model parame-

ters were typically 14% for the ETON model and 17% for the Khomich model. Differences arising from the different model schemes were typically less than 20% and derivations based on the ETON model provided larger abundances above atomic oxygen peak altitude. The other method to obtain atomic oxygen abundances is the use of vibrationally excited OH^*. The OH^* forward model is comparatively straightforward. Resulting atomic oxygen profiles extend from 80 to 96 km. *OH* forward model parameter uncertainties induced an error of 20% at 80 km and 90% at 96 km for derived atomic oxygen abundances.

Comparison to different atomic oxygen datasets was performed and a relatively good agreement was found between derived atomic oxygen from SCIAMACHY green line and *OH* nightglow measurements, especially for the atomic oxygen derived from SCIAMACHY green line measurements based on the ETON model and the one derived from SCIAMACHY *OH* nightglow measurements. The comparison to the WINDII and SABER atomic oxygen showed that the derived atomic oxygen from SCIAMACHY measurements is comparable to the WINDII atomic oxygen in the whole altitude regime but about 30–50% smaller than the atomic oxygen derived from SABER *OH* nightglow measurements above 87 km.

The latitudinal, seasonal and long-term variations of the nightglow emissions and derived atomic oxygen were discussed, with a particular focus on the solar cycle variation. The solar max/min differences im-

printed in atomic oxygen abundances varied in a range of 8–18% and depended on the latitude. It is somewhat striking that the solar cycle variation increases with altitude and is primarily driven by total density compression/expansion variations during the solar cycle, rather than different photolysis rates. This is caused by the fact that atomic oxygen number densities were retrieved in this work, which reflect total density changes as well as atomic oxygen volume mixing ratio (vmr) variations. HAMMONIA model data indicated that the former is more dominant (8–15% at 90–104 km) and atomic oxygen vmr changes vary between solar max and min conditions by only 3%.

8.1 Outlook

The simultaneous observation of $O(^1S)$ and OH nightglow emissions by SCIAMACHY and WINDII gives a unique opportunity to constrain the underlying photochemical models in such a way that the differences between the two methods are minimized. SCIAMACHY with its multitude of OH observations will allow to add further OH observations (e.g. OH(8-5) band measurements) to this analysis, which makes the work more robust regarding instrumental effects such as radiometric calibration or stray light contamination. Applying the same methods and algorithms to WINDII measurements will further support this kind of analysis. Another interesting field of future work is to utilize the hyperspec-

tral observations of SCIAMACHY to constrain the relaxation scheme of OH^*. This topic is not that important for the retrieval of atomic oxygen as conducted in this work, but it will increase the quality of atomic oxygen inversions based on broadband emission measurements, such as SABER. In addition, it would be very desirable, if a few key rate constants could be measured at higher accuracy in the laboratory, such as k_{OOM} $(O + O + M \longrightarrow O_2^* + M)$, k_{OO_3} $(O + O_3 \longrightarrow O_2 + O_2)$, k_{OO_2M} $(O + O_2 + M \longrightarrow O_3 + M)$ and $k_{O_2^*O}$ $(O_2^* + O \longrightarrow O_2 + O(^1S))$.

To obtain a good signal to noise ratio, the observations used in this work were zonally and monthly averaged. For the price of a larger noise level, longitudinally or daily resolved data could be processed as well, in particular for the OH data, which exhibits a better signal to noise (S/N) ratio than the $O(^1S)$ data. Longitudinal data will allow to investigate dynamical processes, such as non-migrating tides, and daily data will allow to analyze short-term solar variabilities in the mesopause region. Further more, single profile retrieval is possible for the SCIAMACHY OH measurements.

Several other daytime atomic oxygen datasets, such as SABER data (*Smith et al.*, 2011b), are available, which are typically based on the photochemical equilibrium of O_3 and O and are the most consistent ones in terms of observations and methods. Owing to the long lifetime of atomic oxygen, these datasets can be used to predict nighttime atomic oxygen abundances for inter-comparison in combination with a tidal model,

which will give a further evidence of atomic oxygen data. Unfortunately, atomic oxygen retrieval based on green line emission data are restricted to altitudes below about 106 km (depending on the actual S/N of the measurement). Combining NO observations in the ultraviolet and infrared regions would allow to extend the atomic oxygen altitude range significantly.

Appendix A

Appendix

A.1 Rate constants of $O(^1S)$ forward model

All the rate constants used in the $O(^1S)$ green line emission model are listed in Table tab-1. The rate constant k_{OOM} corresponds to four temperature dependences recommended by different investigators in the table and a detailed discussion is introduced below.

The absolute values of k_{OOM} at low temperature ($\sim$200 K) are still poorly determined (*Pejaković et al.*, 2008). Experimental measurements of k_{OOM} have been just conducted in the recent years (*Pejaković et al.*, 2008; *Smith and Robertson*, 2008) after a more than 30-year old measurement conducted by *Campbell and Gray* (1973). The temperature dependence of k_{OOM} is in debate. Four temperature dependent expressions for the rate constant k_{OOM} are available nowadays (see Table tab-1) (*McDade et al.*, 1986; *Baulch et al.*, 1976; *Roble*, 1995; *Smith and Robertson*, 2008). A summary of these previous measurements and temperature dependences for the rate constant of atomic oxygen recombination

in nitrogen is displayed in Figure fig-1.

Values of rate constant k_{OOM} at 171–327 K have been measured from 1960 to 2008 and most measurements were conducted at room temperature (298 K) (*Morgan et al.*, 1960; *Barth*, 1961; *Morgan and Schiff*, 1963; *Campbell and Thrush*, 1967; *Campbell and Gray*, 1973; *Pejaković et al.*, 2008; *Smith and Robertson*, 2008). Measurements at two lower temperatures than 250 K have been only performed by *Campbell and Thrush* (1967); *Campbell and Gray* (1973); *Smith and Robertson* (2008). Temperature dependences of k_{OOM} were recommended by several investigators (*McDade et al.*, 1986; *Baulch et al.*, 1976;

Table tab-1: Reaction rate constants for the $O(^1S)$ photochemical models

Rate Constant	Value	Reference
A_{5577}	$(1.260 \pm 0.095)(\mathrm{s}^{-1})$	*Nicolaides et al.* (1969)
$A_{O_{1S}}$	$(1.394 \pm 0.105)(\mathrm{s}^{-1})$	*Slanger et al.* (2011)
$A_{O_2^*}$	$3.0(\mathrm{s}^{-1})$	*Khomich et al.* (2008)
k_{OOM}	$4.7 \times 10^{-33} \times (\frac{300}{T})^2 (cm^6 s^{-1})$	*McDade et al.* (1986)
	$2.76 \times 10^{-34} \times exp(\frac{720}{T})(cm^6 s^{-1})$	*Baulch et al.* (1976)
	$9.59 \times 10^{-34} \times exp(\frac{480}{T})(cm^6 s^{-1})$	*Roble* (1995)
	$3.0 \times 10^{-33} \times (\frac{300}{T})^{3.25} (cm^6 s^{-1})$	*Smith and Robertson* (2008)
$k'_{O_2^* O}$	$1.0 \times 10^{-12} (cm^3 s^{-1})$	*Khomich et al.* (2008)
$k_{O_{1S}O}$	$(5.0 \pm 0.533) \times 10^{-11} \times exp(\frac{-305}{T})(cm^3 s^{-1})$	*Slanger* (1976)
$k_{O_{1S}O_2}$	$(2.32 \pm 0.94) \times 10^{-12} \times exp(\frac{-812+1.82\times10^{-3}T^2}{T})(cm^3 s^{-1})$	*Capetanakis et al.* (1993)
$k_{O_{1S}N_2}$	$5.0 \times 10^{-17} (cm^3 s^{-1})$	*Gobbi et al.* (1992)
$k_{O_2^* O}$	$5.9 \times 10^{-12} (cm^3 s^{-1})$	*Khomich et al.* (2008)
$k_{O_2^* O_2}$	$3.0 \times 10^{-14} (cm^3 s^{-1})$	*Khomich et al.* (2008)
$k_{O_2^* N_2}$	$4.7 \times 10^{-9} \times (\frac{200}{T})^2 exp(\frac{-1506}{T})(cm^3 s^{-1})$	*Bates* (1988b)
C_1	211 ± 10	*McDade et al.* (1986)
C_2	15 ± 2	*McDade et al.* (1986)

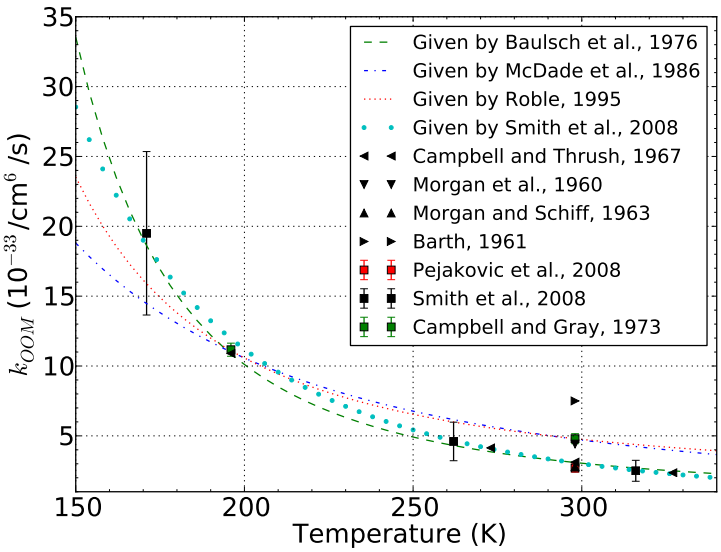

Figure fig-1: Laboratory measurements and temperature dependences for the rate constant of the reaction $O + O + N_2 \rightarrow O_2^* + N_2$.

Roble, 1995; *Smith and Robertson*, 2008) based on these measurements but different fitting strategies (the Arrhenius form and the power law expression). Latest measurements are more consistent with results calculated by the temperature dependence recommended by *Baulch et al.* (1976). However, uncertainty at 171 K measured by *Smith and Robertson* (2008) is quite large (30%).

In the research community relevant to the UMLT region, temperature dependence recommended by *McDade et al.* (1986) has been used by several investigators (*Russell*, 2003; *Gao et al.*, 2012; *Lednyts'kyy et al.*, 2015) and the ETON model was also developed based on the dependence. In the UMLT region, temperature varies in a range at 170–240 K (*Xu et al.*, 2007) and the largest

difference between temperature dependences recommended by *McDade et al.* (1986) and *Baulch et al.* (1976) is around 30%. Since the ETON model is used to derive atomic oxygen abundances, the temperature dependence recommended by *McDade et al.* (1986) is adopted in the work. A 30% uncertainty is assumed for k_{OOM} in order to describe differences within these temperature dependences.

A.2 *OH* nascent production rates

Several measurements have been conducted to determinate the nascent production rates (*Charters et al.*, 1971; *Ohoyama et al.*, 1985; *Klenerman and Smith*, 1987). *Steinfeld et al.* (1987) utilized a linear surprisal analysis to extrapolate the nascent distribution derived by *Charters et al.* (1971) to lower vibrational states. *Adler-Golden* (1997) renormalized the extrapolated nascent distribution by utilizing the Einstein coefficients which were derived by *Nelson et al.* (1990). *Adler-Golden* (1997) found the renormalized distribution agrees fairly well with the one derived by *Klenerman and Smith* (1987) and is comparable with the one measured by *Ohoyama et al.* (1985). All the available nascent distributions are listed in Table tab-2.

Mlynczak and Solomon (1993) supposed that a portion of the exothermic energy of the reaction R3.1 converts to heat directly and the rest excites hydroxyl radicals internally. They took an average of the nascent distributions derived by *Charters et al.* (1971), *Ohoyama et al.* (1985), and *Klenerman and Smith* (1987), and 91% of the available chemical energy can be accounted.

Kaufmann et al. (2008) adopted this population distribution in analysing chemical heating rates derived from SCIAMACHY *OH* airglow. *Mlynczak et al.* (2013b) derived atomic oxygen from SABER *OH* channel 2.0 μm airglow emissions, utilizing the nascent distribution recalculated by *Klenerman and Smith* (1987) in combination with Einstein coefficients of *Mies* (1974).

Table tab-2: Nascent distributions of excited hydroxyl radicals by the reaction R3.1

v	f_v*	$f_v\star$	$f_v\dagger$	$f_v\dagger\dagger$	$f_v\ddagger$	f_v**	$f_v\star\star$
1	0	0	0	0	0	0	0
2	0	0	0	0	0	0	0
3	0	0	0	0	0	0	0
4	0	0	0	0	0	0	0
5	0	0	0	0	0	0	0.01
6	< 0.154	0.066 ± 0.033	0.082 ± 0.021	0.107	0.10	$\approx$0.04	0.03
7	≈ 0.154	0.295 ± 0.066	0.169 ± 0.013	0.147	0.21	0.17	0.15
8	0.308	0.311 ± 0.033	0.266 ± 0.013	0.302	0.29	0.35	0.34
9	0.385	0.328	0.483	0.444	0.40	0.43	0.47

$*$: *Charters et al.* (1971) (OH chemiluminescence measurment: *Charters et al.* (1971), Einstein coefficients: different values were chosen by *Charters et al.* (1971))

$\star$: *Ohoyama et al.* (1985) (OH chemiluminescence measurement: *Ohoyama et al.* (1985), Einstein coefficients: *Mies* (1974)).

†: *Klenerman and Smith* (1987) (OH chemiluminescence measurement: *Klenerman and Smith* (1987), Einstein coefficients: *Mies* (1974)).

††: *Klenerman and Smith* (1987) (OH chemiluminescence measurement: *Charters et al.* (1971), Einstein coefficients: *Mies* (1974)).

‡: *Mlynczak and Solomon* (1993). For details, please refer to the text.

$**$: *Steinfeld et al.* (1987) (OH chemiluminescence measurement: *Charters et al.* (1971), Einstein coefficients: *Nelson et al.* (1990)).

$\star\star$: *Adler-Golden* (1997) (OH chemiluminescence measurement: *Charters et al.* (1971), Einstein coefficients: *Nelson et al.* (1990)).

A.3 *OH* Einstein coefficients

Several Einstein coefficient databases have been released (*Mies*, 1974; *Langhoff et al.*, 1986; *Turnbull and Lowe*, 1989; *Goldman et al.*, 1998; *van der Loo and Groenenboom*, 2007; *Rothman et al.*, 2013). These Einstein coefficients are shortly represented as Mies, LWR, TL, Gold, Trans, and HITRAN, respectively, for convenient. These databases mainly differ in the utilization of the dipole moment function (*Cosby and Slanger*, 2007). Einstein coefficients calculated by *Mies* (1974), *Langhoff et al.* (1986), *Turnbull and Lowe* (1989) and *Goldman et al.* (1998) have their own defects, owing to either flawed experimental data utilized or flawed spectroscopic constants used, which has been reported by *Colin et al.* (2002) and *Cosby and Slanger* (2007). For this four databases, Einstein coefficients calculated by *Goldman et al.* (1998) was found to be preferred by evaluation of the column densities derived from calibrated emission intensities and the corresponding Einstein coefficients (*Cosby and Slanger*, 2007). Einstein coefficients calculated by *van der Loo and Groenenboom* (2007) and *Rothman et al.* (2013) (namely HITRAN) are the newest two databases and it is still undecided which one is better.

The HITRAN hydroxyl emission line intensities are generated by drawing upon the calculation of *Goldman et al.* (1998) and its line positions are calculated based on the spectroscopic constants and term values for the $OH(X^2\Pi_i)$ state updated by *Bernath and Colin* (2009) (*Rothman et al.*, 2005, 2009). *van der Loo and Groenenboom* (2007) computed the Einstein coefficients based on a high-level ab initio function in combination with a spectroscopically parametrized lambda-type doubling Hamiltonian and found that the experimental dipole mo-

ment and potential energy curve could be successfully predicted by their simulations.

In order to evaluate these two Einstein coefficient databases, the same method and observed emission intensities utilized by *Cosby and Slanger* (2007) are adopted to calculate column densities of each rovibrational state:

$$N(v,j) = \frac{I^{(v,j)}_{(v',j')}}{A^{(v,j)}_{(v',j')}} \tag{A.1}$$

where, $N(v,j)$ is the column density at (v,j) rovibrational state, $I^{(v,j)}_{(v',j')}$ is the measured column line intensity and $A^{(v,j)}_{(v',j')}$ is the Einstein coefficient for the quantum transition from rovibrational state (v,j) to (v',j'). The observed line positions and intensities are given in Table tab-3, as well as corresponding Einstein coefficients derived from these two databases. For comparison, Einstein coefficients of Mies, LWR and TL are also given in the table. The HITRAN values are around 40% larger than for the Trans. Deviations between the HITRAN and the TL are found within 20%. The Mies and LWR values are much smaller than for other three values. The column densities for these rovibrational states are calculated from the measured line intensities based on the HITRAN and Trans Einstein coefficients as what *Cosby and Slanger* (2007) did to evaluate the reliability of Einstein coefficients. If the derived column densities are consistent with each other for each vibrational state, it indicates that the Einstein coefficients are relatively accurate. The column densities are normalized to the value of the longest wavelength for each vibrational state and given in Figure fig-2. It is found that both of them are not self-consistent to 1 but the yield values from the Trans Einstein

Table tab-3: *OH* $P_1(2.5)$ line positions, intensities and corresponding Einstein coefficients derived from different databases.

$v' - v''$	wavelength (nm)	UVES (Rayleigh)[a]	Mies[b]	LWR[c]	TL[d]	HITRAN[e]	Trans[f]
9–3	628.74	8.3			0.302	0.260	0.146
9–4	779.41	68.9	0.610	0.508	1.987	2.042	1.146
9–5	1008.24	452	5.411	3.563	9.889	11.598	7.234
8–2	591.53	4.7			0.112	0.092	0.052
8–3	731.62	51.5	0.298	0.225	0.984	0.946	0.546
8–4	943.96	395	2.834	2.063	6.274	7.140	4.268
6–0	529.85	0.3			0.005	0.004	0.002
6–1	678.79	9.9	0.028	0.030	0.134	0.114	0.066
6–2	839.91	154	0.644	0.483	1.719	1.790	1.068

[a]: line intensities measured by the UV-visual echelle spectrograph (UVES) on the Kueyen telescope in Paranal, Chile (*Hanuschik*, 2003).
[b]: Einstein coefficients from *Mies* (1974).
[c]: Einstein coefficients from *Langhoff et al.* (1986).
[d]: Einstein coefficients from *Turnbull and Lowe* (1989).
[e]: Einstein coefficients from *Rothman et al.* (2013).
[f]: Einstein coefficients from *van der Loo and Groenenboom* (2007).

coefficients are more close to 1. That is, the self-consistency of the Trans Einstein coefficients is a little better than for the HITRAN. *Noll et al.* (2015) utilized these two Einstein coefficients to derive rotational temperatures and *OH* populations at rovibrational states from simultaneous spectroscopic measurements by a medium-resolution X-shooter echelle spectrograph operated by the European Southern Observatory (ESO) at Cerro Paranal in Chile and found that the HITRAN Einstein coefficients are more reliable than for the Trans. In addition, the accuracy of the absolute Einstein coefficient values is still in debate and the simulated *OH* band emissions could be subject to systematic error when utilizing these Einstein coefficients. Therefore, HITRAN is used in this work and, additionally, Trans is only used for comparison.

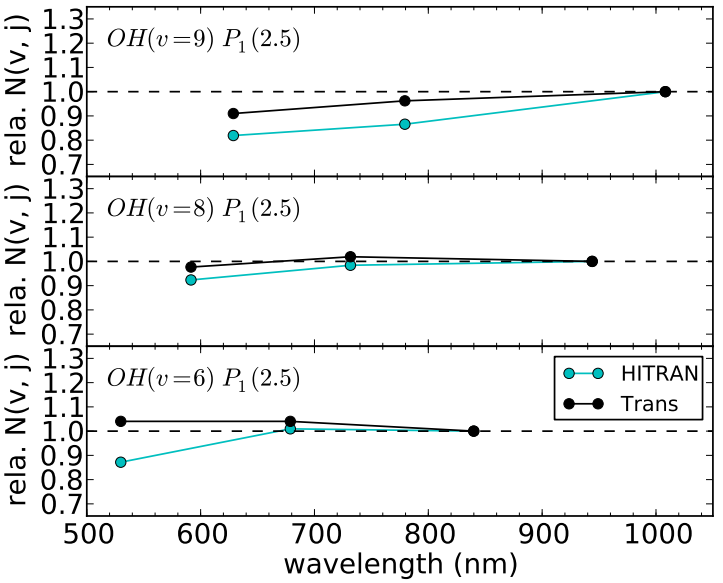

Figure fig-2: Relative column densities for *OH* $P_1(2.5)$ lines at vibrational states 9, 8 and 6. Column densities are normalized to the density of the longest wavelength for each vibrational state. Einstein coefficients derived from HITRAN and Trans are adopted.

A.4 *OH* relaxation models

It is still controversy regarding to the *OH* relaxation schemes (the sudden-death model, the single-quantum model and the multi-quantum model) by a collision with N_2, O_2 or O. *McDade and Llewellyn* (1987) investigated the sudden-death relaxation model and the single-quantum relaxation model using ground-based OH airglow measurements but did not identify the preferred model. *McDade* (1991) found that the night OH airglow emissions was well explained by a relaxation scheme involving the sudden-death quenching model when reproducing peak altitude distributions of different vibrational hydroxyl emissions. *Makhlouf et al.* (1995) adopted the single-quantum relaxation model to develop a photochemical-dynamical model for the OH airglow and investigated gravity wave propagating effect on OH airglow emissions. *Makhlouf et al.* (1995) collected different vibrational rate constants for the quenching of $OH(v)$ by O_2 from *Dodd et al.* (1990) ($1 \leq v \leq 6$), *Knutsen and Copeland* (1993) ($7 \leq v \leq 8$), and *Chalamala and Copeland* (1993) ($v = 9$) and logarithmically extrapolated vibrational rate constants for the quenching of $OH(v)$ by N_2 utilizing the interpolation based on the rate constants at $v = 2$ (*Rensberger et al.*, 1989) and $v = 12$ (*Sappey and Copeland*, 1990). The extrapolated rates by *Makhlouf et al.* (1995) are collected in Table tab-5. *Adler-Golden* (1997) constructed a combination kinetic model based on the laboratory measurements to study Meinel bands emissions. His conclusion supported that the single-quantum relaxation scheme for the OH^* quenching by N_2 and for the quenching of OH^* by O_2 at low vibrational levels. In addition, multi-quantum quenching scheme is recommended for the quenching of OH^* by O_2 at high vibrational levels. For the efficient quencher O_2, *Adler-*

Golden (1997) utilized a more sophisticated expression to present rate constants considering exponential vibrational number gap scaling.

$$k_{O_2,(v,v')} = C[P_v]^{v-v'} \; 0 \leq v' < v \tag{A.2}$$

where, C is a constant to scale the entire system of rate constants. P_v is the probability factor for the vibrational state v (Table tab-6). $C = 4.4 \times 10^{-12}$ $\mathrm{cm^3 mole^{-1} s^{-1}}$ is adopted by *Adler-Golden* (1997). A corrected value $C = (3.181 \pm 0.669) \times 10^{-12}$ $\mathrm{cm^3 mole^{-1} s^{-1}}$ was derived from SABER *OH* airglow measurements by *Xu et al.* (2012) using a correction factor when investigating hydroxyl emission mechanisms. The derived total removal rates by *Xu et al.* (2012) for all the vibrational states are fairly in agreement with the laboratory measurements and are given in Table tab-6. *Russell* (2003) retrieved atomic oxygen from $O(^1S)$ green line measurements and OH (8-3) band $P_1(2.5)$ line measurements by WINDII instrument onboard the UARS satellite. He found that the retrieved atomic oxygen from these two emissions agrees fairly well when the sudden-death relaxation model is utilized. *Kaufmann et al.* (2008) compared SCIAMACHY channel 6 *OH* airglow measurements and model simulations (based on the sudden-death relaxation model, the single-quantum model, and a mixture of these two models) and found a better agreement between them if the mixture of the sudden-death relaxation model and the single-quantum model are adopted. *Smith et al.* (2010) utilized the 2.0 μm emissions observed by SABER instrument to retrieve atomic oxygen concentrations by assuming the single-quantum relaxation model for the quenching by O_2 and N_2 and the sudden-death relaxation model for the quenching by O. *Xu et al.* (2012) repro-

duced SABER 1.6 and 2.0 μm emissions to compare SABER realistic measurements and found that a large discrepancy between measurements and simulations appears if the sudden-death relaxation model for the quenching by by O_2 and N_2 is applied. *von Savigny et al.* (2012) found a qualitative and quantitative agreement for peak altitude distributions of different vibrational levels between SCIAMACHY measurements and model simulations when the multi-quantum relaxation model for the quenching by O_2 is utilized. However, a mixture of these three relaxation models is a preference (*Adler-Golden*, 1997; *Kaufmann et al.*, 2008; *von Savigny et al.*, 2012), that is, the sudden death model is used for the quenching of OH by O, the single-quantum model is applied for the quenching of OH by an inefficient quencher N_2, and the multi-quantum model is adopted for the quenching of OH by a more efficient quencher O_2.

Table tab-4: Hydroxyl chemistry rate constants. $f(298)$ represents rate constant uncertainty factor at 298 K and g represents the uncertainty factor in exponent.

Rate constants	Reaction rate	f(298)$*$	g$*$	Reference
k_{OO_2M}	$6.0\times10^{-34}(\frac{300}{T})^{2.4}cm^6s^{-1}$	1.10	50	*Sander et al.* (2011)
k_{HO_3}	$1.4\times10^{-10}exp(\frac{-470}{T})cm^3s^{-1}$	1.10	40	*Sander et al.* (2011)
k_{OO_3}	$8.0\times10^{-12}exp(\frac{-2060}{T})cm^3s^{-1}$	1.10	200	*Sander et al.* (2011)
$k_{O,(v,v')}$	$2.0\times10^{-10}cm^3s^{-1}$	-	-	*Adler-Golden* (1997)
	$5.0\times10^{-11}cm^3s^{-1}$	-	-	*Smith et al.* (2010)
	$(6.465\pm0.785)\times10^{-11}cm^3s^{-1}$	-	-	*Xu et al.* (2012)
k_{OHO}	$2.5\times10^{-11}cm^3s^{-1}$	-	-	*Makhlouf et al.* (1995)

$*$: Uncertainties (the upper and lower bound) of the rate rates in the second column can be calculated by multiplying and dividing the rate constant by a coefficient $f(T)$ using the expression (*Sander et al.*, 2011):

$$f(T) = f(298)\times exp\{abs[g(\frac{1}{T}-\frac{1}{298})]\}$$

Table tab-5: Collisional rate constants for $OH(v)$ quenching by N_2. ($k_{N_2}(v)$: the total removal rate constant at vibrational v.)

	$k_{N_2}(v)^\star$			
v	a	b	c	d
1	0.058	-	-	-
2	0.10	-	-	-
3	0.17	-	-	-
4	0.30	-	-	-
5	0.52	-	-	-
6	0.91	-	-	-
7	1.60	-	-	-
8	2.70	7.0	-	7.0
9	4.80	-	7.0 ± 2.0	$3.36exp(220/T)^*$

* units: $\times 10^{-13} cm^3 mole^{-1} s^{-1}$

a: *Makhlouf et al.* (1995)

b: *Adler-Golden* (1997) (observed by M. J. Dyer et al., 1997)

c: *Kalogerakis et al.* (2011)

d: *Mlynczak et al.* (2013b) (The 9th rate constant was recommended by K. Kalogerakis (SRI International, 2008))

* T: temperature in Kelvin.

Table tab-6: Collisional rate constants for $OH(v)$ quenching by O_2. ($k_{O_2}(v)$: the total removal rate constant at vibrational v; $k^*_{O_2,(v,v')}$: the state to state rate constant; P_v: the probability factor.)

	$k_{O_2}(v)^\star$							-
v	a	b	c	d	e	f	g	P_v
1	0.13 ±0.04	-	-	-	-	0.19	0.14	0.043
2	0.27 ±0.08	-	-	-	-	0.4	0.29	0.083
3	0.52 ±0.15	-	-	-	-	0.77	0.56	0.15
4	0.88 ±0.3	-	-	-	-	1.3	0.94	0.23
5	1.7 ±0.7	-	-	-	-	2.5	1.8	0.36
6	3.0 ±1.5	-	-	-	-	4.3	3.1	0.50
7	-	7.0 ±2.0	-	-	-	10.2	7.4	0.72
8	-	-	8.0 ±1.0	-	-	11.9	8.6	0.75
9	-	-	-	22.0 ±6.0	$10.5exp(220/T)^\dagger$	30.9	22.3	0.95

*: $k_{O_2,(v,v')} = C[P_v]^{v-v'}$ $(0 \le v' < v)$, $C = 4.4 \times 10^{-12} cm^3 mole^{-1} s^{-1}$ (*Adler-Golden*, 1997), $C = (3.181 \pm 0.669) \times 10^{-12} cm^3 mole^{-1} s^{-1}$ (*Xu et al.*, 2012).

* units: $\times 10^{-12} cm^3 mole^{-1} s^{-1}$

a: *Dodd et al.* (1991)

b: *Knutsen et al.* (1996)

c: *Dyer et al.* (1997)

d: *Kalogerakis et al.* (2011)

e: *Mlynczak et al.* (2013b) (recommended by K. Kalogerakis (SRI International, 2008))

f: *Adler-Golden* (1997)

g: *Xu et al.* (2012)

† T: temperature in Kelvin.

A.5 Tikhonov regularization

A combination of zero- and first- order Tikhonov regularization was utilized in our work to dampen influences of measurement noises on the retrieval results. The zero-order matrix is an $n \times n$ identity matrix.

$$\mathbf{L_0} = \underbrace{\begin{bmatrix} 1 & 0 & 0 & 0 & \cdots & 0 \\ 0 & 1 & 0 & 0 & \ddots & \vdots \\ \vdots & \ddots & \ddots & \ddots & \ddots & \vdots \\ 0 & \cdots & 0 & 1 & 0 & 0 \\ 0 & \cdots & 0 & 0 & 1 & 0 \\ 0 & \cdots & 0 & 0 & 0 & 1 \end{bmatrix}}_{n}$$

The first-order matrix is an altitude dependent $n \times n$ first order derivative operator.

$$\mathbf{L_1} = \frac{1}{h} \underbrace{\begin{bmatrix} -3 & 3 & 0 & 0 & 0 & \cdots & 0 \\ 0 & -3 & 3 & 0 & 0 & \ddots & \vdots \\ 0 & 0 & -1 & 1 & 0 & \ddots & \vdots \\ \vdots & \ddots & \ddots & \ddots & \ddots & \ddots & 0 \\ 0 & \cdots & 0 & 0 & -1 & 1 & 0 \\ 0 & \cdots & 0 & 0 & 0 & -1 & 1 \\ 0 & \cdots & 0 & 0 & 0 & 0 & 0 \end{bmatrix}}_{n}$$

where, h is the uniform grid size (3.3 km in the work), that is, the distance of the two adjacent tangent points. In the work, three times larger elements in the

matrix are selected for the first two rows, corresponding to extremely low signal to noise ratio of the measurements at high altitudes.

Then, $\mathbf{S_a^{-1}}$ can be expressed as the weighted average of the zero- and first-order matrix by multiplying a baseline regularisation strength r.

$$\mathbf{S_a^{-1}} = r(a\mathbf{L_0^T L_0} + b\mathbf{L_1^T L_1})$$

where, a and b are set to 0.1 and 10 in our work. r is adjusted in such a way that the two terms on the right hand side of equation 4.4 are comparable.

A.6 Temporal variations of green line volume emission rate and atomic oxygen abundance

Figure fig-3 and fig-4 display the temporal distribution of atomic oxygen abundance ($[O]$) and green line volume emission rate (VER) profile, respectively, at 0–5°N and 10°N–15°N. Pronounced SAO and AO variations of VER and $[O]$ are found at each latitude bin. Solar cycle variations of VER, $[O]$ and their peak altitude are also significant at each latitude bin with a minimum in 2008.

Figure fig-5 and fig-6 show the latitude-temporal distribution of green line VERs and atomic oxygen abundances, respectively, at 92 km, 96 km and 100 km. Pronounced SAO, AO and solar cycle variations of VER and $[O]$ are also found at different latitudes and altitudes. As found in Figure 5.14, the green line emission and atomic oxygen abundances are much more pronounced in mid latitudes.

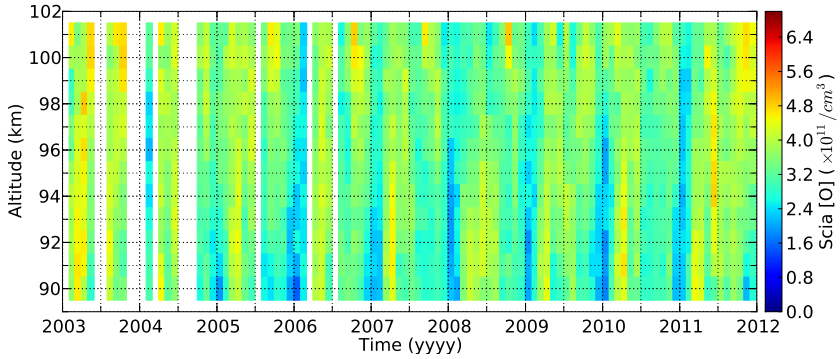

(a) *O* variations at 0–5°N

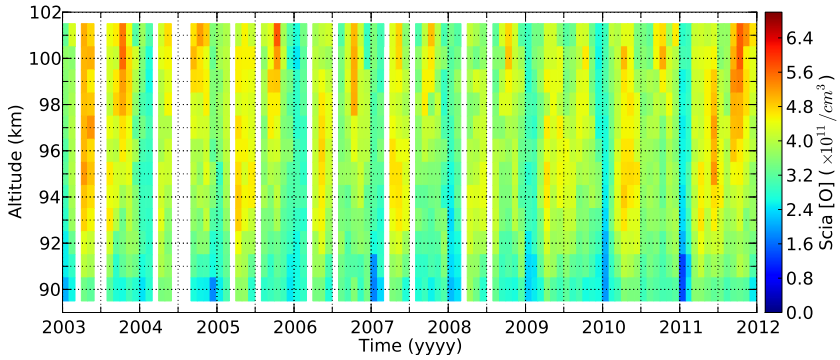

(b) *O* variations at 10°N–15°N

Figure fig-3: Altitude–temporal cross sections of atomic oxygen abundances from 2003 to 2011 at 0–5°N and 10°N–15°N.

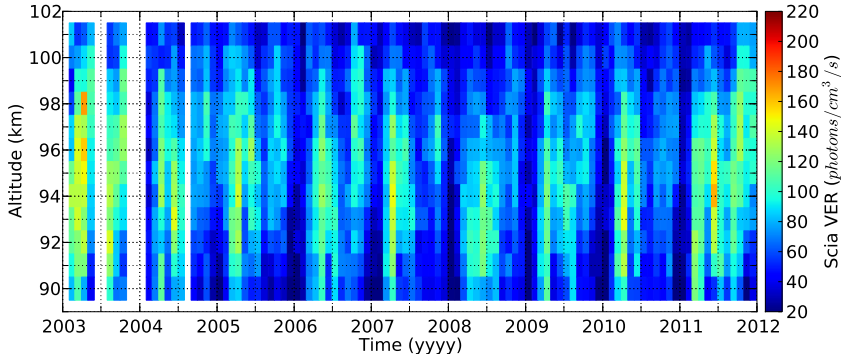

(a) VER variations at 0–5°N

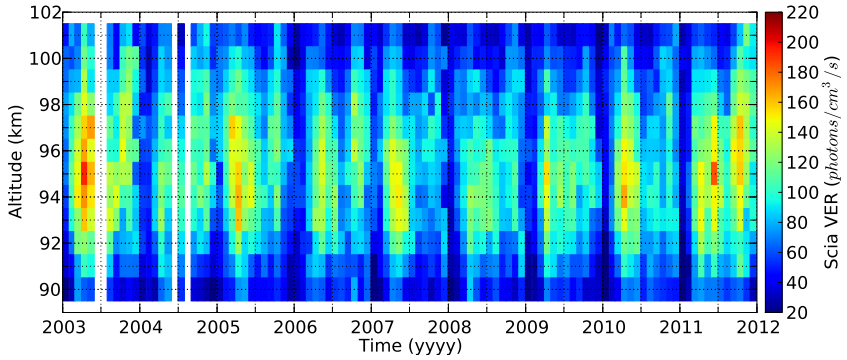

(b) VER variations at 10°N–15°N

Figure fig-4: Altitude–temporal cross sections of green line volume emission rate from 2003 to 2011 at 0–5°N and 10°N–15°N.

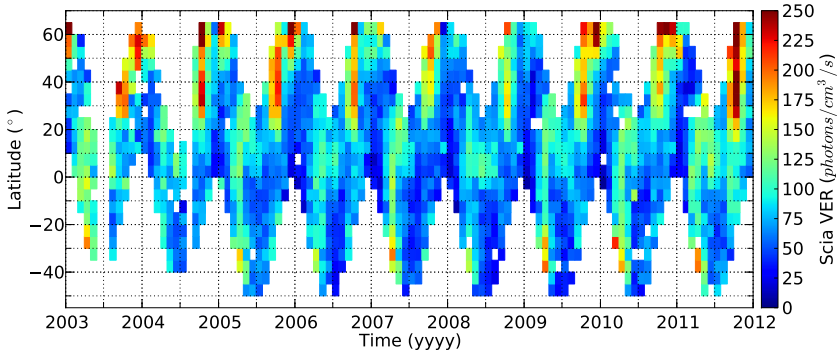

(a) VER variations at 92 km

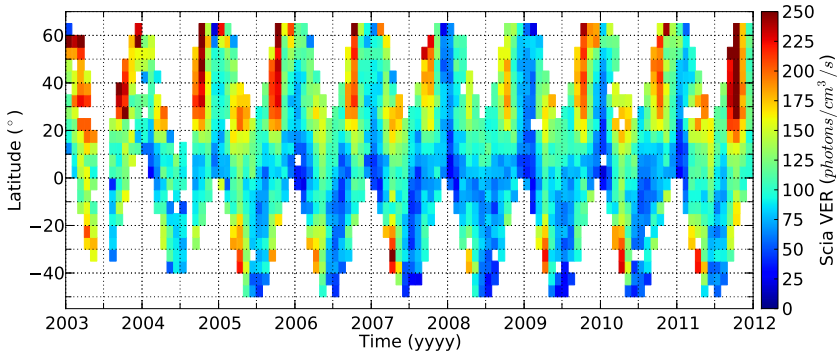

(b) VER variations at 96 km

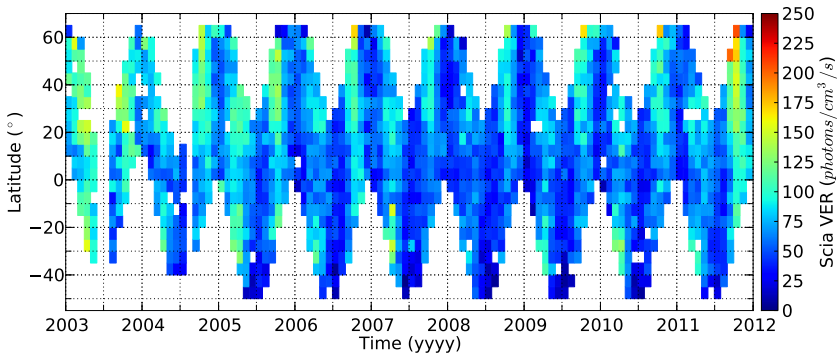

(c) VER variations at 100 km

Figure fig-5: Latitude–temporal cross sections of green line volume emission rate from 2003 to 2011 at 92 km, 96 km and 100 km.

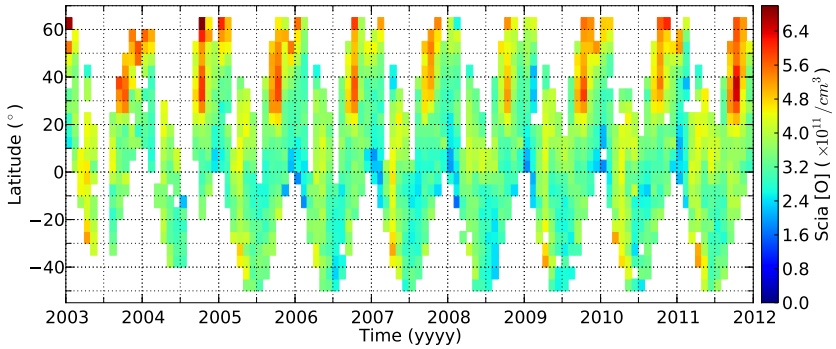

(a) *O* variations at 92 km

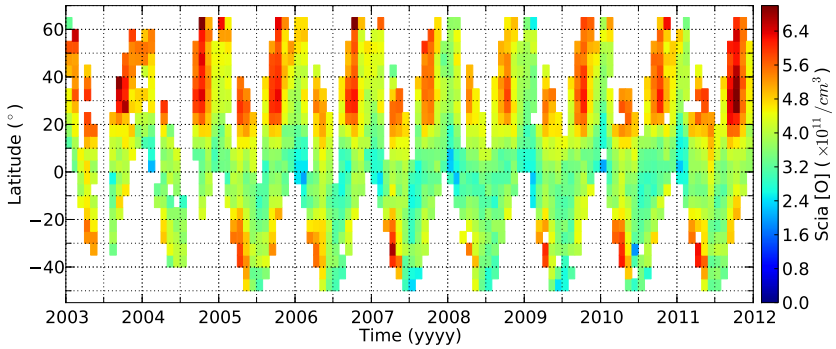

(b) *O* variations at 96 km

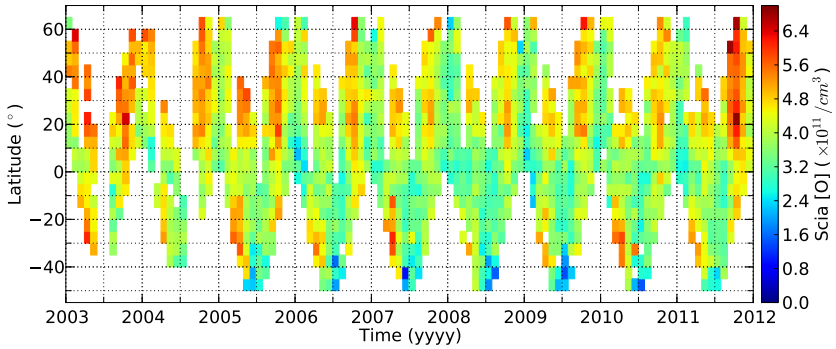

(c) *O* variations at 100 km

Figure fig-6: Latitude–temporal cross sections of atomic oxygen abundances from 2003 to 2011 at 92 km, 96 km and 100 km.

A.7 Effect on atomic oxygen abundances due to the usage of different *OH* Einstein coefficients.

Since two latest *OH* Einstein coefficients are available (*van der Loo and Groenenboom*, 2007; *Rothman et al.*, 2013), it is preferable to make a comparison to derived atomic oxygen abundances from SCIAMACHY *OH*(9–6) band emission measurements based on these two Einstein coefficients. The utilized *OH*(9–6) band Einstein coefficients for the retrieval from HITRAN and Trans databases are listed in Table 3.1. The HITRAN data is found approximately 13% larger than the Trans data for the *OH*(9–6) band Einstein coefficients and the derived atomic oxygen abundances using the Trans data are around 13% larger than for HITRAN data (Figure fig-7), where Einstein coefficients are inversely proportional to the derived atomic oxygen abundances, which has also been verified by the uncertainty assessment of Einstein coefficient in Figure 6.5. A 10% uncertainty of Einstein coefficient maps nearly linearly into atomic oxygen abundances. Therefore, it is 6% difference expected in the reconstructed SABER atomic oxygen in comparison to the data calculated by *Mlynczak et al.* (2013b) if HITRAN data used.

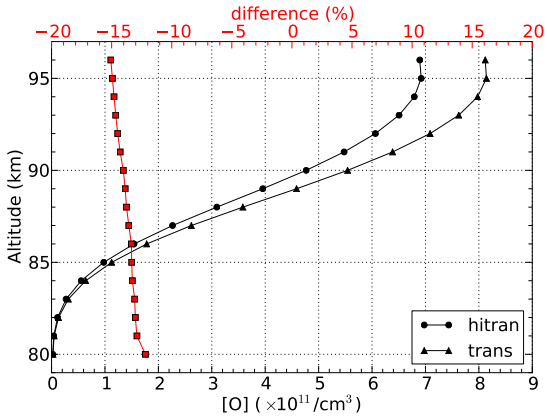

Figure fig-7: Derived atomic oxygen abundances (hitran and trans) from *OH*(9–6) band emission measurements based on the HITRAN and Trans Einstein coefficients at 35°N–40°N for November, 2005. Red square line shows percentage deviations of these two atomic oxygen profiles.

A.8 Latitudinal and temporal variations of atomic oxygen abundances and volume emission rates derived from SCIAMACHY $OH(9-6)$ band measurements

Global zonal mean atomic oxygen concentrations derived from SCIAMACHY *OH* airglow measurements are given in Figure fig-8. Enhanced atomic oxygen concentrations appear around 90 km in April over equatorial region. This is caused by the tidal vertical transport. Zonal inhomogeneity of atomic oxygen is also pronounced.

Figure fig-9 shows latitude-temporal variations of monthly zonal mean atomic oxygen from the year 2003 to 2011 at three altitudes. Annual oscillation (AO) dominates the atomic oxygen variations in mid and high latitudes at 95 km. It maximizes on October. Semi-annual oscillation (SAO) is observed with maxima on April and October. Significant solar cycle impact on the atomic oxygen variations is also found in mid latitudes at 95 km. SAO and AO are pronounced over the equatorial region at 85 km and 90 km. The latitudinal structure is mainly supposed to be the signature of the diurnal migrating tide, which can be characterized by a distinctive Hough (1, 1) mode.

Altitude-temporal variations of monthly mean zonal mean atomic oxygen are given in Figure fig-10. SAO, AO and solar cycle impact are pronounced, as shown in fig-9. Atomic oxygen concentrations at 2.5°N peak around 90 km and the peak altitude is about 5 km lower than other two latitudes.

The latitude-temporal variations of monthly zonal mean $OH(9-6)$ band nightglow emissions are displayed in Figure fig-11. Pronounced SAO variations are found over the equatorial region at each altitude. The SAO signals are found with maxima near equinox seasons and minima near solstice seasons. AO signals can be discerned over the equatorial region due to enhanced emissions in vernal equinox, which is also found in the SABER *OH* nightglow measurements by *Gao et al.* (2010). SAO and AO signals are also found in the mid latitudes but with weak amplitudes. Pronounced solar cycle variations are also found in the data at 95 km.

Figure fig-12 displays the altitude-temporal variations of monthly zonal

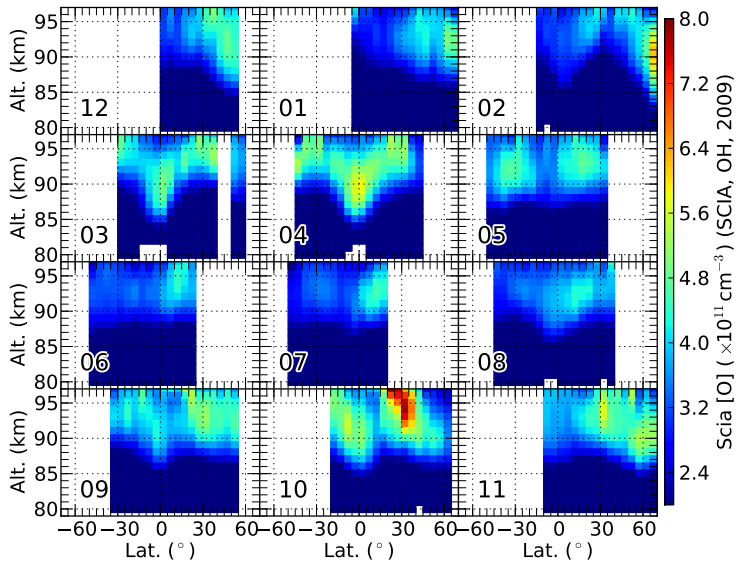

Figure fig-8: SCIAMACHY zonal mean nighttime atomic oxygen concentration derived from *OH* airglow measurements for 2009.

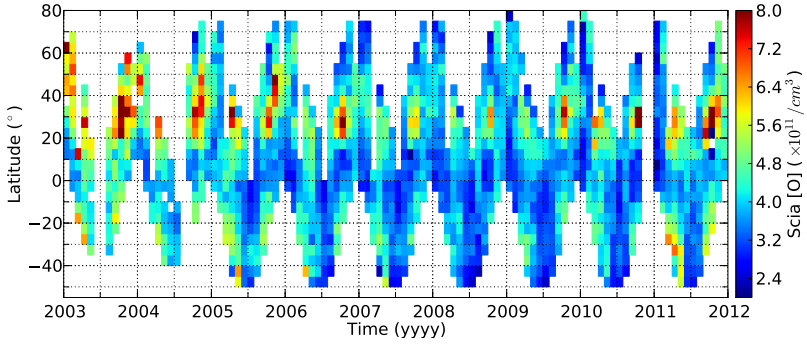

(a) 95 km

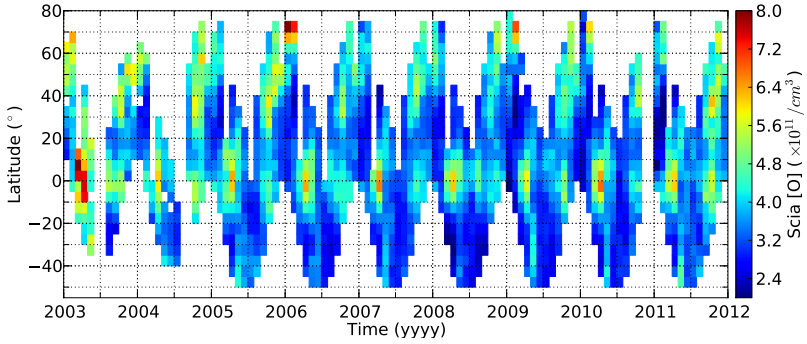

(b) 90 km

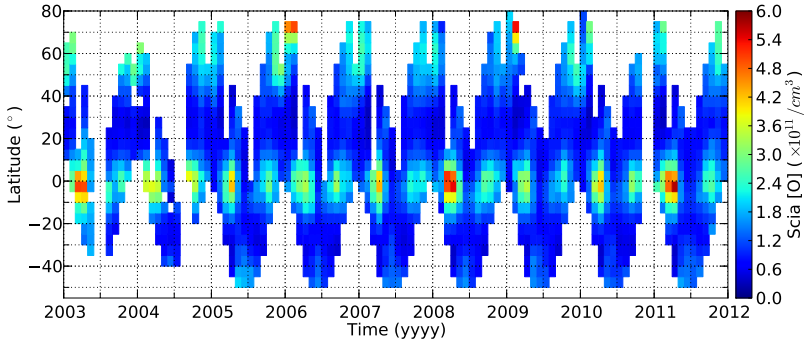

(c) 85 km

Figure fig-9: Temporal variations of monthly zonal mean SCIAMACHY atomic oxygen derived from *OH* nightglow measurements in latitude from the year 2003 to 2011 at different altitudes.

mean OH(9-6) band nightglow emissions at 2.5°, 22.5° and 42.5°. It is clear that VERs over the equatorial region are much brighter than those at other latitudes in the whole time series. Peak heights also vary with time at each latitude, such as SAO and AO variations. Peak heights at 2.5° are around 85 km and much lower than for other latitudes. With the exception of SAO and AO variations, peak heights also have a three year variation with minima on October 2005, April 2008 and April 2011 and maxima on October 2006 and October 2009 at 2.5°. This suggests a strong downward transport of atomic oxygen over the equatorial region driven by downward tidal motion at 10 p.m., which is consistent with the finding of the atomic oxygen over the equatorial region as shown in Figure fig-10.

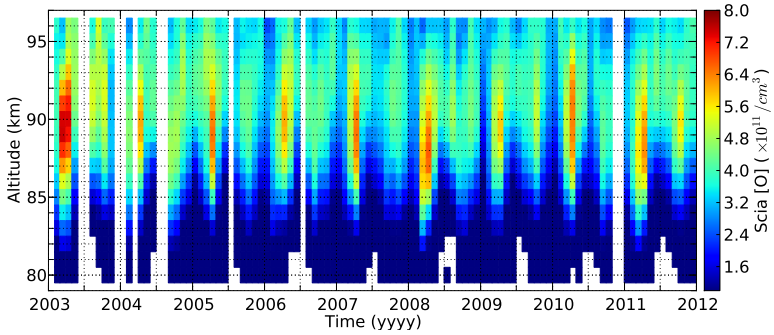

(a) 2.5°N

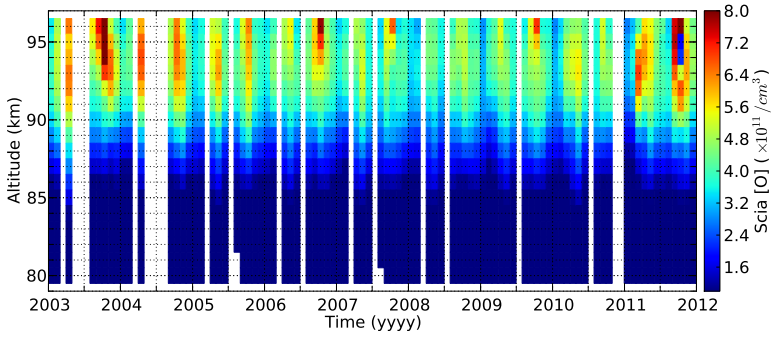

(b) 22.5°N

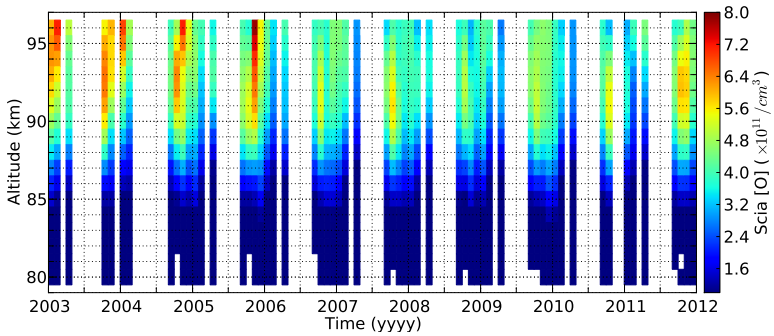

(c) 42.5°N

Figure fig-10: Altitude-temporal variations of monthly zonal mean SCIAMACHY atomic oxygen derived from *OH* nightglow measurements from the year 2003 to 2011 at different latitudes.

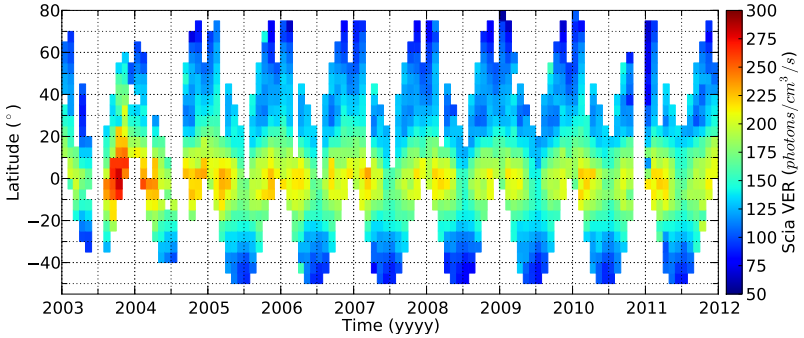

(a) 95 km

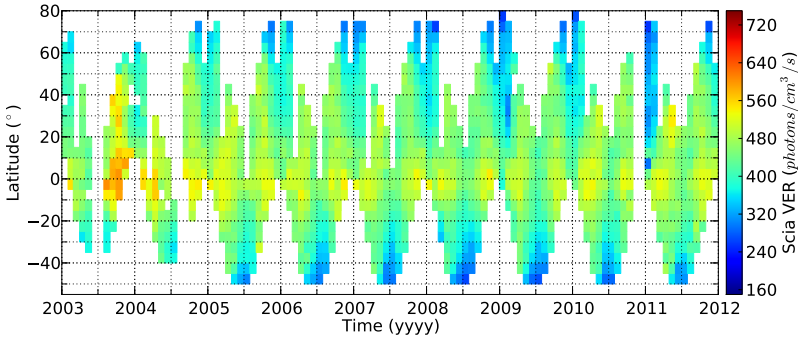

(b) 90 km

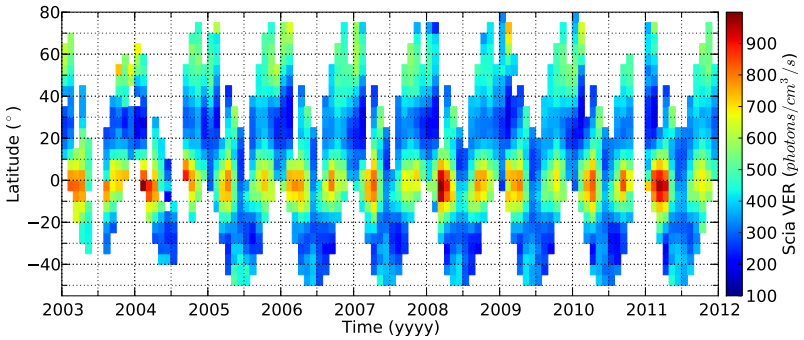

(c) 85 km

Figure fig-11: Latitude-temporal variations of monthly zonal mean SCIAMACHY $OH(9-6)$ band nightglow emissions from the year 2003 to 2011 at 95 km (a), 90 km (b) and 85 km (c).

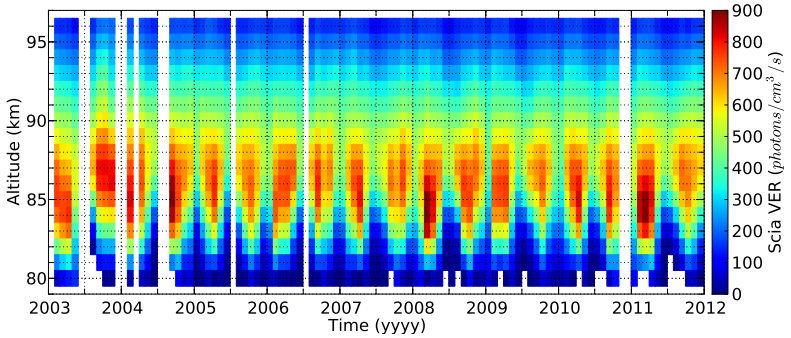

(a) 2.5°

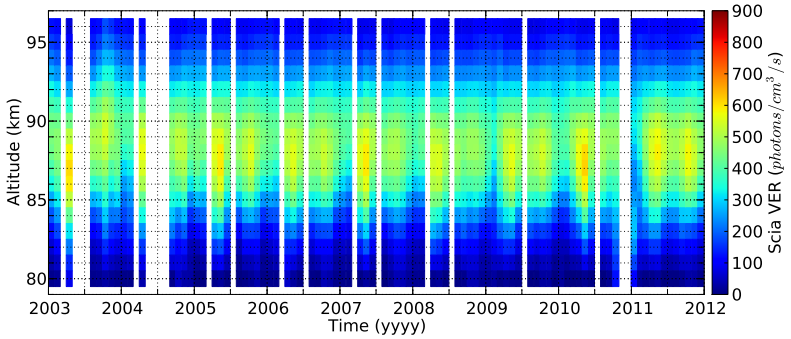

(b) 22.5°

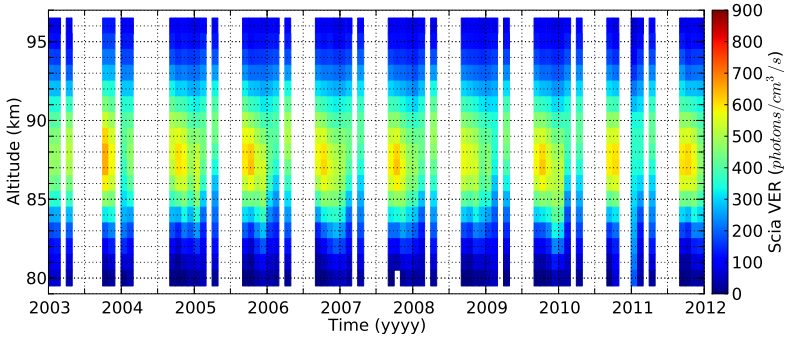

(c) 42.5°

Figure fig-12: Altitude-temporal variations of monthly zonal mean SCIAMACHY $OH(9-6)$ band nightglow emissions from the year 2003 to 2011 at 2.5°N (a), 22.5°N (b) and 42.5°N (c).

A.9 SABER atomic oxygen abundances

Global zonal mean atomic oxygen concentrations derived from SABER database are given in Figure fig-13. Atomic oxygen abundances are larger than SCIAMACHY atomic oxygen derived from $OH(9-6)$ band nightglow measurements (Figure fig-8), but a similar morphology is found by comparison to the corresponding global data in each month. This indicates that both instruments (SABER and SCIAMACHY) successfully capture the same phenomena happening in the UMLT region.

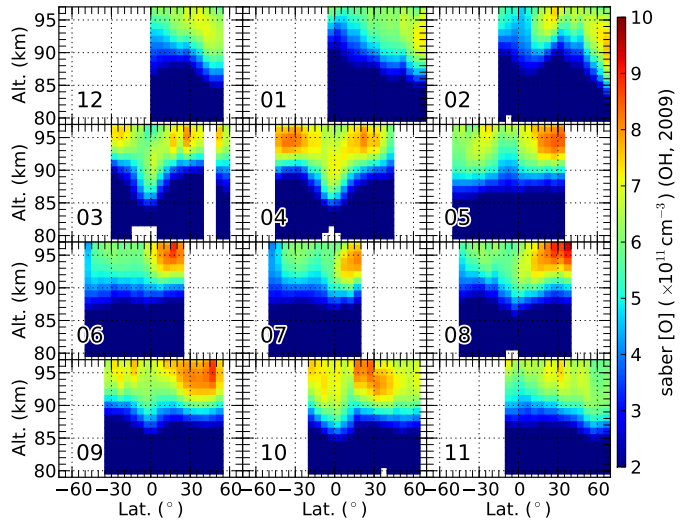

Figure fig-13: SABER zonal mean nighttime atomic oxygen concentration at 9–11 p.m. for 2009.

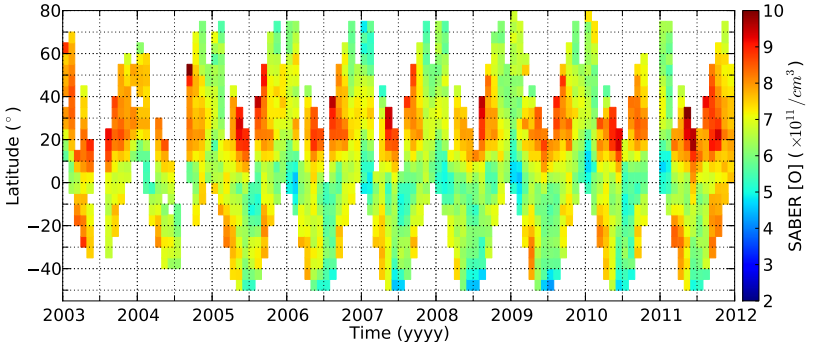

(a) 95 km

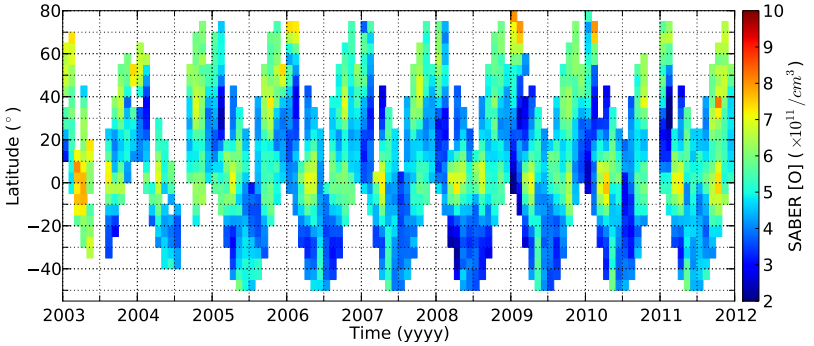

(b) 90 km

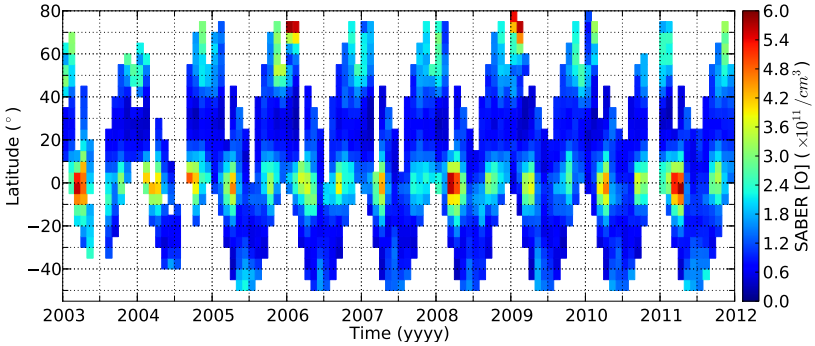

(c) 85 km

Figure fig-14: Temporal variations of monthly zonal mean SABER atomic oxygen in latitude from the year 2003 to 2011 at different altitudes.

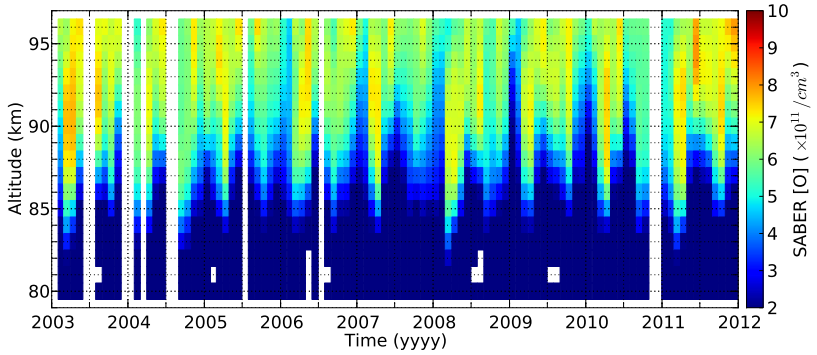

(a) 2.5°N

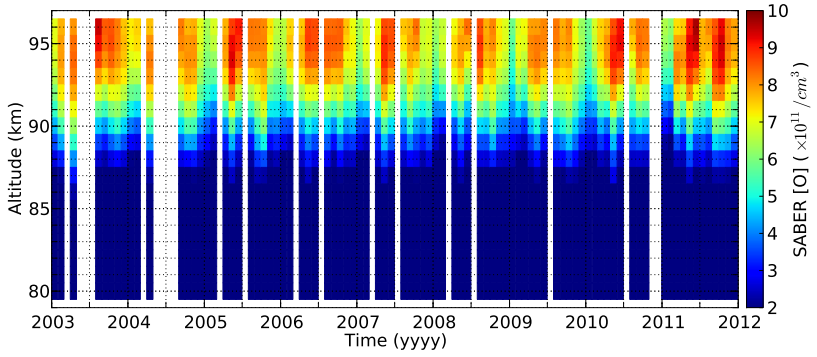

(b) 22.5°N

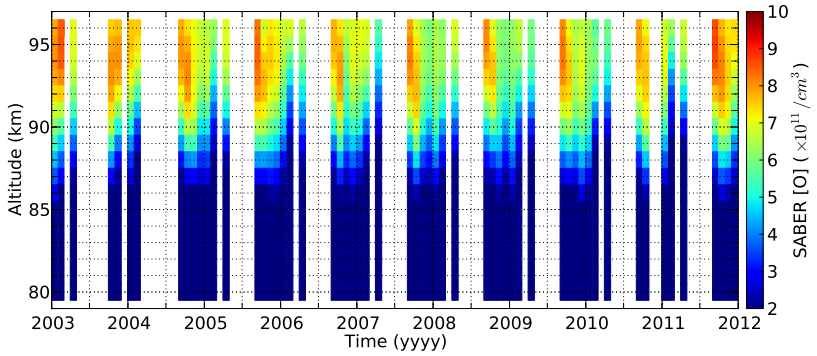

(c) 42.5°N

Figure fig-15: Altitude-temporal variations of monthly zonal mean SABER atomic oxygen from the year 2003 to 2011 at different latitudes.

Acknowledgements

Firstly, I would like to express my special appreciation and thanks to Prof. Dr. Martin Riese for providing me with this meaningful topic and for his invaluable advice on research. Thanks for Martin's tremendous academic support. I am also very grateful to Prof. Dr. Ralf Koppmann for offering me the opportunity to work at Bergische Universität Wuppertal and for supporting my research.

Furthermore, I would like to address my sincere gratitude to Dr. Martin Kaufmann, who is not only a dedicated scientific advisor in my research, providing me with many insightful discussions and suggestions, but also an enthusiastic friend in daily life, giving me plenty of help. I am particularly indebted to Martin for his constant faith in my work and for giving me the freedom to pursue various projects without objection. Also, profound gratitude goes to Dr. Manfred Ern for his helpful comments on my work and publications.

I am also grateful to all remaining colleagues from the IEK-7 and from the atmospheric physics department of the Bergische Universität Wuppertal. It is a great pleasure to work with them in the past three and a half years. Particularly, many thanks to my friends (too many to list here but you know who you are!) for providing kindly help and sincere friendship.

Last, but not least, I would like to express my heartfelt gratitude to my beloved wife. I am very indebted to my wife for her understanding and bearing with me during the course of my study.

Bibliography

Adler-Golden, S. (1997), Kinetic parameters for OH nightglow modeling consistent with recent laboratory measurements, *Journal of Geophysical Research: Space Physics*, *102*(A9), 19,969–19,976, doi:10.1029/97JA01622.

Baker, D. J., and A. T. J. Stair (1988), Rocket measurements of the altitude distributions of the hydroxyl airglow, *Physica Scripta*, *37*(4), 611.

Barth, C. A. (1961), Research summary, *JPL*, *64*, 36–39.

Barth, C. A., and A. F. Hildebrandt (1961), The 5577 A airglow emission mechanism, *Journal of Geophysical Research*, *66*(3), 985–986, doi:10.1029/JZ066i003p00985.

Bates, D. (1988a), Excitation of 557.7 nm OI line in nightglow, *Planetary and Space Science*, *36*(9), 883 – 889, doi:http://dx.doi.org/10.1016/0032-0633(88)90094-3, special Issue: Atomic Oxygen Abundance in Thermosphere.

Bates, D. (1988b), Excitation and quenching of the oxygen bands in the nightglow, *Planetary and Space Science*, *36*(9), 875 – 881, doi:http://dx.doi.org/10.1016/0032-0633(88)90093-1, special Issue: Atomic Oxygen Abundance in Thermosphere.

Bates, D. R. (1988c), *Progress in Atmospheric Physics: Proceedings of the 15th Annual Meeting on Atmospheric Studies by Optical Methods, held in Granada, Spain, 6–11 September 1987*, chap. The Oxygen

Nightglow, pp. 3–31, Springer Netherlands, Dordrecht, doi:10.1007/978-94-009-3009-4_1.

Bates, D. R., and M. Nicolet (1950), The photochemistry of atmospheric water vapor, *Journal of Geophysical Research*, *55*(3), 301–327, doi:10.1029/JZ055i003p00301.

Baulch, D. L., D. D. Drysdale, J. Duxbury, and S. J. Grant (1976), *Evaluated Kinetic Data for High Temperature Reactions: Homogeneous Gas Phase Reactions of the 02-03 System, the CO-02-HZ System and of Sulphur Containing Species v. 3*, Butterworths, Boston.

Bernath, P. F., and R. Colin (2009), Revised molecular constants and term values for the $X^2\Pi$ and $B^2\Sigma^+$ states of OH, *Journal of Molecular Spectroscopy*, *257*(1), 20 – 23, doi:http://dx.doi.org/10.1016/j.jms.2009.06.003.

Bittner, M., D. Offermann, H.-H. Graef, M. Donner, and K. Hamilton (2002), An 18-year time series of OH rotational temperatures and middle atmosphere decadal variations, *Journal of Atmospheric and Solar-Terrestrial Physics*, *64*(8â11), 1147 – 1166, doi:http://dx.doi.org/10.1016/S1364-6826(02)00065-2, PSMOS 2000 Workshop - Planetary Scale Mesopause Observing System.

Brasseur, G., and D. Offermann (1986), Recombination of atomic oxygen near the mesopause: Interpretation of rocket data, *Journal of Geophysical Research: Atmospheres*, *91*(D10), 10,818–10,824, doi:10.1029/JD091iD10p10818.

Burrage, M. D., W. R. Skinner, and P. B. Hays (1997), Intercalibration of HRDI and WINDII wind measurements, *Annales Geophysicae*, *15*(9), 1089–1098, doi:10.1007/s00585-997-1089-8.

Campbell, I., and C. Gray (1973), Rate constants for $O(^3P)$ recombination and association with $N(^4S)$, *Chemical Physics Letters*, *18*(4), 607 – 609, doi:http://dx.doi.org/10.1016/0009-2614(73)80479-8.

Campbell, I. M., and B. A. Thrush (1967), The association of oxygen atoms and their combination with nitrogen atoms, *Proceedings of the Royal Society of London A: Mathematical, Physical and Engineering Sciences*, *296*(1445), 222–232, doi:10.1098/rspa.1967.0015.

Capetanakis, F. P., F. Sondermann, S. Höser, and F. Stuhl (1993), Temperature dependence of the quenching of $O(^1S)$ by simple inorganic molecules, *The Journal of Chemical Physics*, *98*(10), 7883–7887, doi:http://dx.doi.org/10.1063/1.464596.

Chalamala, B. R., and R. A. Copeland (1993), Collision dynamics of $OH(X^2\Pi$, v=9), *The Journal of Chemical Physics*, *99*(8), 5807–5811, doi:http://dx.doi.org/10.1063/1.465932.

Chapman, S. (1931), Some phenomena of the upper atmosphere, *Proceedings of the Royal Society of London A: Mathematical, Physical and Engineering Sciences*, *132*(820), 353–374, doi:10.1098/rspa.1931.0105.

Charters, P. E., R. G. Macdonald, and J. C. Polanyi (1971), Formation of vibrationally excited OH by the reaction H + O_3, *Appl. Opt.*, *10*(8), 1747–1754, doi:10.1364/AO.10.001747.

Clemesha, B., and H. Takahashi (1996), Rocket-borne measurements of horizontal structure in the OH(8,3) and Na D airglow emissions, *Advances in Space Research*, *17*(11), 81 – 84, doi:http://dx.doi.org/10.1016/0273-1177(95)00733-U.

Clemesha, B., H. Takahashi, D. Simonich, D. Gobbi, and P. Batista (2005), Experimental evidence for solar cycle and long-term change in the low-latitude MLT region, *Journal of Atmospheric and Solar-Terrestrial Physics*, *67*(1-2), 191 – 196, doi:http://dx.doi.org/10.1016/j.jastp.2004.07.027.

Colin, R., P. Coheur, M. Kiseleva, A. Vandaele, and P. Bernath (2002), Spectroscopic constants and term values for the $X^2\Pi_i$ state of OH (v=0-

10), *Journal of molecular spectroscopy*, *214*(2), 225–226, doi:10.1006/jmsp.2002.8591.

Cosby, P. C., and T. G. Slanger (2007), OH spectroscopy and chemistry investigated with astronomical sky spectra, *Canadian Journal of Physics*, *85*(2), 77–99, doi:10.1139/p06-088.

Dandekar, B., and J. Turtle (1971), Atomic oxygen concentration from the measurement of the [OI] 5577 Å emission of the airglow, *Planetary and Space Science*, *19*(8), 949 – 957, doi:http://dx.doi.org/10.1016/0032-0633(71)90145-0.

Das (2011), Effects of solar cycle variations on oxygen green line emission rate over Kiso, Japan, *Earth, Planets and Space*, *63*(8), 941–948, doi:10.5047/eps.2011.04.006.

Deutsch, K. A., and G. Hernandez (2003), Long-term behavior of the OI 558 nm emission in the night sky and its aeronomical implications, *Journal of Geophysical Research: Space Physics*, *108*(A12), doi:10.1029/2002JA009611.

Dodd, J. A., S. J. Lipson, and W. A. M. Blumberg (1990), Vibrational relaxation of OH($X^2\Pi$, v=1-3) by O_2, *The Journal of Chemical Physics*, *92*(6), 3387–3393, doi:http://dx.doi.org/10.1063/1.457849.

Dodd, J. A., S. J. Lipson, and W. A. M. Blumberg (1991), Formation and vibrational relaxation of OH($X^2\Pi$, v) by O_2 and CO_2, *The Journal of Chemical Physics*, *95*(8), 5752–5762, doi:http://dx.doi.org/10.1063/1.461597.

Dodd, J. A., S. J. Lipson, J. R. Lowell, P. S. Armstrong, W. A. M. Blumberg, R. M. Nadile, S. M. Adler-Golden, W. J. Marinelli, K. W. Holtzclaw, and B. D. Green (1994), Analysis of hydroxyl earthlimb airglow emissions: Kinetic model for state-to-state dynamics of OH (v, N), *Journal of Geophysical Research: Atmospheres*, *99*(D2), 3559–3585, doi:10.1029/93JD03338.

Dyer, M. J., K. Knutsen, and R. A. Copeland (1997), Energy transfer in the ground state of OH: Measurements of OH(v=8,10,11) removal, *The Journal of Chemical Physics*, *107*(19), 7809–7815, doi:http://dx.doi.org/10.1063/1.475094.

Efron, B. (1979), Bootstrap methods: Another look at the jackknife, *The Annals of Statistics*, *7*(1), 1–26, doi:10.1214/aos/1176344552.

Fomichev, V. I., C. Fu, J. de Grandpré, S. R. Beagley, V. P. Ogibalov, and J. C. McConnell (2004), Model thermal response to minor radiative energy sources and sinks in the middle atmosphere, *Journal of Geophysical Research: Atmospheres*, *109*(D19), n/a–n/a, doi:10.1029/2004JD004892, d19107.

Forbes, J. M., X. Zhang, and D. R. Marsh (2014), Solar cycle dependence of middle atmosphere temperatures, *Journal of Geophysical Research: Atmospheres*, *119*(16), 9615–9625, doi:10.1002/2014JD021484.

French, W. J. R., and A. R. Klekociuk (2011), Long-term trends in Antarctic winter hydroxyl temperatures, *Journal of Geophysical Research: Atmospheres*, *116*(D4), n/a–n/a, doi:10.1029/2011JD015731, d00P09.

Fukuyama, K. (1976), Airglow variations and dynamics in the lower thermosphere and upper mesosphere-1. diurnal variation and its seasonal dependency, *Journal of Atmospheric and Terrestrial Physics*, *38*(12), 1279 – 1287, doi:http://dx.doi.org/10.1016/0021-9169(76)90136-7.

Fukuyama, K. (1977), Airglow variations and dynamics in the lower thermosphere and upper mesosphere-II. seasonal and long-term variations, *Journal of Atmospheric and Terrestrial Physics*, *39*(1), 1 – 14, doi:http://dx.doi.org/10.1016/0021-9169(77)90038-1.

Gao, H., J. Xu, and Q. Wu (2010), Seasonal and QBO variations in the OH nightglow emission observed by TIMED/SABER, *Journal of Geophysical Research: Space Physics*, *115*(A6), n/a–n/a, doi:10.1029/2009JA014641, a06313.

Gao, H., J.-B. Nee, and J. Xu (2012), The emission of oxygen green line and density of O atom determined by using ISUAL and SABER measurements, *Annales Geophysicae*, *30*(4), 695â701, doi:10.5194/angeo-30-695-2012.

García-Comas, M., M. López-Puertas, B. T. Marshall, P. P. Wintersteiner, B. Funke, D. Bermejo-Pantaleón, C. J. Mertens, E. E. Remsberg, L. L. Gordley, M. G. Mlynczak, and J. M. Russell (2008), Errors in Sounding of the Atmosphere using Broadband Emission Radiometry (SABER) kinetic temperature caused by non-local-thermodynamic-equilibrium model parameters, *Journal of Geophysical Research: Atmospheres*, *113*(D24), n/a–n/a, doi:10.1029/2008JD010105, d24106.

Gobbi, D., H. Takahashi, B. Clemesha, and P. Batista (1992), Equatorial atomic oxygen profiles derived from rocket observations of OI 557.7 nm airglow emission, *Planetary and Space Science*, *40*(6), 775 – 781, doi:http://dx.doi.org/10.1016/0032-0633(92)90106-X.

Goldman, A., W. Schoenfeld, D. Goorvitch, C. C. Jr, H. Dothe, F. Mélen, M. Abrams, and J. Selby (1998), Updated line parameters for OH $X^2\Pi$-$X^2\Pi(v'', v')$ transitions, *Journal of Quantitative Spectroscopy and Radiative Transfer*, *59*(3 - 5), 453 – 469, doi:http://dx.doi.org/10.1016/S0022-4073(97)00112-X, atmospheric Spectroscopy Applications 96.

Good, R. (1976), Determination of atomic oxygen density from rocket borne measurement of hydroxyl airglow, *Planetary and Space Science*, *24*(4), 389 – 395, doi:http://dx.doi.org/10.1016/0032-0633(76)90052-0.

Gottwald, M., H. Bovensmann, G. Lichtenberg, S. Noël, A. von Bargen, S. Slijkhuis, A. Piters, R. Hoogeveen, C. von Savigny, M. Buchwitz, A. Kokhanovsky, A. Richter, A. Rozanov, T. Holzer-Popp, K. Bramstedt, J.-C. Lambert, J. Skupin, F. Wittrock, H. Schrijver, and J. Burrows (2006), *SCIAMACHY-Monitoring the Changing Earth's Atmosphere*, Springer Netherlands.

Greer, R., D. Murtagh, I. McDADE, P. Dickinson, L. Thomas, D. Jenkins, J. Stegman, E. Llewellyn, G. Witt, D. Mackinnon, and E. Williams (1986), ETON 1: A data base pertinent to the study of energy transfer in the oxygen nightglow, *Planetary and Space Science*, *34*(9), 771 – 788, doi:http://dx.doi.org/10.1016/0032-0633(86)90074-7.

Greet, P. A., W. J. R. French, G. B. Burns, P. F. B. Williams, R. P. Lowe, and K. Finlayson (1998), OH(6-2) spectra and rotational temperature measurements at Davis, Antarctica, *Annales Geophysicae*, *16*(1), 77–89, doi:10.1007/s00585-997-0077-3.

Gumbel, J. (1998), Rocket-borne optical measurements of minor constituents in the middle atmosphere, Ph.D. thesis, Stockholm University.

Haley, C., I. McDade, and S. Melo (2001), An assessment of a method for recovering atomic oxygen density profiles from column integrated nightglow intensity measurements, *Advances in Space Research*, *27*(6-7), 1147 – 1152, doi:http://dx.doi.org/10.1016/S0273-1177(01)00147-8.

Hansen, P. C. (1992), Analysis of discrete ill-posed problems by means of the L-Curve, *SIAM Review*, *34*(4), 561–580, doi:10.1137/1034115.

Hanuschik, R. W. (2003), A flux-calibrated, high-resolution atlas of optical sky emission from UVES, *A&A*, *407*(3), 1157–1164, doi:10.1051/0004-6361:20030885.

Hays, P. B., V. J. Abreu, M. E. Dobbs, D. A. Gell, H. J. Grassl, and W. R. Skinner (1993), The High-Resolution Doppler Imager on the Upper Atmosphere Research Satellite, *Journal of Geophysical Research: Atmospheres*, *98*(D6), 10,713–10,723, doi:10.1029/93JD00409.

Hecht, J. H., A. Z. Liu, R. L. Walterscheid, R. G. Roble, M. F. Larsen, and J. H. Clemmons (2004), Airglow emissions and oxygen mixing ratios from the photometer experiment on the Turbulent Oxygen Mixing Experiment (TOMEX), *Journal of Geophysical Research: Atmospheres*, *109*(D2), n/a–n/a, doi:10.1029/2002JD003035, d02S05.

Hedin, J., J. Gumbel, J. Stegman, and G. Witt (2009), Use of O_2 airglow for calibrating direct atomic oxygen measurements from sounding rockets, *Atmospheric Measurement Techniques*, *2*(2), 801–812, doi: 10.5194/amt-2-801-2009.

Iwagami, N., T. Shibaki, T. Suzuki, H. Sekiguchi, N. Takegawa, and W. Morrow (2003), Rocket observations of atomic oxygen density and airglow emission rate in the WAVE2000 campaign, *Journal of Atmospheric and Solar-Terrestrial Physics*, *65*(16-18), 1349 – 1360, doi: http://dx.doi.org/10.1016/j.jastp.2003.08.002.

Kalogerakis, K. S., G. P. Smith, and R. A. Copeland (2011), Collisional removal of OH($X^2\Pi$, v) by O, O_2, O_3, N_2, and CO_2, *Journal of Geophysical Research: Atmospheres*, *116*(D20), n/a–n/a, doi: 10.1029/2011JD015734, d20307.

Kaufmann, M., C. Lehmann, L. Hoffmann, B. Funke, M. López-Puertas, C. Savigny, and M. Riese (2008), Chemical heating rates derived from SCIAMACHY vibrationally excited OH limb emission spectra, *Advances in Space Research*, *41*(11), 1914 – 1920, doi:http://dx.doi.org/10.1016/j.asr.2007.07.045.

Kaufmann, M., C. Lehmann, and M. Riese (2010), Solar cycle 23 in SCIAMACHY mesospheric chemical heating rates, in *Proceedings of the 2010 ESA Living Planet Symposium, 18 June - 2 July 2010, Bergen, Norway (ESA SP-686)*.

Kaufmann, M., M. Ern, C. Lehmann, and M. Riese (2013), The response of atomic hydrogen to solar radiation changes, in *Climate and Weather of the Sun-Earth System (CAWSES)*, edited by F.-J. Lübken, Springer Atmospheric Sciences, pp. 171–188, Springer Netherlands.

Kaufmann, M., Y. Zhu, M. Ern, and M. Riese (2014), Global distribution of atomic oxygen in the mesopause region as derived from SCIAMACHY O(^{1}S) green line measurements, *Geophysical Research Letters*, *41*(17), 6274–6280, doi:10.1002/2014GL060574.

Khomich, V. Y., A. I. Semenov, and N. N. Shefov (2008), *Airglow as an indicator of upper atmospheric structure and dynamics*, Springer, New York; London.

Klenerman, D., and I. W. M. Smith (1987), Infrared chemiluminescence studies using a SISAM spectrometer. Reactions producing vibrationally excited OH, *J. Chem. Soc., Faraday Trans. 2*, *83*, 229–241, doi:10.1039/F29878300229.

Knutsen, K., and R. A. Copeland (1993), Vibrational relaxation of OH($X^2\Pi$, v= 7, 8) by O_2, N_2, N_2O and CO_2, *EOS. Trans. AGU*, *(43) Fall Meeting Suppl.*, 472.

Knutsen, K., M. J. Dyer, and R. A. Copeland (1996), Collisional removal of OH($X^2\Pi$, v= 7) by O_2, N_2, CO_2, and N_2O, *The Journal of Chemical Physics*, *104*(15), 5798–5802, doi:http://dx.doi.org/10.1063/1.471311.

Krasnopolsky, V. (1986), Oxygen emissions in the night airglow of the Earth, Venus and Mars, *Planetary and Space Science*, *34*(6), 511 – 518, doi:http://dx.doi.org/10.1016/0032-0633(86)90089-9.

Langhoff, S. R., H.-J. Werner, and P. Rosmus (1986), Theoretical transition probabilities for the OH Meinel system, *Journal of Molecular Spectroscopy*, *118*(2), 507 – 529, doi:http://dx.doi.org/10.1016/0022-2852(86)90186-4.

Lednyts'kyy, O., C. von Savigny, K.-U. Eichmann, and M. G. Mlynczak (2015), Atomic oxygen retrievals in the MLT region from SCIAMACHY nightglow limb measurements, *Atmospheric Measurement Techniques*, *8*(3), 1021–1041, doi:10.5194/amt-8-1021-2015.

Liu, G., and G. G. Shepherd (2008), An investigation of the solar cycle impact on the lower thermosphere O(^{1}S) nightglow emission as observed by WINDII/UARS, *Advances in Space Research*, *42*(5), 933 – 938, doi:http://dx.doi.org/10.1016/j.asr.2007.10.008.

Liu, W., J. Xu, A. K. Smith, and W. Yuan (2015), Comparison of rotational temperature derived from ground-based OH airglow observations with TIMED/SABER to evaluate the Einstein coefficients, *Journal of Geophysical Research: Space Physics*, *120*(11), 10,069–10,082, doi:10.1002/2015JA021886, 2015JA021886.

Llewellyn, E., and I. McDade (1996), A reference model for atomic oxygen in the terrestrial atmosphere, *Advances in Space Research*, *18*(9-10), 209 – 226, doi:http://dx.doi.org/10.1016/0273-1177(96)00059-2.

Lomb, N. R. (1976), Least-squares frequency analysis of unequally spaced data, *Astrophysics and Space Science*, *39*(2), 447–462, doi:10.1007/BF00648343.

López-González, M., J. López-Moreno, and R. Rodrigo (1992), Altitude profiles of the atmospheric system of O_2 and of the green line emission, *Planetary and Space Science*, *40*(6), 783 – 795, doi:http://dx.doi.org/10.1016/0032-0633(92)90107-Y.

Louet, J. (2001), The envisat mission and system, *ESA Bulletin*, *106*, 11–25.

Lourakis, M. L. A., and A. A. Argyros (2005), Is Levenberg-Marquardt the most efficient optimization algorithm for implementing bundle adjustment?, *Computer Vision, 2005. ICCV 2005. Tenth IEEE International Conference on*, *2*, 1526–1531.

Madsen, K., H. B. Nielsen, and O. Tingleff (2004), *Methods for Non-Linear Least Squares Problems (2nd ed.)*, Informatics and Mathematical Modelling, Technical University of Denmark, DTU.

Makhlouf, U. B., R. H. Picard, and J. R. Winick (1995), Photochemical-dynamical modeling of the measured response of airglow to gravity waves: 1. Basic model for OH airglow, *Journal of Geophysical Research: Atmospheres*, *100*(D6), 11,289–11,311, doi:10.1029/94JD03327.

McDade, I., and E. Llewellyn (1988), Mesospheric oxygen atom densities inferred from night-time OH Meinel band emission rates, *Planetary and Space Science*, *36*(9), 897 – 905, doi:http://dx.doi.org/10.1016/0032-0633(88)90097-9.

McDade, I., D. Murtagh, R. Greer, P. Dickinson, G. Witt, J. Stegman, E. Llewellyn, L. Thomas, and D. Jenkins (1986), ETON 2: Quenching parameters for the proposed precursors of $O_2(b^1\Sigma_g^+)$ and $O(^1S)$ in the terrestrial nightglow, *Planetary and Space Science*, *34*(9), 789 – 800, doi:http://dx.doi.org/10.1016/0032-0633(86)90075-9.

McDade, I. C. (1991), The altitude dependence of the $OH(X^2\Pi)$ vibrational distribution in the nightglow: Some model expectations, *Planetary and Space Science*, *39*(7), 1049 – 1057, doi:http://dx.doi.org/10.1016/0032-0633(91)90112-N.

McDade, I. C., and E. J. Llewellyn (1986), The excitation of $O(^1S)$ and O_2 bands in the nightglow: a brief review and preview, *Canadian Journal of Physics*, *64*(12), 1626–1630, doi:10.1139/p86-287.

McDade, I. C., and E. J. Llewellyn (1987), Kinetic parameters related to sources and sinks of vibrationally excited OH in the nightglow, *Journal of Geophysical Research: Space Physics*, *92*(A7), 7643–7650, doi:10.1029/JA092iA07p07643.

Meinel, I. A. B. (1950), OH emission bands in the spectrum of the night sky, *Astrophys. J.*, *111*, 555–564.

Melo, S. M., H. Takahashi, B. Clemesha, P. P. Batista, and D. Simonich (1996), Atomic oxygen concentrations from rocket airglow observations in the equatorial region, *Journal of Atmospheric and Terrestrial Physics*, *58*(16), 1935 – 1942, doi:http://dx.doi.org/10.1016/0021-9169(95)00192-1, atmospheric Studies by Optical Methods.

Melo, S. M. L., I. C. McDade, and H. Takahashi (2001), Atomic oxygen density profiles from ground-based nightglow measurements at 23°S,

Journal of Geophysical Research: Atmospheres, *106*(D14), 15,377–15,384, doi:10.1029/2000JD900820.

Mies, F. H. (1974), Calculated vibrational transition probabilities of OH($X^2\Pi$), *Journal of Molecular Spectroscopy*, *53*(2), 150 – 188, doi:http://dx.doi.org/10.1016/0022-2852(74)90125-8.

Mlynczak, M. G., and S. Solomon (1993), A detailed evaluation of the heating efficiency in the middle atmosphere, *Journal of Geophysical Research: Atmospheres*, *98*(D6), 10,517–10,541, doi:10.1029/93JD00315.

Mlynczak, M. G., L. H. Hunt, C. J. Mertens, B. T. Marshall, J. M. Russell, M. López Puertas, A. K. Smith, D. E. Siskind, J. C. Mast, R. E. Thompson, and L. L. Gordley (2013a), Radiative and energetic constraints on the global annual mean atomic oxygen concentration in the mesopause region, *Journal of Geophysical Research: Atmospheres*, *118*(11), 5796–5802, doi:10.1002/jgrd.50400.

Mlynczak, M. G., L. A. Hunt, J. C. Mast, B. Thomas Marshall, J. M. Russell, A. K. Smith, D. E. Siskind, J.-H. Yee, C. J. Mertens, F. Javier Martin-Torres, R. Earl Thompson, D. P. Drob, and L. L. Gordley (2013b), Atomic oxygen in the mesosphere and lower thermosphere derived from SABER: algorithm theoretical basis and measurement uncertainty, *Journal of Geophysical Research: Atmospheres*, *118*(11), 5724–5735, doi:10.1002/jgrd.50401.

Moreels, G., G. Megie, A. Jones, and R. Gattinger (1977), An oxygen-hydrogen atmospheric model and its application to the OH emission problem, *Journal of Atmospheric and Terrestrial Physics*, *39*(5), 551 – 570, doi:http://dx.doi.org/10.1016/0021-9169(77)90065-4.

Morgan, J. E., and H. I. Schiff (1963), Recombination of oxygen atoms in the presence of inert gases, *The Journal of Chemical Physics*, *38*(7), 1495–1500, doi:http://dx.doi.org/10.1063/1.1776908.

Morgan, J. E., L. Elias, and H. I. Schiff (1960), Recombination of oxygen atoms in the absence of O_2, *The Journal of Chemical Physics*, *33*(3), 930–931, doi:http://dx.doi.org/10.1063/1.1731292.

Murtagh, D., G. Witt, J. Stegman, I. McDade, E. Llewellyn, F. Harris, and R. Greer (1990), An assessment of proposed $O(^1S)$ and $O_2(b^1\Sigma_g^+)$ nightglow excitation parameters, *Planetary and Space Science*, *38*(1), 43–53, doi:10.1016/0032-0633(90)90004-A.

Nee, J.-B., S.-D. Tsai, T.-H. Peng, R.-R. Hsu, A. B.-C. Chen, S. Zhang, T.-Y. Huang, P. K. Rajesh, J.-Y. Liu, H. U. Frey, and S. B. Mende (2010), OH airglow and equatorial variations observed by ISUAL instrument on board the FORMOSAT 2 satellite, *Terr. Atmos. Ocean. Sci.*, *21*, 985–995.

Nelson, D. D., A. Schiffman, D. J. Nesbitt, J. J. Orlando, and J. B. Burkholder (1990), $H+O_3$ Fourier-transform infrared emission and laser absorption studies of $OH(X^2\Pi)$ radical: An experimental dipole moment function and state-to-state Einstein *A* coefficients, *The Journal of Chemical Physics*, *93*(10), 7003–7019, doi:http://dx.doi.org/10.1063/1.459476.

Nicolaides, C., O. Sinanoğlu, and P. Westhaus (1969), Theory of atomic structure including electron correlation. II. all-external pair correlations in the various states and ions of B, C, N, O, F, Ne, and Na, and prediction of electron affinities and atomic excitation energies, *Phys. Rev.*, *181*, 54–65, doi:10.1103/PhysRev.181.54.

Noël, S., H. Bovensmann, M. Wuttke, J. Burrows, M. Gottwald, E. Krieg, A. Goede, and C. Muller (2002), Nadir, limb, and occultation measurements with SCIAMACHY, *Advances in Space Research*, *29*(11), 1819 – 1824, doi:http://dx.doi.org/10.1016/S0273-1177(02)00102-3.

Noll, S., W. Kausch, S. Kimeswenger, S. Unterguggenberger, and A. M. Jones (2015), OH populations and temperatures from simultaneous spectroscopic observations of 25 bands, *Atmospheric Chemistry and Physics*, *15*(7), 3647–3669, doi:10.5194/acp-15-3647-2015.

Offermann, D., and A. Drescher (1973), Atomic oxygen densities in the lower thermosphere as derived from in situ 5577-A night airglow and mass spectrometer measurements, *Journal of Geophysical Research*, *78*(28), 6690–6700, doi:10.1029/JA078i028p06690.

Offermann, D., and R. Gerndt (1990), Upper mesosphere temperatures from OH*-emissions, *Advances in Space Research*, *10*(12), 217 – 221, doi:http://dx.doi.org/10.1016/0273-1177(90)90399-K.

Offermann, D., V. Friedrich, P. Ross, and U. V. Zahn (1981), Neutral gas composition measurements between 80 and 120 km, *Planetary and Space Science*, *29*(7), 747 – 764, doi:http://dx.doi.org/10.1016/0032-0633(81)90046-5.

Offermann, D., P. Hoffmann, P. Knieling, R. Koppmann, J. Oberheide, and W. Steinbrecht (2010), Long-term trends and solar cycle variations of mesospheric temperature and dynamics, *Journal of Geophysical Research: Atmospheres*, *115*(D18), n/a–n/a, doi:10.1029/2009JD013363, d18127.

Ohoyama, H., T. Kasai, Y. Yoshimura, H. Kimura, and K. Kuwata (1985), Initial distribution of vibration of the OH radicals produced in the H + $O_3 \rightarrow OH(X^2\Pi_{1/2,3/2}) + O_2$ reaction. chemiluminescence by a crossed beam technique, *Chemical Physics Letters*, *118*(3), 263 – 266, doi:http://dx.doi.org/10.1016/0009-2614(85)85312-4.

Parihar, M. G., N. (2008), Measurement of mesopause temperature from hydroxyl nightglow at Kolhapur (16.8°N, 74.2°E), India, *Advances in Space Research*, *41*(4), 660–669, doi:10.1016/j.asr.2007.05.002.

Pejaković, D. A., K. S. Kalogerakis, R. A. Copeland, and D. L. Huestis (2008), Laboratory determination of the rate coefficient for three-body recombination of oxygen atoms in nitrogen, *Journal of Geophysical Research: Space Physics*, *113*(A4), n/a–n/a, doi:10.1029/2007JA012694, a04303.

Pendleton, W. R., P. J. Espy, and M. R. Hammond (1993), Evidence for non-local-thermodynamic-equilibrium rotation in the OH nightglow, *Journal of Geophysical Research: Space Physics*, *98*(A7), 11,567–11,579, doi:10.1029/93JA00740.

Picone, J. M., A. E. Hedin, D. P. Drob, and A. C. Aikin (2002), NRLMSISE-00 empirical model of the atmosphere: Statistical comparisons and scientific issues, *Journal of Geophysical Research: Space Physics*, *107*(A12), SIA 15–1–SIA 15–16, doi:10.1029/2002JA009430.

Rayleigh, L. (1924), The light of the night sky: Its intensity variations when analysed by colour filter, *Proc. R. Soc. London, Ser. A*, *119*, 117–137.

Rayleigh, L., and H. S. Jones (1935), The light of the night-sky: Analysis of the intensity variations at three stations, *Proceedings of the Royal Society of London A: Mathematical, Physical and Engineering Sciences*, *151*(872), 22–55, doi:10.1098/rspa.1935.0133.

Reid, I. M., A. J. Spargo, and J. M. Woithe (2014), Seasonal variations of the nighttime O(^{1}S) and OH(8-3) airglow intensity at Adelaide, Australia, *Journal of Geophysical Research: Atmospheres*, *119*(11), 6991–7013, doi:10.1002/2013JD020906.

Rensberger, K. J., J. B. Jeffries, and D. R. Crosley (1989), Vibrational relaxation of OH($X^2\Pi$,v=2), *The Journal of Chemical Physics*, *90*(4), 2174–2181, doi:http://dx.doi.org/10.1063/1.456671.

Riese, M., D. Offermann, and G. Brasseur (1994), Energy released by recombination of atomic oxygen and related species at mesopause heights, *Journal of Geophysical Research: Atmospheres*, *99*(D7), 14,585–14,593, doi:10.1029/94JD00356.

Roble, R. G. (1995), *Energetics of the Mesosphere and Thermosphere*, pp. 1–21, American Geophysical Union, Washington, D.C., doi:10.1029/GM087p0001.

Roble, R. G., and E. C. Ridley (1994), A thermosphere-ionosphere-mesosphere-electrodynamics general circulation model (time-GCM): Equinox solar cycle minimum simulations (30-500 km), *Geophysical Research Letters*, *21*(6), 417–420, doi:10.1029/93GL03391.

Rodgers, C. D. (2000), *Inverse Methods for Atmospheric Sounding: Theory and Practice*, *Series on Atmospheric, Oceanic and Planetary Physics*, vol. 2, World Scientific, Singapore.

Rothman, L., D. Jacquemart, A. Barbe, D. C. Benner, M. Birk, L. Brown, M. Carleer, C. C. Jr., K. Chance, L. Coudert, V. Dana, V. Devi, J.-M. Flaud, R. Gamache, A. Goldman, J.-M. Hartmann, K. Jucks, A. Maki, J.-Y. Mandin, S. Massie, J. Orphal, A. Perrin, C. Rinsland, M. Smith, J. Tennyson, R. Tolchenov, R. Toth, J. V. Auwera, P. Varanasi, and G. Wagner (2005), The HITRAN 2004 molecular spectroscopic database, *Journal of Quantitative Spectroscopy and Radiative Transfer*, *96*(2), 139 – 204, doi:http://dx.doi.org/10.1016/j.jqsrt.2004.10.008.

Rothman, L., I. Gordon, A. Barbe, D. Benner, P. Bernath, M. Birk, V. Boudon, L. Brown, A. Campargue, J.-P. Champion, K. Chance, L. Coudert, V. Dana, V. Devi, S. Fally, J.-M. Flaud, R. Gamache, A. Goldman, D. Jacquemart, I. Kleiner, N. Lacome, W. Lafferty, J.-Y. Mandin, S. Massie, S. Mikhailenko, C. Miller, N. Moazzen-Ahmadi, O. Naumenko, A. Nikitin, J. Orphal, V. Perevalov, A. Perrin, A. Predoi-Cross, C. Rinsland, M. Rotger, M. Simecková, M. Smith, K. Sung, S. Tashkun, J. Tennyson, R. Toth, A. Vandaele, and J. V. Auwera (2009), The HITRAN 2008 molecular spectroscopic database, *Journal of Quantitative Spectroscopy and Radiative Transfer*, *110*(9-10), 533–572, doi:10.1016/j.jqsrt.2009.02.013.

Rothman, L., I. Gordon, Y. Babikov, A. Barbe, D. C. Benner, P. Bernath, M. Birk, L. Bizzocchi, V. Boudon, L. Brown, A. Campargue, K. Chance, E. Cohen, L. Coudert, V. Devi, B. Drouin, A. Fayt, J.-M. Flaud, R. Gamache, J. Harrison, J.-M. Hartmann, C. Hill, J. Hodges, D. Jacquemart, A. Jolly, J. Lamouroux, R. L. Roy, G. Li, D. Long,

O. Lyulin, C. Mackie, S. Massie, S. Mikhailenko, H. Müller, O. Naumenko, A. Nikitin, J. Orphal, V. Perevalov, A. Perrin, E. Polovtseva, C. Richard, M. Smith, E. Starikova, K. Sung, S. Tashkun, J. Tennyson, G. Toon, V. Tyuterev, and G. Wagner (2013), The HITRAN2012 molecular spectroscopic database, *Journal of Quantitative Spectroscopy and Radiative Transfer*, *130*(0), 4 – 50, doi:http://dx.doi.org/10.1016/j.jqsrt.2013.07.002, HITRAN2012 special issue.

Rousselot, P., C. Lidman, J.-G. Cuby, G. Moreels, and G. Monnet (2000), Night-sky spectral atlas of OH emission lines in the near-infrared, *Astron. Astrophys.*, *354*, 1134–1150.

Russell, J. P. (2001), Atomic oxygen in the mesopause region derived from WINDII hydroxyl airglow measurements, Ph.D. thesis, The University of Western Ontario.

Russell, J. P. (2003), Atomic oxygen profiles (80-94 km) derived from Wind Imaging Interferometer/Upper Atmospheric Research Satellite measurements of the hydroxyl airglow: 1. Validation of technique, *Journal of Geophysical Research*, *108*(D21), doi:10.1029/2003JD003454.

Russell, J. P., W. E. Ward, R. P. Lowe, R. G. Roble, G. G. Shepherd, and B. Solheim (2005), Atomic oxygen profiles (80 to 115 km) derived from Wind Imaging Interferometer/Upper Atmospheric Research Satellite measurements of the hydroxyl and greenline airglow: Local time-latitude dependence, *Journal of Geophysical Research: Atmospheres*, *110*(D15), doi:10.1029/2004JD005570.

Sander, S. P., J. Abbatt, J. R. Barker, J. B. Burkholder, R. R. Friedl, D. M. Golden, C. E. Kolb, M. J. Kurylo, G. K. Moortgat, P. H. Wine, R. E. Huie, and V. L. Orkin (2011), Chemical kinetics and photochemical data for use in atmospheric studies, *Pasadena: Jet Propulsion Laboratory*, *Evaluation No. 17*.

Sappey, A. D., and R. A. Copeland (1990), Collision dynamics of OH($X^2\Pi$,v=12), *The Journal of Chemical Physics*, *93*(8), 5741–5746, doi:http://dx.doi.org/10.1063/1.459567.

Scargle, J. D. (1982), Studies in astronomical time series analysis. II - Statistical aspects of spectral analysis of unevenly spaced data, *Astrophysical Journal*, *263*, 835–853.

Schmidt, H., G. Brasseur, M. Charron, E. Manzini, M. Giorgetta, T. Diehl, V. Fomichev, D. Kinnison, D. Marsh, and S. Walters (2006), The HAMMONIA chemistry climate model: Sensitivity of the mesopause region to the 11-year solar cycle and CO_2 doubling, *Journal of Climate*, *19*, 3903–3931.

Sheese, P. E., I. C. McDade, R. L. Gattinger, and E. J. Llewellyn (2011), Atomic oxygen densities retrieved from Optical Spectrograph and Infrared Imaging System observations of O_2 A-band airglow emission in the mesosphere and lower thermosphere, *Journal of Geophysical Research*, *116*(D1), doi:10.1029/2010JD014640.

Sheese, P. E., E. J. Llewellyn, R. L. Gattinger, and K. Strong (2014), OH Meinel band nightglow profiles from OSIRIS observations, *Journal of Geophysical Research: Atmospheres*, *119*(19), 11,417–11,428, doi:10.1002/2014JD021617, 2014JD021617.

Shefov, N. (1969), Hydroxyl emission of the upper atmosphere—I: The behaviour during a solar cycle, seasons and geomagnetic disturbances, *Planetary and Space Science*, *17*(5), 797 – 813, doi:http://dx.doi.org/10.1016/0032-0633(69)90089-0.

Shepherd, G. G., J. Stegman, P. Espy, C. McLandress, G. Thuillier, and R. H. Wiens (1999), Springtime transition in lower thermospheric atomic oxygen, *Journal of Geophysical Research: Space Physics*, *104*(A1), 213–223, doi:10.1029/98JA02831.

Shepherd, G. G., Y.-M. Cho, G. Liu, M. G. Shepherd, and R. G. Roble (2006a), Airglow variability in the context of the global mesospheric

circulation, *Journal of Atmospheric and Solar-Terrestrial Physics*, *68*(17), 2000 – 2011, doi:http://dx.doi.org/10.1016/j.jastp.2006.06.006, long-term Trends and Short-term Variability in the Upper, Middle and Lower AtmosphereSymposia JSII02 Long-term trends in the upper atmosphere and JSMA03 Short-term variability and long-term changes in the lower and middle atmosphere.

Shepherd, M. G., J. C. McConnell, W. K. Tobiska, G. R. Gladstone, S. Chakrabarti, and G. Schmidtke (1995), Inference of atomic oxygen concentration from remote sensing of optical aurora, *Journal of Geophysical Research: Space Physics*, *100*(A9), 17,415–17,428, doi: 10.1029/94JA03374.

Shepherd, M. G., G. Liu, and G. G. Shepherd (2006b), Mesospheric semiannual oscillation in temperature and nightglow emission, *Journal of Atmospheric and Solar-Terrestrial Physics*, *68*(3-5), 379 – 389, doi: http://dx.doi.org/10.1016/j.jastp.2005.02.029, vertical Coupling in the Atmosphere/Ionosphere System2nd IAGA/ICMA Workshop on Vertical Coupling in the Atmosphere/Ionosphere System, Bath, UK, 12 - 15 July, 2004.

Silverman, S. M. (1970), Night airglow phenomenology, *Space Science Reviews*, *11*(2), 341–379, doi:10.1007/BF00241526.

Singh, V., I. C. McDade, G. G. Shepherd, B. H. Solheim, and W. E. Ward (1996), The O(^{1}S) dayglow emission as observed by the WIND imaging interferometer on the UARS, *Annales Geophysicae*, *14*(6), 637–646, doi:10.1007/s00585-996-0637-y.

Sivjee, G., K. Dick, and P. Feldman (1972), Temporal variations in night-time hydroxyl rotational temperature, *Planetary and Space Science*, *20*(2), 261 – 269, doi:http://dx.doi.org/10.1016/0032-0633(72)90107-9.

Slanger, T. G. (1976), O(^{1}S) quenching by O(^{3}P), *The Journal of Chemical Physics*, *64*(9), 3763, doi:10.1063/1.432691.

Slanger, T. G., and G. Black (1976), O(^{1}S) production from oxygen atom recombination, *The Journal of Chemical Physics*, *64*(9), 3767–3773, doi:http://dx.doi.org/10.1063/1.432692.

Slanger, T. G., and G. Black (1977), O(^{1}S) in the lower thermosphereâChapman vs Barth, *Planetary and Space Science*, *25*(1), 79 – 88, doi:http://dx.doi.org/10.1016/0032-0633(77)90120-9.

Slanger, T. G., , and R. A. Copeland (2003), Energetic oxygen in the upper atmosphere and the laboratory, *Chemical Reviews*, *103*(12), 4731–4766, doi:10.1021/cr0205311, pMID: 14664631.

Slanger, T. G., B. D. Sharpee, D. A. Pejaković, D. L. Huestis, M. A. Bautista, R. L. Gattinger, E. J. Llewellyn, I. C. McDade, D. E. Siskind, and K. R. Minschwaner (2011), Atomic oxygen emission intensity ratio: Observation and theory, *Eos, Transactions American Geophysical Union*, *92*(35), 291–292, doi:10.1029/2011EO350005.

Smith, A. (2012a), Global dynamics of the MLT, *Surveys in Geophysics*, *33*(6), 1177–1230, doi:10.1007/s10712-012-9196-9.

Smith, A. (2012b), Interactions between the lower, middle and upper atmosphere, *Space Science Reviews*, *168*(1-4), 1–21, doi:10.1007/s11214-011-9791-y.

Smith, A. K., and D. R. Marsh (2005), Processes that account for the ozone maximum at the mesopause, *Journal of Geophysical Research: Atmospheres*, *110*(D23), n/a–n/a, doi:10.1029/2005JD006298, d23305.

Smith, A. K., D. R. Marsh, J. M. Russell, M. G. Mlynczak, F. J. Martin-Torres, and E. Kyrölä (2008), Satellite observations of high nighttime ozone at the equatorial mesopause, *Journal of Geophysical Research*, *113*(D17), doi:10.1029/2008JD010066.

Smith, A. K., D. R. Marsh, M. G. Mlynczak, and J. C. Mast (2010), Temporal variations of atomic oxygen in the upper mesosphere from

SABER, *Journal of Geophysical Research*, *115*(D18), doi:10.1029/2009JD013434.

Smith, A. K., R. R. Garcia, D. R. Marsh, and J. H. Richter (2011a), WACCM simulations of the mean circulation and trace species transport in the winter mesosphere, *Journal of Geophysical Research: Atmospheres*, *116*(D20), n/a–n/a, doi:10.1029/2011JD016083, d20115.

Smith, A. K., D. R. Marsh, M. G. Mlynczak, J. M. Russell, and J. C. Mast (2011b), *Aeronomy of the Earth's Atmosphere and Ionosphere*, chap. SABER Observations of Daytime Atomic Oxygen and Ozone Variability in the Mesosphere, pp. 75–82, Springer Netherlands, Dordrecht, doi:10.1007/978-94-007-0326-1_5.

Smith, G. P., and R. Robertson (2008), Temperature dependence of oxygen atom recombination in nitrogen after ozone photolysis, *Chemical Physics Letters*, *458*(1â3), 6 – 10, doi:http://dx.doi.org/10.1016/j.cplett.2008.04.074.

Smith, I. W. M. (1984), The role of electronically excited states in recombination reactions, *International Journal of Chemical Kinetics*, *16*(4), 423–443, doi:10.1002/kin.550160411.

Steinfeld, J. I., S. M. Adler-Golden, and J. W. Gallagher (1987), Critical survey of data on the spectroscopy and kinetics of ozone in the mesosphere and thermosphere, *31*(31), 1–148, jILA Pub. 3552.

Strobel, D. F. (1978), Parameterization of the atmospheric heating rate from 15 to 120 km due to O_2 and O_3 absorption of solar radiation, *Journal of Geophysical Research: Oceans*, *83*(C12), 6225–6230, doi:10.1029/JC083iC12p06225.

Takahashi, H., Y. Sahai, and P. Batista (1984), Tidal and solar cycle effects on the OI 5577 Å, NaD and OH(8,3) airglow emissions observed at 23°S, *Planetary and Space Science*, *32*(7), 897 – 902, doi:http://dx.doi.org/10.1016/0032-0633(84)90013-8.

Takahashi, H., S. M. L. Melo, B. R. Clemesha, D. M. Simonich, J. Stegman, and G. Witt (1996), Atomic hydrogen and ozone concentrations derived from simultaneous lidar and rocket airglow measurements in the equatorial region, *Journal of Geophysical Research: Atmospheres*, *101*(D2), 4033–4040, doi:10.1029/95JD03035.

Takahashi, H., R. Buriti, D. Gobbi, and P. Batista (2002), Equatorial planetary wave signatures observed in mesospheric airglow emissions, *Journal of Atmospheric and Solar-Terrestrial Physics*, *64*(8-11), 1263 – 1272, doi:http://dx.doi.org/10.1016/S1364-6826(02)00040-8, {PSMOS} 2000 Workshop - Planetary Scale Mesopause Observing System.

Tapping, K. F. (2013), The 10.7cm solar radio flux (F10.7), *Space Weather*, *11*(7), 394–406, doi:10.1002/swe.20064.

Tikhonov, A. N., and V. Y. Arsenin (1977), *Solutions of ill-posed problems*, Winston, Washington D.C., USA.

Trinks, H., D. Offermann, U. von Zahn, and C. Steinhauer (1978), Neutral composition measurements between 90- and 220-km altitude by rocket-borne mass spectrometer, *Journal of Geophysical Research: Space Physics*, *83*(A5), 2169–2176, doi:10.1029/JA083iA05p02169.

Turnbull, D., and R. Lowe (1989), New hydroxyl transition probabilities and their importance in airglow studies, *Planetary and Space Science*, *37*(6), 723 – 738, doi:http://dx.doi.org/10.1016/0032-0633(89)90042-1.

van der Loo, M. P. J., and G. C. Groenenboom (2007), Theoretical transition probabilities for the OH Meinel system, *The Journal of Chemical Physics*, *126*(11), 114314, doi:http://dx.doi.org/10.1063/1.2646859.

von Savigny, C., and O. Lednyts'kyy (2013), On the relationship between atomic oxygen and vertical shifts between OH Meinel bands originating from different vibrational levels, *Geophysical Research Letters*, *40*(21), 5821–5825, doi:10.1002/2013GL058017.

von Savigny, C., I. C. McDade, K.-U. Eichmann, and J. P. Burrows (2012), On the dependence of the OH^* meinel emission altitude on vibrational level: SCIAMACHY observations and model simulations, *Atmospheric Chemistry and Physics*, *12*(18), 8813–8828, doi:10.5194/acp-12-8813-2012.

Wallace, J. M., and P. V. Hobbs (2006), *Atmospheric Science: An Introductory Survey*, second edition ed., Academic Press, San Diego.

Wiens, R. H., V. P. Bhatnagar, and L. L. Cogger (1999), WINDII measurements of nightglow enhancements in the South Atlantic Magnetic Anomaly Zone, *Geophysical Research Letters*, *26*(15), 2355–2358, doi:10.1029/1999GL900515.

Witt, G., J. Stegman, B. Solheim, and E. Llewellyn (1979), A measurement of the $O_2(b^1\Sigma_g^+\text{-}X^3\Sigma_g^-)$ atmospheric band and the $OI(^1S)$ green line in the nightglow, *Planetary and Space Science*, *27*(4), 341 – 350, doi:http://dx.doi.org/10.1016/0032-0633(79)90111-9.

Witt, G., J. Stegman, D. Murtagh, I. McDade, R. Greer, P. Dickinson, and D. Jenkins (1984), Collisional energy transfer and the excitation of $O_2(b^1\Sigma_g^+)$ in the atmosphere, *Journal of Photochemistry*, *25*(2-4), 365 – 378, doi:http://dx.doi.org/10.1016/0047-2670(84)87038-0.

Wraight, P. (1982), Association of atomic oxygen and airglow excitation mechanisms, *Planetary and Space Science*, *30*(3), 251 – 259, doi:http://dx.doi.org/10.1016/0032-0633(82)90003-4.

Xu, J., and A. K. Smith (2003), Perturbations of the sodium layer: controlled by chemistry or dynamics?, *Geophysical Research Letters*, *30*(20), n/a–n/a, doi:10.1029/2003GL018040, 2056.

Xu, J., A. K. Smith, W. Yuan, H.-L. Liu, Q. Wu, M. G. Mlynczak, and J. M. Russell (2007), Global structure and long-term variations of zonal mean temperature observed by TIMED/SABER, *Journal of Geophysical Research: Atmospheres*, *112*(D24), doi:10.1029/2007JD008546.

Xu, J., H. Gao, A. K. Smith, and Y. Zhu (2012), Using TIMED/SABER nightglow observations to investigate hydroxyl emission mechanisms in the mesopause region, *Journal of Geophysical Research: Atmospheres*, *117*(D2), n/a–n/a, doi:10.1029/2011JD016342, d02301.

Yeo, K. L., N. A. Krivova, and S. K. Solanki (2014), Solar cycle variation in solar irradiance, *Space Science Reviews*, *186*(1), 137–167, doi:10.1007/s11214-014-0061-7.

Zhang, S. P., and G. G. Shepherd (1999), The influence of the diurnal tide on the O(^{1}S) and OH emission rates observed by WINDII on UARS, *Geophysical Research Letters*, *26*(4), 529–532, doi:10.1029/1999GL900033.

Zhang, Y., and L. Paxton (2008), An empirical Kp-dependent global auroral model based on TIMED/GUVI FUV data, *Journal of Atmospheric and Solar-Terrestrial Physics*, *70*(8-9), 1231–1242, doi:10.1016/j.jastp.2008.03.008.

Zhu, Y., M. Kaufmann, M. Ern, and M. Riese (2015), Nighttime atomic oxygen in the mesopause region retrieved from SCIAMACHY O(^{1}S) green line measurements and its response to solar cycle variation, *Journal of Geophysical Research: Space Physics*, *120*(10), 9057–9073, doi:10.1002/2015JA021405, 2015JA021405.

Band / Volume 328
Conductivity and Structure of Sputtered ZnO:Al on Flat and Textured Substrates for Thin-Film Solar Cells
N. Sommer (2016), vii, 195, XIV pp
ISBN: 978-3-95806-156-9

Band / Volume 329
Glaslotfügen von Festoxid-Brennstoffzellen durch Laseraufschmelzung
M. Willberg (2016), 99 pp
ISBN: 978-3-95806-157-6

Band / Volume 330
The Role of Natural Nanoparticles and Colloids for Phosphorus Binding in Forested Headwater Catchments
N. Gottselig (2016), VIII, 116 pp
ISBN: 978-3-95806-160-6

Band / Volume 331
Numerische Modellierung der thermomechanischen Fluid-Struktur-Interaktion im SOFC-Stack
A. Al-Masri (2016), iii, 165 pp
ISBN: 978-3-95806-161-3

Band / Volume 332
Analysis of biomixtures to determine the fate of pesticides
S. Mukherjee (2016), xix, 136 pp
ISBN: 978-3-95806-163-7

Band / Volume 333
Temperature Dependence of Carbon Kinetic Isotope Effect for The Oxidation Reaction of Ethane by Hydroxyl Radicals Under Atmospherically Relevant Conditions: Experimental and Theoretical Studies
T. Piansawan (2016), 196 pp
ISBN: 978-3-95806-166-8

Band / Volume 334
Konzeption von Membranmodulen zur effizienten Abtrennung von Kohlendioxid aus Gasgemischen
S. Luhr (2016)
ISBN: 978-3-95806-170-5

Band / Volume 335
Einfluss fehlpassungsinduzierter Spannungsfelder auf den Transportprozess bei ionischer Leitung
J. Keppner (2016), viii, 171 pp
ISBN: 978-3-95806-171-2

Band / Volume 336
Production and Characterization of Monodisperse Uranium Particles for Nuclear Safeguards Applications
A. Knott (2016), A-H, 123, xxviii, xiii pp
ISBN: 978-3-95806-172-9

Band / Volume 337
3D hydrological simulation of a forested headwater catchment: Spatio-temporal validation and scale dependent parameterization
Z. Fang (2016), XVII, 119 pp
ISBN: 978-3-95806-174-3

Band / Volume 338
Influence of Thermomechanical Treatment on High Temperature Properties of Laves Phase Strengthened Ferritic Steels
M. Talík (2016), xxiii, 130 pp
ISBN: 978-3-95806-175-0

Band / Volume 339
Groundwater recharge in Slovenia
Results of a bilateral German-Slovenian Research project
Mišo Andjelov, Zlatko Mikulič, Björn Tetzlaff, Jože Uhan & Frank Wendland (2016)
ISBN: 978-3-95806-177-4

Band / Volume 340
Atomic oxygen derived from SCIAMACHY O(^{1}S) and OH airglow measurements in the Mesopause region
Y. Zhu (2016), 206 pp
ISBN: 978-3-95806-178-1

Weitere ***Schriften des Verlags im Forschungszentrum Jülich*** unter
http://wwwzb1.fz-juelich.de/verlagextern1/index.asp